From Hopping to Ballistic Transport in Graphene-Based Electronic Devices

From Hopping to Ballistic Transport in Graphene-Based Electronic Devices

A dissertation presented

by

Thiti Taychatanapat

to

The Department of Physics

in partial fulfillment of the requirements

for the degree of

Doctor of Philosophy

in the subject of

Physics

Harvard University

Cambridge, Massachusetts

April 2013

Dissertation Advisor:

Pablo Jarillo-Herrero

Author:

Thiti Taychatanapat

From Hopping to Ballistic Transport in Graphene-Based Electronic Devices

Abstract

This thesis describes electronic transport experiments in graphene from the hopping to the ballistic regime. The first experiment studies dual-gated bilayer graphene devices. By applying an electric field with these dual gates, we can open a band gap in bilayer graphene and observe an increase in resistance of over six orders of magnitude as well as a strongly non-linear behavior in the transport characteristics. A temperature-dependence study of resistance at large electric field at the charge neutrality point shows the change in the transport mechanism from a hopping dominated regime at low temperature to a diffusive regime at high temperature.

The second experiment examines electronic properties of Bernal-stacked trilayer graphene. Due to the low mobility of trilayer graphene on SiO_2 substrates, we employ hexagonal boron nitride as a local substrate to improve its mobility. This led us to observe a quantum Hall effect with multiple Landau level crossings, proving the coexistence of massless and massive Dirac fermions in Bernal-stacked trilayer graphene. From the position of these crossing points in magnetic field and electron density, we can deduce the band parameters used to model its band structure. At high magnetic field, we observe broken symmetry states via Landau level splittings as well as crossings among these broken-symmetry states.

In the third experiment, we investigate transverse magnetic focusing (TMF) in mono-, bi-, and tri-layer graphene. The ability to tune density allows us to electronically modify focal points and investigate TMF continuously from hole to electron regimes. This also allows us to observe the change in band structure of trilayer graphene as a function of applied electric field. Finally, we also observe TMF at room temperature in monolayer graphene which unambiguously proves the existence of ballistic transport at room temperature.

Contents

List of Figures

List of Tables

Citations to Previously Published Work

Chapters 4, 5, and 6 have appeared in the following papers:

"Electronic transport in dual-gated graphene at large displacement fields"
Thiti Taychatanapat and Pablo Jarillo-Herrero
Phys. Rev. Lett. **105**, 166601 (2010);

"Quantum Hall effect and Landau level crossing of Dirac fermions in trilayer graphene"
Thiti Taychatanapat, Kenji Watanabe, Takashi Taniguchi, and Pablo Jarillo-Herrero
Nature Physics **7**, 621–625 (2011);

"Electrically tunable transverse magnetic focusing in graphene"
Thiti Taychatanapat, Kenji Watanabe, Takashi Taniguchi, and Pablo Jarillo-Herrero
Nature Physics **9**, 225–229 (2013).

Acknowledgments

First, I would like to thank my advisor, Pablo Jarillo-Herrero. His enthusiasm and steadfast determination to understand every detail have often led to a better understanding of new data and "occasionally" late night g-chat or skype. His friendliness and ability to digest new information present to him are some of the things I hope to attain one day (the friendliness part might be impossible though). I am also thankful for his willingness to change the date for one of the group dinners so that I could go on a date, and for his help in establishing a contact in Singapore for my future career.

I would like to thank the members of my committee, Prof. Amir Yacoby and Prof. Subir Sachdev, for their advice and kindness over the years, and Prof. Charles Marcus for a research opportunity in my first year at Harvard. I am also deeply grateful for the research experience I had at Prof. Dan Ralph's lab at Cornell which gave me a good foundation on scientific research techniques.

When I first joined the Jarillo-Herrero group in summer 2008, the measurement lab was probably one of the most, if not the most, quiet and empty labs in Building 13, with only a He3 dewar standing in the corner. After 5 years, the room has now been filled with equipments and become significantly louder with 3 pumps and a pulse tube running simultaneously. Surprisingly though, the fabrication lab still remains pretty much unchanged and stays peculiarly almost as clean as it was on the first day I joined the lab (except the hot plate).

Many lab members have contributed to filling the lab with useful equipments which I have benefitted throughout my years here. The first postdoc in the group was Michele Zaffalon. He set up a highly-reliable He3 system and taught me how to operate it - a skill which I have been putting into good use as all the results in this thesis are measured inside the He3 system. He was also an excellent source for electronic knowledge

from which I had learnt a lot.

Britt Baugher and Joel Wang, the first two to join the group as graduate students, did a lot of ordering at the initial stage when money was not abundant and each purchase required major research. Britt's knowledge on mechanical stuffs has been a great resource for the group. His superb organizing skill also put the overly crowded measurement lab into a much more spacious and pleasant room. Joel is the caretaker of our cryofree (but not problem-free) system. His genuine belief in the flip-chip bonder has contributed to the first graphene transfer method used in the group and in my experiments. His expertise on food also opened my tiny world to western cuisine and celebrity chefs as well as "Thailand" cafe. Leonardo Campos, who was a visiting graduate student and later joined the group as a postdoc, provided the needed humors during group meetings. His adventurous nature has led us to a more successful exfoliation technique. After many months delay due to Leonardo's faculty application process and my thesis writing, hopefully we will finish our trilayer graphene paper soon.

Shortly after I joined the group, Javier Sanchez-Yamagishi became a new member and has brought with him a lot of energy and random comments to the group. I have also benefitted greatly from his willingness to explore new ideas and methods, most notably his graphene transfer technique. Hadar Steinberg introduced me to a Shklovskii's book which resulted in my first PRL paper. His thirst for accurate answers to any ambiguous explanations has brought intellectual discussions to our group meetings and helped strengthen my physics knowledge.

Valla Fatemi, Qiong Ma, Yafang Yang, and Jason Luo form a new wave of graduate students, joining the group when it is quite well-established. Valla helped build a new breakout box for the He3 system which makes grounding and un-grounding devices

so much less painful and more reliable. I am also grateful for his help in proofreading this thesis. Qiong amazes me with her skill in juggling a shuttlecock and her ability to bring cuteness to her office door, a He dewar, and her photocurrent data. I wish you all productive Ph.D. careers and good luck with your qualifying exams.

Tchefor Ndukum, Nathan Gabor, Andrea Young, and Hugh Churchill joined the group as postdocs and have brought their own expertise to the group. To me, they all have one thing in common - I have known them way before they joined the group. Tchefor was a grader for my Solid State class at Cornell, although he did not remember me from that class. Nathan was collaborating with Ralph group in which I was a member during my time at Cornell. Andrea and I met during an open house at Columbia. I also worked with Hugh during my short period in Marcus group. The time I spent working with Hugh on carbon nanotube had best prepared me for graphene research, both on the fabrication and measurement techniques - I am still using the Elionix and the Igor. In addition to having known all of them before they joined the group, I know that they have one more thing in common - their passion in what they do after all those years in Ph.D.. Such passion is something I hope to emulate after leaving Harvard.

My graphene-on-hBN devices would not exist without the high-quality single crystal hBN generously provided to us by our Japanese collaborators, Kenji Watanabe and Takashi Taniguchi. I also would like to thank Mario Hofmann and Alfonso Reina from Jing Kong group who helped train me on how to use the AFM and the furnace in Jing Kong's lab. I also had a chance to collaborate with Han Wang from Palacios group who gave me a glimpse of the engineering world.

Most of the analysis and understanding of the data in this thesis would not have been possible without the helps from the theorists. Prof. Leonid Levitov has always

provided insight and guided us to literatures for any new data set we obtained. Prof. Edward McCann and Prof. Mikito Koshino were instrumental in helping us understand the quantum Hall effect in trilayer graphene and generously shared their manuscript on trilayer graphene with us before it was published. Leonardo and I also had a chance to collaborate with Dmitry Abanin and Maksym Serbyn on a new data on trilayer graphene with top gate. After a few meetings I have had with them, their insight on the material helps confirm that I have made the right choice pursuing my Physics Ph.D. as an experimentalist.

Working at MIT as a Harvard student requires a handful of paper work every semester. Our administrative assistant, Monica Wolf, has helped me tremendously with this process. In addition, she always made sure that our purchase orders, reimbursements, and CNS fees are taken care of.

Lastly, I am grateful to my parents for their constant support over the years. They have shown me, by example, that hard-working ethics is a prerequisite for any accomplishment. And while they did not have the luxury of a high-school education, they made sure that I had the best education possible. They were, indeed, the true starting point of this thesis.

Dedicated to my family

Chapter 1

Introduction

Graphene is a monolayer of graphite which has a honeycomb lattice structure. Its band structure was first analyzed theoretically in 1947 by P. R. Wallace [1]. Due to thermal fluctuations, a free-standing two-dimensional material would not be able to establish long-range order and cannot exist in nature [2]. However, in 2004, Geim *et al.* showed that graphene can be isolated from graphite by a mechanical exfoliation technique (or "scotch tape" technique) on a surface [3]. Its existence was later confirmed by an unusual half-integer quantum Hall effect [4, 5]. Since then, graphene has been a subject of extensive research due to its remarkable electronic, mechanical, optical, and chemical properties and potential for future applications. Electronically, its gapless linear band structure and the chiral nature of electrons in graphene as well as its tunability of charge density have led to the observation of new phenomena such as the half-integer quantum Hall effect [4, 5], the quantum Hall effect in PN junctions [6, 7], Klein tunneling [8, 9], and strain-induced pseudo-magnetic fields [10, 11]. Mechanically, graphene has been shown to be the strongest material ever measured, with a Young's modulus of 1 TPa and yet it

can be stretched elastically by up to 20% [12]. It is also impermeable to He gas [13]. Optically, graphene is nearly transparent with its opacity given by $\pi\alpha$ where α is the fine structure constant [14]. Due to its gapless band structure, graphene is ideal for broadband optoelectronic applications as electrons in graphene can be excited by photons over a wide range of energies. Chemically, graphene can be reversibly transformed from semi-metal to insulator by means of hydrogenation or fluorination with very uniform coverage [15–17].

In this thesis, I will focus on the electronic properties of mono-, bi-, and tri-layer graphene, an area which has been developed at an incredible pace both theoretically and experimentally. Even though graphene has such promising potential, progress has been hindered by the presence of impurities, which make graphene less pristine and which obscure the observation of some of the novel predicted phenomena. In the early phase of graphene research, 300-nm-thick SiO_2 was the most common substrate for electronic study because monolayer graphene can be easily identified under an optical microscope and it is also used as a gate to control electron density in graphene. Moreover, the standard fabrication process, which involves mechanical exfoliation of graphene directly onto SiO_2 and electron-beam lithography, also helped SiO_2 become the most common choice. However, the mobility of graphene on SiO_2 has been limited to $\sim$10,000 cm^2 V^{-1} s^{-1} which corresponds to a mean free path of $\sim$100 nm for a density $n \sim 10^{12}$ cm^{-2}. Therefore, electronic transport in graphene is in a diffusive regime because the separation between contacts is typically on the order of a micron.

Charged impurities trapped inside the oxide are believed to be a major source of scattering [18–21]. One possible way to improve graphene quality is to remove graphene from the SiO_2 substrate and leave it suspended [22,23]. This method has increased the mobility of graphene by one to two orders of magnitude to $\sim 10^5$–10^6 cm^2 V^{-1} s^{-1} [22–24] with

a mean free path reaching 1–10 μm. Such a long mean free path indicates that charge carriers now can travel ballistically across the sample without scattering. The high quality of suspended graphene has led to the observation of intriguing phenomena which would have been impossible for graphene on SiO_2 such as the fractional quantum Hall effect [25, 26] and the renormalization of Fermi velocity near the Dirac point in monolayer graphene [24], as well as interaction effects in bilayer graphene [27–31]. However, eliminating the substrate and leaving graphene suspended put major limitations on device geometry because suspended graphene can easily collapse. As a result, the majority of studies on suspended graphene so far has been performed on two-terminal geometry. In addition, suspended graphene is inevitably subjected to ripples and strain [32–34] which can effect its electronic properties in an unknown way [35–37].

Alternatively, instead of removing the SiO_2 substrate, searching for a new substrate to replace SiO_2 has also been pursued in order to find a perfect match for graphene and eliminate the disadvantages present in suspended graphene. Graphene on mica has been shown to improve its flatness [38] but device fabrication has proved to be challenging [39]. Eventually, a revolution came when Dean *et al.* employed hexagonal boron nitride (hBN) as a new substrate [40] and observed a significant increase in graphene mobility (60,000 and 80,000 $cm^2V^{-1}s^{-1}$ for monolayer and bilayer graphene respectively).

Hexagonal boron nitride has the same honeycomb lattice structure as graphene but with boron and nitrogen replacing carbon in the A and B sublattices. In addition, lattice constant in hBN is 1.8% longer than that of graphene [41]. Unlike graphene, which is a semi-metal, hBN is an insulator and, for the single crystals grown by Watanabe *et al.*, its direct band gap is 5.97 eV [42]. Due to the strong bonding between boron and nitrogen, hBN is expected to be free of dangling bonds and surface charge traps. STM studies of

graphene on hBN have also confirmed that the potential fluctuations and surface roughness in graphene on hBN are about an order of magnitude smaller than those on SiO_2 [43, 44]. Later studies have found mobilities $> 100,000$ $cm^2V^{-1}s^{-1}$ [45–48]. Even though graphene devices on hBN substrates require a complicated fabrication process involving graphene transfer, the fact that graphene is supported has allowed for a more complex device geometry than that in suspended graphene.

The data presented in this thesis have been taken on mono-, bi-, and tri-layer graphene devices. By adding one or two more layers onto monolayer graphene, its band structure becomes significantly modified and each one case possesses its own special electronic properties. Therefore, in Chapter 2 and Chapter 3, a detailed description of band structure and quantum Hall effect in mono-, bi-, and tri-layer graphene will be discussed. After these chapters, I will present the results from three experiments where the graphene's electronic transport properties vary from hopping to ballistic regimes:

- Chapter 4 explores the ability to open a band gap in dual-gated bilayer graphene by applying a perpendicular electric field and also the effect of disorder on the measured transport gap.

- Chapter 5 investigates quantum Hall effect and Landau level crossing in Bernal-stacked trilayer graphene which leads to the determination of the band parameters used to describe the peculiar band structure of Bernal-stacked trilayer graphene.

- Chapter 6 describes transverse magnetic focusing in mono-, bi-, and tri-layer graphene from low temperature to room temperature. The ability to tune electron density enables the use of transverse magnetic focusing to probe the change in trilayer graphene's band structure when subjected to an electric field.

Chapter 2

Band structure of mono-, bi-, and tri-layer graphene

2.1 Band structure of monolayer graphene

Monolayer graphene (MLG) has a honeycomb structure in which the unit cell contains two atoms, A and B sublattices (Fig. 2.1). The lattice vectors are given by

$$\boldsymbol{a}_1 = \frac{a}{2}(3, \sqrt{3}), \quad \boldsymbol{a}_2 = \frac{a}{2}(3, -\sqrt{3}) \tag{2.1}$$

where $a = 1.42$ Å is the distance between nearest neighbor atoms. It is worth noting that in the literature, a is sometimes denoted for the magnitude of the lattice vectors ($|\boldsymbol{a}_1| = |\boldsymbol{a}_2| = \sqrt{3} \times 1.42$ Å). However, in this thesis, I will use a as the distance between nearest neighbor atoms. The three nearest-neighbor vectors are

$$\boldsymbol{\delta}_1 = \frac{a}{2}(1, \sqrt{3}), \quad \boldsymbol{\delta}_2 = \frac{a}{2}(1, -\sqrt{3}), \quad \boldsymbol{\delta}_3 = -a(1, 0). \tag{2.2}$$

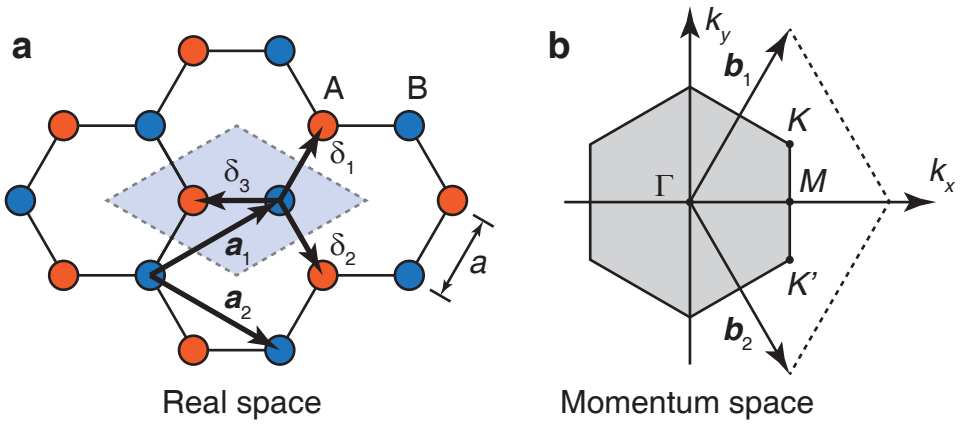

Figure 2.1: **a**, Crystal structure of monolayer graphene in real space. The shaded region at the center is a unit cell containing atoms in two sublattices, A and B. **b**, Crystal structure of monolayer graphene in reciprocal space. The vectors $\boldsymbol{b}_1$ and $\boldsymbol{b}_2$ are reciprocal lattice vectors and the shaded region is the first Brillouin zone.

In momentum space, the reciprocal-lattice vectors are given by

$$\boldsymbol{b}_1 = \frac{2\pi}{3a}(1, \sqrt{3}), \quad \boldsymbol{b}_2 = \frac{2\pi}{3a}(1, -\sqrt{3}). \tag{2.3}$$

The special points, which play an important role in the band structure of graphene at low energy, are K and K' located at the corners of the first Brillouin zone where the valence and conduction bands meet. These points are given by

$$\boldsymbol{K} = (\frac{2\pi}{3a}, \frac{2\pi}{3\sqrt{3}a}), \quad \boldsymbol{K}' = (\frac{2\pi}{3a}, -\frac{2\pi}{3\sqrt{3}a}) \tag{2.4}$$

Applying the tight-binding model and limiting oneself to hopping between nearest neighbors, one obtains the following Hamiltonian

$$H_{\mathrm{MLG}} = -\gamma_0 \sum_{\boldsymbol{R},\,\sigma} \Big[a_\sigma^\dagger(\boldsymbol{R}) b_\sigma(\boldsymbol{R}) + a_\sigma^\dagger(\boldsymbol{R}) b_\sigma(\boldsymbol{R} - \boldsymbol{a}_1) + a_\sigma^\dagger(\boldsymbol{R}) b_\sigma(\boldsymbol{R} - \boldsymbol{a}_2) + \mathrm{h.c.} \Big] \tag{2.5}$$

where $a_\sigma(\boldsymbol{R})$ ($a_\sigma^\dagger(\boldsymbol{R})$) is an annihilation (creation) operator of a spin-σ electron at sublattice A, site $\boldsymbol{R}$ and $\gamma_0 \approx 3.1$ eV is the hopping parameter between nearest neighbors [49]. One

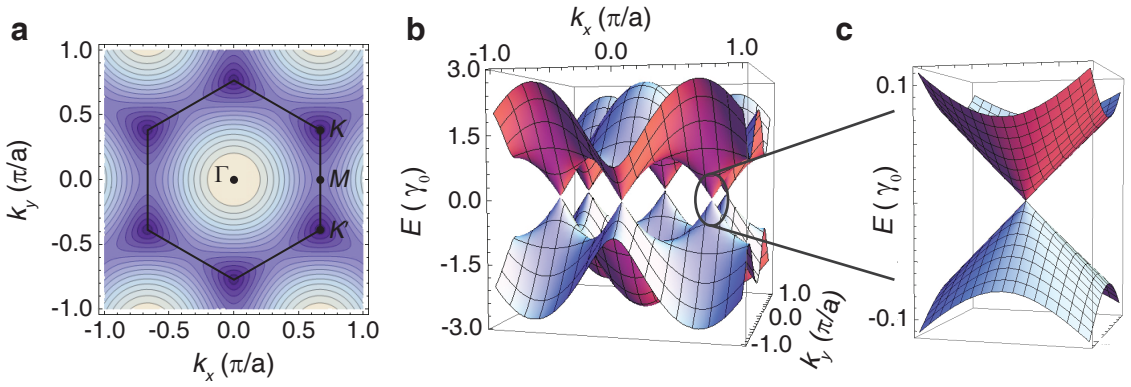

Figure 2.2: **a**, The energy contour plot of the conduction band of MLG (the darker the color, the lower the energy). The minimum energy of MLG's conduction band occurs at K and K' points. **b**, The band structure of MLG. **c**, Zoom-in of the band structure near one of the K-points. The valence and conduction bands meet at the K-points, leaving MLG as a gapless material. The Dirac cones can be seen clearly at low energy.

can diagonalize the Hamiltonian H_{MLG} by changing basis from real space to momentum space (Fourier transform) by substituting $a_\sigma(\boldsymbol{R}) = \dfrac{1}{\sqrt{N}} \sum_m e^{-i\vec{k}_m \cdot \vec{R}} a_{k_m,\sigma}$. The resulting Hamiltonian for the basis $\psi = (a_{k,\sigma}, b_{k,\sigma})$ is given by

$$H_{\mathrm{MLG}} = -\gamma_0 \begin{bmatrix} 0 & s^*(\boldsymbol{k}) \\ s(\boldsymbol{k}) & 0 \end{bmatrix} \tag{2.6}$$

where $s(k) = 1 + e^{i\boldsymbol{k}\cdot\boldsymbol{a}_1} + e^{i\boldsymbol{k}\cdot\boldsymbol{a}_2}$. Hence, the dispersion relation of MLG is

$$E_{\mathrm{MLG}}(k_x, k_y) = \pm\gamma_0 |s(\boldsymbol{k})| \tag{2.7}$$

$$= \pm\gamma_0 \sqrt{1 + 4\cos\left(\frac{\sqrt{3}}{2}k_y a\right)\cos\left(\frac{3}{2}k_x a\right) + 4\cos^2\left(\frac{\sqrt{3}}{2}k_y a\right)} \tag{2.8}$$

The band structure of MLG is shown in Fig. 2.2. Since one unit cell contains two carbon atoms and each one contributes one free electron, the band structure is half-filled ($E_{\mathrm{F}} = 0$).

One important aspect of MLG is that it is a gapless material. Its conduction and valence bands meet at the K and K' points (see Fig. 2.1 and 2.2) which makes MLG

a semi-metal. In a transport measurement, charge density can be typically tuned within $\pm 10^{13}$ cm^{-2} which corresponds to $\sim\pm 350$ meV. Such an energy scale is much smaller than γ_0 and therefore, in transport, charge carriers whose momentum is in the vicinity of the K and K' points can only be probed. By expanding H_{MLG} around one of the K points, one obtains the low energy H_{MLG} as follows:

$$H_{\mathrm{MLG}} = \frac{3\gamma_0 a}{2\hbar} \begin{bmatrix} 0 & p_x + i\xi p_y \\ p_x - i\xi p_y & 0 \end{bmatrix} = v_{\mathrm{F}} \boldsymbol{\sigma} \cdot \boldsymbol{p} \tag{2.9}$$

where $\boldsymbol{p} = \hbar \boldsymbol{k}$ is a momentum relative to the K or K' points, $\xi = \pm 1$ for K and K' respectively, $v_{\mathrm{F}} = 3\gamma_0 a/2\hbar$, and $\boldsymbol{\sigma}$ are the Pauli matrices. Equation 2.9 suggests that an electron in MLG is chiral in the sense that its pseudo-spin is tied to the direction of momentum. The components or direction of the pseudo-spin describe the weight of electron's wave function on A and B sublattices. The eigen-energy of H_{MLG} around the K points is then given by

$$E = \pm v_{\mathrm{F}} |\boldsymbol{p}| \tag{2.10}$$

This dispersion relation has the same functional form as that of a photon which implies that low energy electrons in MLG behave as a massless particle moving at the Fermi velocity of $v_{\mathrm{F}} \approx 1 \times 10^6$ m/s, independent of energy. This is vastly different from two-dimensional electron gas (2-DEG) in other systems such as semiconductor heterojunctions where electrons are massive and non-chiral with the dispersion relation of $E = \boldsymbol{p}^2/2m^*$. Hence, in this system, the Fermi velocity is $v_{\mathrm{F}} = p_{\mathrm{F}}/m^* = \sqrt{2E_{\mathrm{F}}/m^*}$ which depends on energy.

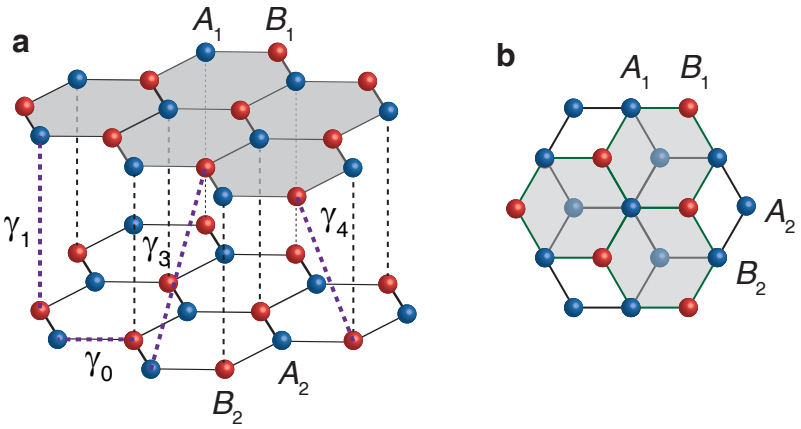

Figure 2.3: **a**, Crystal structure of Bernal-stacked BLG in which sublattice A_1 is sitting on top of sublattice B_2. The hopping parameters γ_0 and γ_1 describe the hopping between the nearest intra- and inter-layer respectively. The hopping parameters γ_3 and γ_4 describe the hopping between B_1 to A_2 and B_1 to B_2, respectively. **b**, A top view of **a**.

2.2 Band structure of bilayer graphene

2.2.1 Hamiltonian and dispersion relation of bilayer graphene

Bilayer graphene (BLG) consists of two layers of MLG, with one on top of the other. The most abundant stacking in nature is Bernal-stacking where sublattice A of the top layer and sublattice B of the bottom layer are vertically aligned (Fig. 2.3). The unit cell of BLG then consists of four atoms: A_1 and B_1 from the top layer and A_2 and B_2 from the bottom layer.

In addition to γ_0 which describes the nearest intra-layer hopping, one needs to introduce an extra parameter γ_1, the nearest inter-layer hopping energy between A_1 and B_2 whose value is $\sim$0.39 eV [49]. Taking only γ_0 and γ_1 into account, the Hamiltonian for

BLG can be written as [50]

$$H_{\mathrm{BLG}} = \sum_{i=1}^{2} H_i + \gamma_1 \sum_{\boldsymbol{R},\,\sigma} \Big[a^{\dagger}_{1,\,\sigma}(\boldsymbol{R}) b_{2,\,\sigma}(\boldsymbol{R}) + \mathrm{h.c.} \Big] + H_V \tag{2.11}$$

where H_i is the MLG Hamiltonian for layer i. The second term in Eq. 2.11 represents a hopping between A_1 and B_2 with the hopping energy of γ_1. The last term describes the potential difference V between the top and the bottom layers and is given by

$$H_V = \frac{V}{2} \sum_{\boldsymbol{R},\,\sigma} \left[n_{A1}(\boldsymbol{R}) + n_{B1}(\boldsymbol{R}) - n_{A2}(\boldsymbol{R}) - n_{B2}(\boldsymbol{R}) \right] \tag{2.12}$$

where n_{Ai} and n_{Bi} are number operators on sublattices A_i and B_i respectively. In experiments, a potential difference V can be induced by depositing alkali atoms or employing dual-gate geometry [51, 52].

The Hamiltonian H_{BLG} can again be diagonalized by changing the basis from real space to reciprocal space. The Hamiltonian in reciprocal space becomes

$$H_{\mathrm{BLG}} = \begin{bmatrix} V/2 & -\gamma_0 s(\boldsymbol{k}) & 0 & -\gamma_1 \\ -\gamma_0 s^*(\boldsymbol{k}) & V/2 & 0 & 0 \\ 0 & 0 & -V/2 & -\gamma_0 s(\boldsymbol{k}) \\ -\gamma_1 & 0 & -\gamma_0 s^*(\boldsymbol{k}) & -V/2 \end{bmatrix} \tag{2.13}$$

in the (A_1, B_1, A_2, B_2) basis. The eigen-energies are given by

$$E^{\pm\pm}_{\mathrm{BLG}} = \pm \sqrt{\frac{V^2}{4} + E^2_{\mathrm{MLG}}(\boldsymbol{k}) + \frac{\gamma_1^2}{2} \pm \sqrt{\frac{\gamma_1^4}{4} + (V^2 + \gamma_1^2) E^2_{\mathrm{MLG}}(\boldsymbol{k})}}. \tag{2.14}$$

Similar to MLG, low-energy states, whose momentum are around K or K' points, are relevant. Expanding $s(\boldsymbol{k})$ about these two points in momentum space yields $\gamma_0 s(\boldsymbol{k}) = v_{\mathrm{F}}(p_x + i\xi p_y)$ where $\xi = \pm 1$ for K and K' points respectively.

Since one unit cell contains four atoms, BLG consists of four subbands. Two of these four subbands are at low energy which can be accessible in transport experiments.

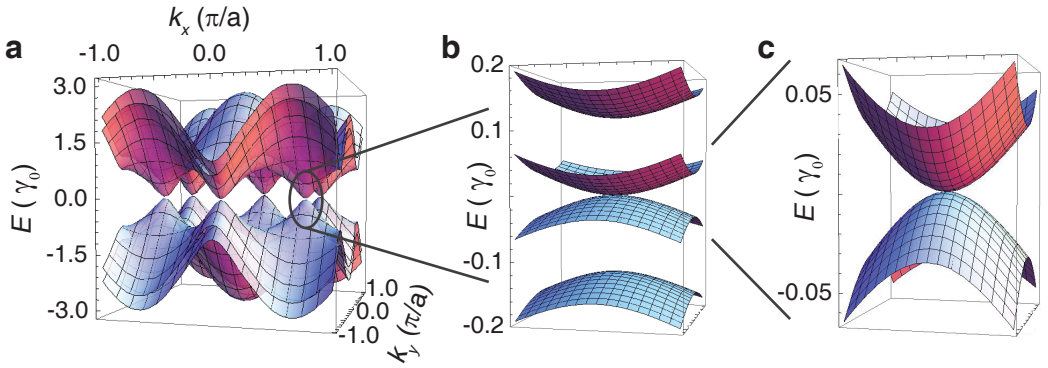

Figure 2.4: **a**, The band structure of BLG for $V = 0$. **b**, Zoom-in band structure in **a** near one of the K points, showing four subbands with two at low energy and the other two at high energy. **c**, Zoom-in band structure at low energy. The valence and conduction bands meet at K points similar to MLG but the dispersion relation in BLG is now parabolic instead of linear as in MLG.

The other two subbands reside at higher energy (shifted from zero energy by $\gamma_1 \sim 0.39$ eV). These two high-energy subbands are hardly involved and/or accessible in a typical transport measurement, except those which use electrolyte gating techniques which can induce density high enough to reach the higher energy subbands [53].

Since the two high-energy subbands do not contribute to a usual transport experiment, it is desirable to obtain a hamiltonian at low energy, which involves only electrons on A_2 and B_1. Electrons which live on A_1 and B_2 gain an extra kinetic energy γ_1 owing to the inter-layer hopping and hence exist in the high-energy subbands. The low energy hamiltonian about the K point is given by [54]

$$H_{\mathrm{BLG}} = -\frac{1}{2m^*}\begin{bmatrix} 0 & (\pi^\dagger)^2 \\ \pi^2 & 0 \end{bmatrix} + V\left(\frac{1}{2}\begin{bmatrix} 1 & 0 \\ 0 & -1 \end{bmatrix} - \frac{v_{\mathrm{F}}^2}{\gamma_1^2}\begin{bmatrix} \pi^\dagger\pi & 0 \\ 0 & -\pi\pi^\dagger \end{bmatrix}\right) \tag{2.15}$$

where $m^* = \gamma_1/(2v_{\mathrm{F}}^2) \sim 0.034 m_e$ and $\pi = p_x + ip_y$.

When the potential difference between the layers is zero ($V = 0$), the dispersion

relation of BLG becomes parabolic with $E = \pm p^2/2m^*$ (Fig. 2.4) as opposed to the linear dispersion found in MLG. In addition, even though the dispersion in BLG is similar to those in semiconductor heterostructures, electrons in BLG behave as massive Dirac fermions owing to the chiral nature of the dispersion relation arising from the two component wave function.

2.2.2 Band gap opening in bilayer graphene

One unique property of BLG is that a band gap opens in its band structure if a potential difference V exists between the layers. One of the most common ways to achieve this is by using top and back gates. These two gates allow for control of density n and electric displacement field D independently. By applying a displacement field normal to the BLG plane, a potential difference is induced between layers and the inversion symmetry of BLG is broken. As a result, a band gap can be opened in BLG.

One can investigate the behavior of the band structure for finite V by expanding Eq. 2.14 with the assumption $v_{\mathrm{F}}p \ll V \ll \gamma_1$. The expansion yields [50]

$$E^{\pm -}_{\mathrm{BLG}}(V,p) \approx \pm\frac{V}{2} \mp \frac{V v_{\mathrm{F}}^2}{\gamma_1^2}p^2 \pm \frac{v_{\mathrm{F}}^4}{\gamma_1^2 V}p^4, \tag{2.16}$$

which results in a "Mexican hat" dispersion (Fig. 2.5b) [55].

Due to this Mexican hat dispersion, the band gap Δ_g between conduction and valence bands is located at finite momentum $p = \dfrac{(2\gamma_1^2+V^2)}{4(\gamma_1^2+V^2)}\dfrac{V^2}{v_{\mathrm{F}}^2}$ and equal to $\Delta_g = \sqrt{\dfrac{\gamma_1^2V^2}{(\gamma_1^2+V^2)}}$. For $V \ll \gamma_1$, the band gap $\Delta_g \sim V$, which explains the flat band observed in Fig. 2.5, because the gap at $p = 0$ is equal to V. As V is increased, the band gap will saturate at γ_1 [49, 50].

Unlike MLG whose gapless nature remains valid even after electric field is ap-

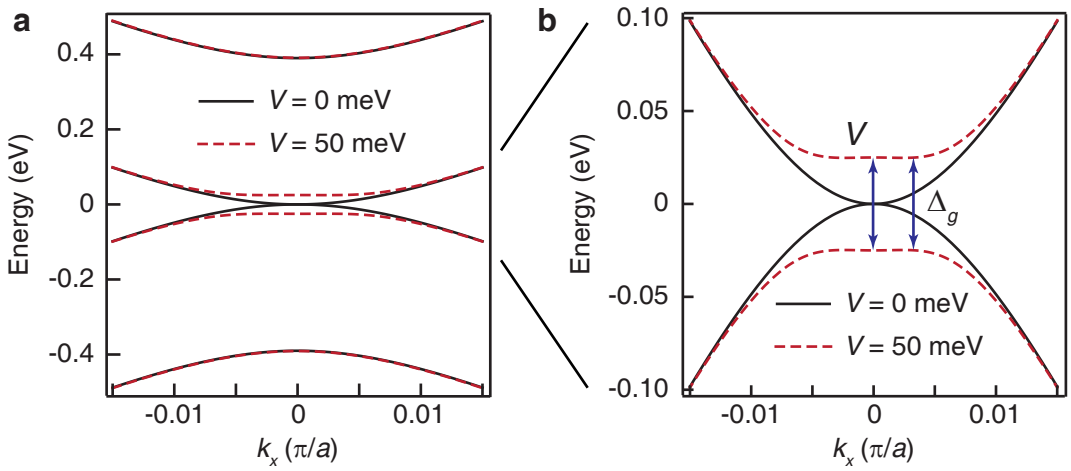

Figure 2.5: **a**, BLG band structure when $V = 0$ (black lines) and $V = 50$ meV (red dashed lines). The two high energy bands are shifted from zero energy by γ_1. **b**, Zoom-in plot of **a**. When $V = 0$ (black lines), BLG has zero band gap. The red dashed lines are the band structure when $V = 50$ meV, showing a maxican hat dispersion.

plied, the ability to induce a band gap has attracted significant interest in using the BLG to replace silicon in semiconductor devices. Such a band gap would allow a higher current on/off ratio as density is tuned across the charge neutrality point. However, disorder still remains a challenge for researchers to fully utilize BLG. Since disorder can cause potential fluctuations resulting in electron-hole puddles near the charge neutrality point [56], electrons can hop between different puddles which reduces the current on/off ratio significantly. This issue will be discussed in detail in Chapter 4.

2.2.3 Trigonal warping and electron-hole asymmetry

Up to now, only the nearest intra- and inter-layer hopping parameters γ_0 and γ_1 have been taken into account. In this section, two additional hopping parameters will be considered, namely γ_3, which describes the coupling between B_1 and A_2, and γ_4 which

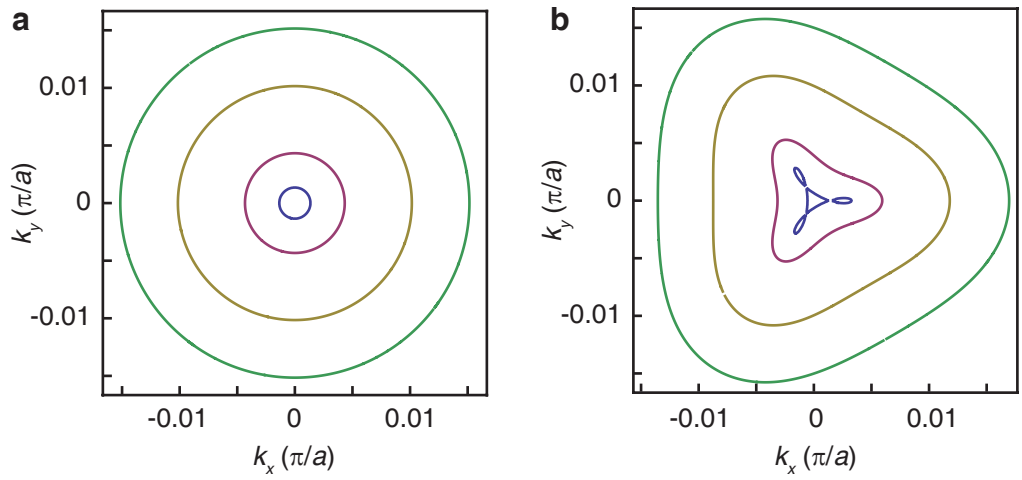

Figure 2.6: **a**, Fermi surface of BLG when $\gamma_3 = 0$ for $E_F = 1$, 10, 50, 100 meV (inner to outer circles). **b**, Fermi surface of BLG when $\gamma_3 = 0.315$ eV for the same Fermi energies as in **a**. The trigonal warping effect can be seen clearly as a result of finite γ_3. In addition, at low energy, the Fermi surface deforms into four separate pockets. $\gamma_4 = 0$ for both panels.

describes the coupling between A_1 and A_2 or B_1 and B_2 (Fig. 2.3). Incorporating these two parameters, one obtains the following Hamiltonian [57]:

$$H_{\mathrm{BLG}} = \begin{bmatrix} V/2 & v_F\pi^\dagger & -v_4\pi & \gamma_1 \\ v_F\pi & V/2 & v_3\pi^\dagger & -v_4\pi \\ -v_4\pi^\dagger & v_3\pi & -V/2 & v_F\pi^\dagger \\ \gamma_1 & -v_4\pi^\dagger & v_F\pi & -V/2 \end{bmatrix} \tag{2.17}$$

where $v_i = 3\gamma_i a/2\hbar$. The parameters I use here follow the convention of the Slonczewski-Weiss-McClure parameterization [58].

Let me first consider the effect of γ_3. This hopping parameter deforms the Fermi surface from circular to triangle-like shapes as shown in Fig. 2.6. This effect is called trigonal warping. In addition, at low energy, one observes Lifshitz transition at which a single Fermi surface splits into four separate pockets (Fig. 2.6). For $\gamma_3 = 0.315$ eV, the

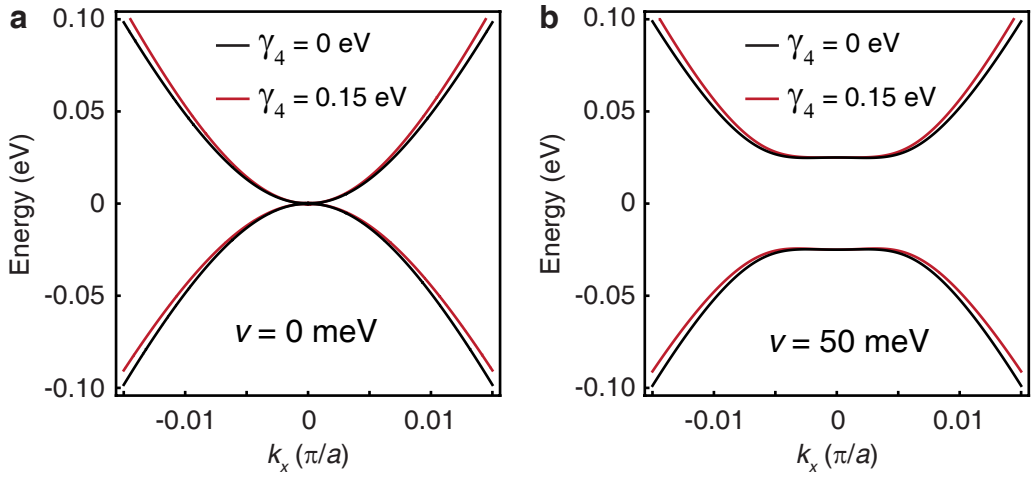

Figure 2.7: **a**, Low energy band structures of BLG for $V = 0$ meV when $\gamma_4 = 0$ eV (black line) and $\gamma_4 = 0.15$ eV (red line). Electron-hole asymmetry can be seen when $\gamma_4 \neq 0$ as the valence band is larger than the conduction band. **b**, Low energy band structures of BLG for $V = 50$ meV when $\gamma_4 = 0$ eV (black line) and $\gamma_4 = 0.15$ eV (red line). Similar Electron-hole asymmetry is also present.

Lifshitz transition occurs at $E \sim 1$ meV which corresponds to a very small density of $1 \times 10^{10}\text{cm}^{-2}$ or 140 mV in back gate voltage for a typical 300 nm SiO_2 dielectric. Hence, an extremely high quality sample is needed in order to observe the Lifshitz transition.

Another small correction to BLG's band structure comes from the γ_4 hopping parameter. Its value reported in literature is determined experimentally from graphite or theoretically from first principles calculation and ranges from a few tens of meV to a hundred meV [49, 58]. The effect of γ_4 is to introduce electron-hole asymmetry to the band structure as shown in Fig. 2.7.

2.3 Band structure of trilayer graphene

The two common stackings in trilayer graphene (TLG) are Bernal (ABA) and rhombohedral (ABC). A study employing Raman spectroscopy has found that, for many exfoliated TLG flakes, about 85 % of the TLG area is ABA stacking while the other 15 % is ABC stacking [59]. Due to their difference in stacking, ABA and ABC trilayer graphenes have vastly different electronic properties. For ABC, the crystal structure has inversion symmetry while ABA does not. This implies that the valley degeneracy for ABC is protected [60]. However, even though ABA's crystal structure does not have inversion symmetry, it possesses mirror symmetry which allows for a decomposition of the ABA Hamiltonian into monolayer and bilayer Hamiltonians.

2.3.1 Simple model band structure

I first concentrate on a simple model in which only γ_0 and γ_1 are considered. This will provide a general idea of the difference among MLG, BLG, and TLG as well as the difference between ABA and ABC. In addition, I will continue to consider momentum in the vicinity of the K point, which is accessible in a transport experiment.

ABC trilayer graphene

For ABC trilayer graphene, the nearest inter layer hopping parameter γ_1 connects between $B1$ and $A2$ as well as $B2$ and $A3$. The Hamiltonian is given by, in the basis of

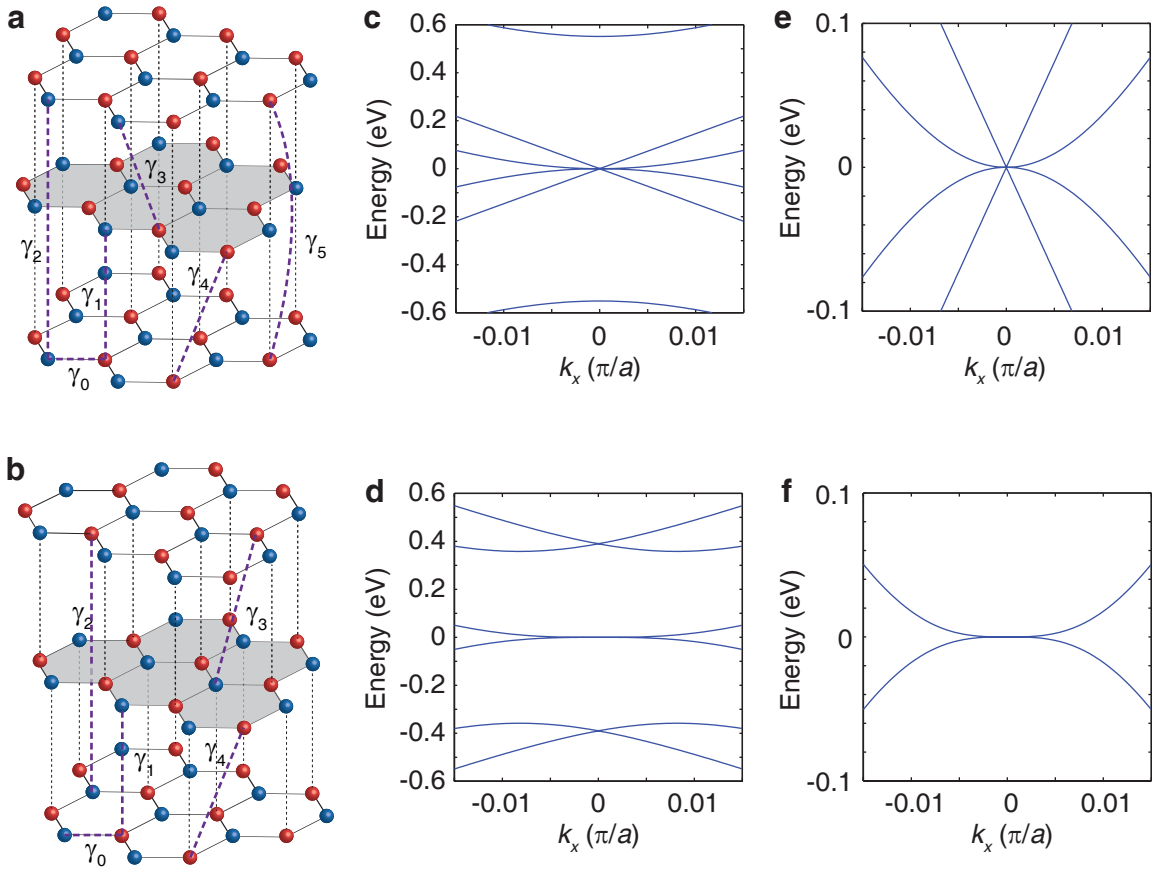

Figure 2.8: **a-b**, Crystal structures of ABA and ABC trilayer graphene respectively. **c-d**, Band structures of ABA and ABC trilayer graphene when only γ_0 and γ_1 are taken into account. **e-f**, Low-energy band structure of ABA and ABC trilayer graphene when only γ_0 and γ_1 are taken into account. ABA trilayer graphene has two subbands at low energy while ABC trilayer graphene only has one.

$A1$, $B1$, $A2$, $B2$, $A3$, and $B3$,

$$H_{ABC} = \begin{bmatrix} U_1 & v_F\pi^\dagger & 0 & 0 & 0 & 0 \\ v_F\pi & U_1 & \gamma_1 & 0 & 0 & 0 \\ 0 & \gamma_1 & U_2 & v_F\pi^\dagger & 0 & 0 \\ 0 & 0 & v_F\pi & U_2 & \gamma_1 & 0 \\ 0 & 0 & 0 & \gamma_1 & U_3 & v_F\pi \\ 0 & 0 & 0 & 0 & v_F\pi^\dagger & U_3 \end{bmatrix} \tag{2.18}$$

where U_i is the onsite potential for layer i. Such Hamiltonian results in three subbands, one at low energy and the other two at high energy (Fig. 2.8). Similar to BLG, those two bands at high energy are not relevant for a typical transport experiment. Hence, a low energy effective Hamiltonian provides better insight into the system better than the full 6×6 Hamiltonian. The two-component Hamiltonian in the basis of $A1$ and $B3$ is [61]

$$H_{ABC}^{(\text{eff})} = \frac{v_F^3}{\gamma_1^2}\begin{bmatrix} 0 & (\pi^\dagger)^3 \\ \pi^3 & 0 \end{bmatrix} + \Delta_1\left(1 - \frac{v_F^2p^2}{\gamma_1^2}\right)\begin{bmatrix} 1 & 0 \\ 0 & -1 \end{bmatrix} + \Delta_2\left(1 - \frac{3v_F^2p^2}{\gamma_1^2}\right)\begin{bmatrix} 1 & 0 \\ 0 & 1 \end{bmatrix} \tag{2.19}$$

where $\Delta_1 = (U_1 - U_3)/2$ and $\Delta_2 = (U_1 - 2U_2 + U_3)/6$. When $\Delta_1 = \Delta_2 = 0$ (no potential difference between layers is induced), the dispersion relation for ABC trilayer is $E = \pm v_F^3p^3/\gamma_1^2$ (Fig. 2.8f) in contrast to $E = v_Fp$ in MLG or $E = v_F^2p^2/\gamma_1$ in BLG. The second term on the right hand side of Eq. 2.19 involves the potential difference between the top and bottom layers Δ_1. This term is responsible for the opening of the band gap as an electric field is applied normal to the graphene plane [62, 63]. The third term results in a shift in energy as both diagonal elements have the same sign. The value of Δ_2 is typically very small compared to Δ_1 as it involves a non-linear part of the screening which is a second order effect.

ABA trilayer graphene

For *ABA* trilayer graphene, the nearest-neighbor inter layer hopping parameter γ_1 connects between $B1$ and $A2$ as well as $A2$ and $B3$ (in contrast to $B2$ and $A3$ in ABC trilayer graphene). The Hamiltonian is given by, in the basis of $A1$, $B1$, $A2$, $B2$, $A3$, and $B3$ [60],

$$H_{ABA} = \begin{bmatrix} U_1 & v_{\mathrm{F}}\pi & 0 & 0 & 0 & 0 \\ v_{\mathrm{F}}\pi & U_1 & \gamma_1 & 0 & 0 & 0 \\ 0 & \gamma_1 & U_2 & v_{\mathrm{F}}\pi^\dagger & 0 & \gamma_1 \\ 0 & 0 & v_{\mathrm{F}}\pi & U_2 & 0 & 0 \\ 0 & 0 & 0 & 0 & U_3 & v_{\mathrm{F}}\pi^\dagger \\ 0 & 0 & \gamma_1 & 0 & v_{\mathrm{F}}\pi & U_3 \end{bmatrix} \tag{2.20}$$

In order to obtain insight into H_{ABA}, the current basis is transformed into a new basis which respects the mirror reflection symmetry in *ABA* trilayer graphene, namely $(A1 - A3)/\sqrt{2}$, $(B1 - B3)/\sqrt{2}$, $(A1 + A3)/\sqrt{2}$, $B2$, $A2$, and $(B1 + B3)/\sqrt{2}$. Under this new basis, the Hamiltonian reads

$$H_{ABA} = \begin{bmatrix} H_m & \Xi \\ \Xi^\dagger & H_b \end{bmatrix}, \tag{2.21}$$

where

$$\Xi = \begin{bmatrix} \Delta_1 & 0 & 0 & 0 \\ 0 & 0 & 0 & \Delta_1 \end{bmatrix}, \qquad H_m = \begin{bmatrix} \Delta_2 & v_{\mathrm{F}}\pi^\dagger \\ v_{\mathrm{F}}\pi & \Delta_2 \end{bmatrix}, \tag{2.22}$$

and

$$H_b = \begin{bmatrix} \Delta_2 & 0 & 0 & v_{\mathrm{F}}\pi^\dagger \\ 0 & -2\Delta_2 & v_{\mathrm{F}}\pi & 0 \\ 0 & v_{\mathrm{F}}\pi^\dagger & -2\Delta_2 & \sqrt{2}\gamma_1 \\ v_{\mathrm{F}}\pi & 0 & \sqrt{2}\gamma_1 & \Delta_2 \end{bmatrix}. \tag{2.23}$$

One important feature, under the new basis, is that the Hamiltonian can be decomposed into MLG-like and BLG-like Hamiltonians H_m and H_b respectively. The only difference is that, in the BLG-like H_b, the nearest inter-layer coupling γ_1 becomes $\sqrt{2}\gamma_1$. When $\Delta_1 = 0$, the off-diagonal block Ξ is zero and MLG-like and BLG-like sectors do not interact. Hence, at low energy, the band structure of ABA trilayer graphene consists of a linear dispersion from the MLG-like subband and a parabolic dispersion from the BLG-like subband (Fig. 2.8c and e).

2.3.2 Full-parameter model band structure

The hopping parameters γ_0 and γ_1 are generally enough to explain most experimental data in MLG and BLG. However, it has been shown that higher order hopping parameters are necessary in order to explain the quantum Hall effect found in ABA trilayer graphene which will be discussed in detail in chapter 5 [46]. Therefore, in this section, a full-parameter model will be used to consider the band structures of ABA and ABC trilayer graphene. The parameters I use here will follow the convention from Slonczewski, Weiss, and McClure (SWMcC) [58]. In addition to γ_0 and γ_1, I have already discussed the effect of γ_3 and γ_4 in the BLG section. For TLG, the extra parameters have to be introduced in order to fully describe the band structure are γ_2, γ_5, and δ.

The parameters γ_2 and γ_5 describe the hopping energy between vertically aligned sites from layers 1 and 3 without and with a site in between from the middle layer, respectively. Therefore, γ_2 connects $A1$ and $A3$ lattice sites for ABA trilayer graphene and $A1$ and $B3$ lattice sites for ABC trilayer graphene, while γ_5 is only present in ABA trilayer graphene and connects $B1$ and $B3$. (Fig. 2.8a and b). Finally, δ describes the on-site energy difference between $A1$, $B2$, $A3$ and $B1$, $A2$, $B3$ in ABA trilayer graphene. The

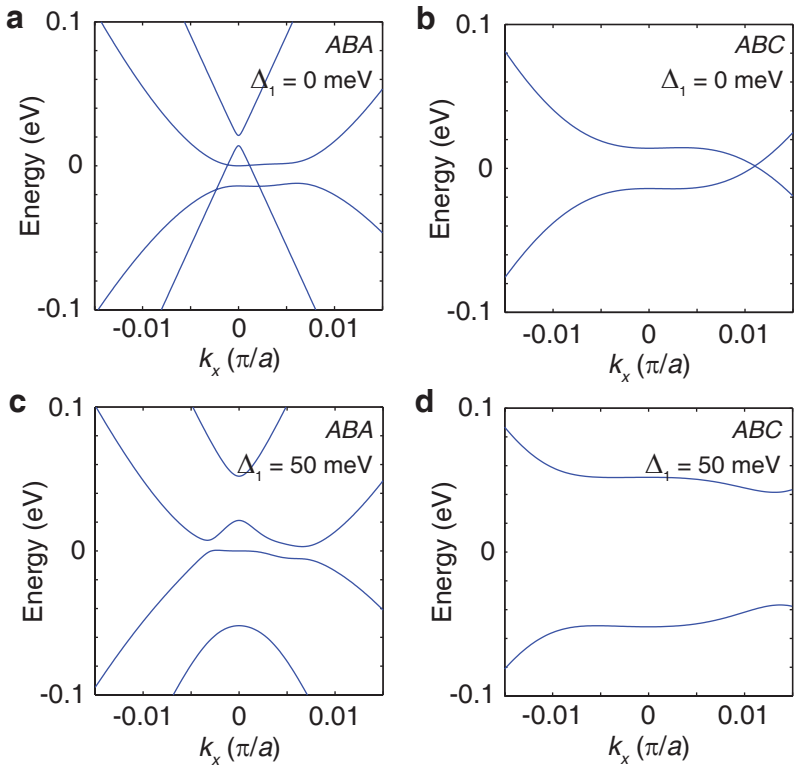

Figure 2.9: **a-b**, Band structures of ABA and ABC trilayer graphene with the following hopping parameters $\gamma_0 = 3.1$, $\gamma_1 = 0.39$, $\gamma_2 = -0.028$, $\gamma_3 = 0.315$, $\gamma_4 = 0.041$, $\gamma_5 = 0.05$, $\delta = 0.046$ eV, and $\Delta_1 = \Delta_2 = 0$ meV. **c-d** Band structures of ABA and ABC trilayer graphene with the same hopping parameters as in **a** and **b** but with $\Delta_1 = 50$ meV and $\Delta_2 = 0$ meV.

full-parameter Hamiltonians for ABC and ABA trilayer graphene are given by [61] in the basis of $A1$, $B1$, $A2$, $B2$, $A3$, $B3$

$$H_{ABC} = \begin{bmatrix} U_1 & v_F\pi^\dagger & -v_4\pi^\dagger & v_3\pi & 0 & \gamma_2/2 \\ v_F\pi & U_1 & \gamma_1 & -v_4\pi^\dagger & 0 & 0 \\ -v_4\pi & \gamma_1 & U_2 & v_F\pi^\dagger & -v_4\pi^\dagger & v_3\pi \\ v_3\pi^\dagger & -v_4\pi & v_F\pi & U_2 & \gamma_1 & -v_4\pi^\dagger \\ 0 & 0 & -v_4\pi & \gamma_1 & U_3 & v_F\pi \\ \gamma_2/2 & 0 & v_3\pi^\dagger & -v_4\pi & v_F\pi^\dagger & U_3 \end{bmatrix} \tag{2.24}$$

and

$$H_{ABA} = \begin{bmatrix} U_1 & v_F\pi & -v_4\pi^\dagger & v_3\pi & \gamma_2/2 & 0 \\ v_F\pi & U_1+\delta & \gamma_1 & -v_4\pi^\dagger & 0 & \gamma_5/2 \\ -v_4\pi & \gamma_1 & U_2+\delta & v_F\pi^\dagger & -v_4\pi & \gamma_1 \\ v_3\pi^\dagger & -v_4\pi & v_F\pi & U_2 & v_3\pi^\dagger & -v_4\pi \\ \gamma_2/2 & 0 & -v_4\pi^\dagger & v_3\pi & U_3 & v_F\pi^\dagger \\ 0 & \gamma_5/2 & \gamma_1 & -v_4\pi^\dagger & v_F\pi & U_3+\delta \end{bmatrix} \tag{2.25}$$

For H_{ABA}, one changes the basis to reflect the mirror symmetry, similar to the simple model case. As a result, H_{ABA} becomes

$$H_{ABA} = \begin{bmatrix} H_m & \Xi \\ \Xi^\dagger & H_b \end{bmatrix}, \tag{2.26}$$

where

$$\Xi = \begin{bmatrix} \Delta_1 & 0 & 0 & 0 \\ 0 & 0 & 0 & \Delta_1 \end{bmatrix}, \quad H_m = \begin{bmatrix} \Delta_2 - \gamma_2/2 & v_F\pi^\dagger \\ v_F\pi & \Delta_2 - \gamma_5/2 + \delta \end{bmatrix},$$

$$H_b = \begin{bmatrix} \Delta_2 + \gamma_2/2 & \sqrt{2}v_3\pi & -\sqrt{2}v_4\pi^\dagger & v_F\pi^\dagger \\ \sqrt{2}v_3\pi^\dagger & -2\Delta_2 & v_F\pi & -\sqrt{2}v_4\pi \\ -\sqrt{2}v_4\pi & v_F\pi^\dagger & -2\Delta_2 + \delta & \sqrt{2}\gamma_1 \\ v_F\pi & -\sqrt{2}v_4\pi^\dagger & \sqrt{2}\gamma_1 & \Delta_2 + \gamma_5/2 + \delta \end{bmatrix}.$$

Even though a few extra parameters have been included to H_{ABA}, its general characteristics remain unchanged: H_{ABA} can still be divided into MLG-like and BLG-like sectors with the same off-diagonal matrix Ξ. The difference between H_{BLG} and H_b (the BLG-like sector of H_{ABA}) is that γ_1, v_3, and v_4 become $\sqrt{2}\gamma_1$, $\sqrt{2}v_3$, and $\sqrt{2}v_4$.

The band structures for ABA and ABC trilayer graphene with the full parameter model are shown in Fig. 2.9 for $\Delta_1 = 0$ and 50 meV and $\Delta_2 = 0$. The values of the SWMcC parameters are taken from Taychatanapat *et al.* on ABA trilayer graphene [46]. For ABA trilayer graphene (Fig. 2.9a), the MLG-like and BLG-like subbands are present with small band overlap between them. This band overlap and the small band gap in the MLG-like and BLG-like subbands are due to finite γ_2, γ_5, and δ, which appear in the diagonal elements of H_m and H_b causing the bands to shift relatively in energy. For ABC trilayer graphene (Fig. 2.9b), the p^3 dispersion relation from the simple model is no longer the case. A finite value of γ_3 induces trigonal warping and causes the valence and conduction bands to meet at finite momenta instead of at the K point.

The potential difference Δ_1 also has different effects on ABA and ABC trilayer graphene. For ABA trilayer graphene, a finite value of Δ_1 results in a non-zero off diagonal matrix Ξ (Eq. 2.26) which causes hybridization between monolayer- and bilayer-like subbands. As a result, a small band gap opens near zero energy and the monolayer-like subband shifting away from zero energy (Fig. 2.9c). For ABC trilayer graphene, a finite

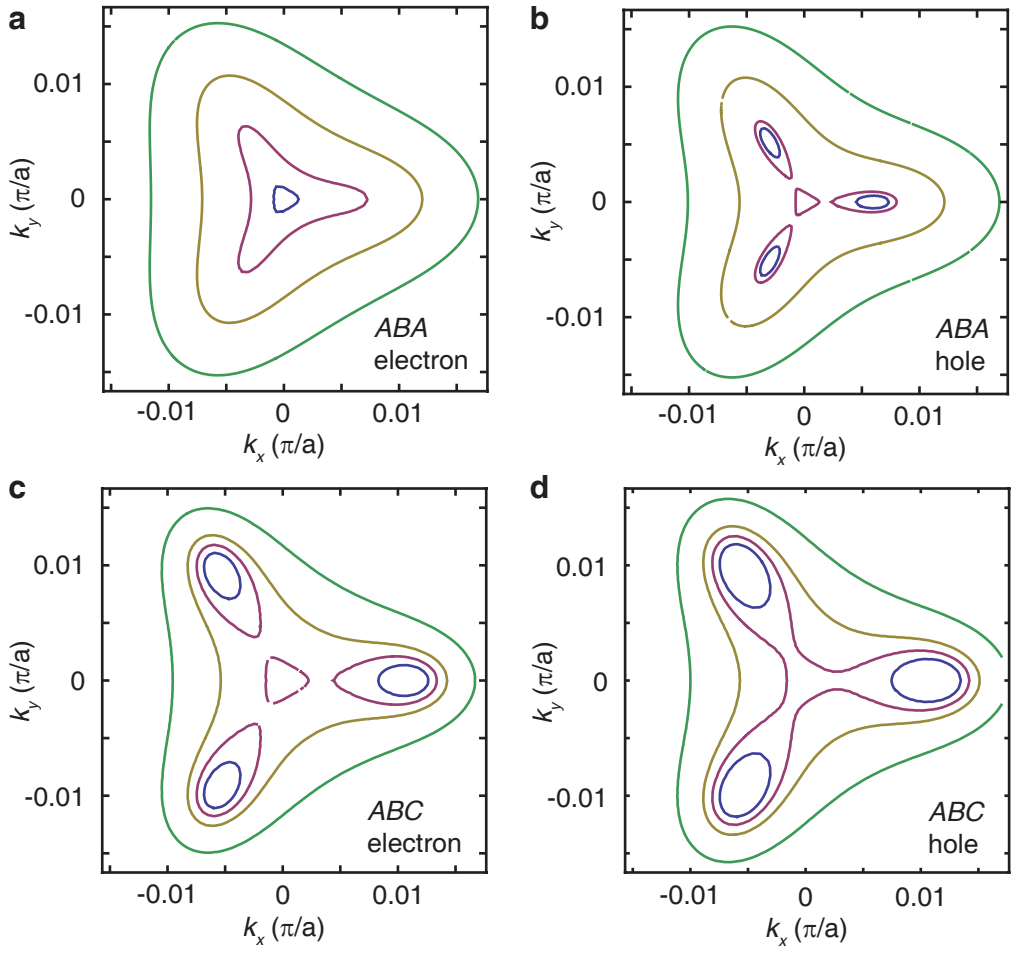

Figure 2.10: **a**, Fermi surface of ABA trilayer graphene in the electron regime with the same band parameters as in Fig. 2.9a for $E_F = 0.4$, 5, 30, 70 meV (from blue to green lines). **b**, Fermi surface of ABA trilayer graphene in the hole regime for $E_F = -13$, -14.2, -30, -60 meV. **c**, Fermi surface of ABC trilayer graphene in the electron regime with the same band parameters as in Fig. 2.9b for $E_F = 10$, 14.3, 20, 38 meV. **d**, Fermi surfaces of ABC trilayer graphene in the hole regime for $E_F = -10$, -14.3, -20, -38 meV.

Δ_1 induces a sizable band gap opening, larger than BLG for the same displacement field.

A Lifshitz transition may be more easily observed in ABC trilayer graphene as it occurs at a much higher density than in BLG. For example, using band parameters obtained from ABA trilayer graphene, the density needed to observe the Lifshitz transition in ABC trilayer graphene is about $7 \times 10^{11}\text{cm}^{-2}$ for electron regime and $-6 \times 10^{11}\text{cm}^{-2}$ for hole regime, corresponding to back gate voltage of 9.8 and -8.4 V for 300 nm SiO_2 dielectric. These densities are almost two orders of magnitude larger than the density for the Lifshitz transition in BLG ($\sim 1 \times 10^{10}\text{cm}^{-2}$).

2.4 Interaction effects on band structure

In an ultra-clean sample, the band structure in graphene can get modified due to interaction effects. For example, in a suspended monolayer graphene, the Fermi velocity v_F which is supposed to be a constant in the single-particle picture increases at low density and reaches 3×10^6 m/s at $n < 10^{10}$ cm^{-2}, three times higher than the typical value observed in a more disordered sample [24]. Electron-electron interactions are believed to play a major role as screening becomes increasingly weaker at low density. In bilayer graphene, while the non-interacting model results in a gapless band structure, electron-electron interactions can lead to a finite band gap at zero electric field and zero magnetic field [28, 30, 31].

Furthermore, interaction with a substrate can also lead to a change in band structure. For example, graphene on hBN forms an angle-dependent moiré pattern. As a result, graphene is subjected to a weak periodic potential from hBN substrates. Such a potential induces a formation of new superlattice Dirac peaks at higher energy [64] and Hofstadter's butterfly at finite magnetic field [65, 66].

Chapter 3

Quantum Hall effect in mono-, bi-, and tri-layer graphene

The quantum Hall effect (QHE) is a phenomenon which occurs in a two-dimensional electron gas (2DEG). When electrons in a 2DEG are subjected to a high magnetic field, its Hall resistance becomes quantized at some integer multiple of $h/e^2 = 25.81\ \mathrm{k}\,\Omega$, instead of being linear with magnetic field. It was first discovered in the inversion layer of MOSFETs in the 1980s by K. von Klitzing, G. Dorda and M. Pepper [67]. Later, most QHE experiments were performed on high-quality semiconductor heterostructures, particularly on gallium arsenide. Graphene also hosts a 2DEG whose electrons behave as Dirac fermions, as opposed to normal massive electrons in the semiconductor heterostructures. As a result, the QHE in graphene has become one of the most intense research topics in recent years.

3.1 Introduction to quantum Hall effect

Semiclassically, electrons in an applied magnetic field will experience the Lorentz force forcing them to move in a closed orbit, obeying the following equation of motion

$$\hbar \frac{\mathrm{d}}{\mathrm{d}t}\boldsymbol{k} = (-e)\frac{\mathrm{d}}{\mathrm{d}t}\boldsymbol{r} \times \boldsymbol{B}. \tag{3.1}$$

Even though this semiclassical picture can be used to explain some phenomena, such as the classical Hall effect and transverse magnetic focusing, which will be discussed in detail in Chapter 6, it fails to explain the quantization of the Hall conductance in the quantum Hall effect. A fully quantum-mechanical treatment is required in order to explain such quantization.

Landau level for a non-relativistic particle

The non-relativistic hamiltonian for an electron in semiconductor heterostructures is simply a free electron $H = p^2/2m^*$ where m^* is the effective mass. At zero magnetic field, the density of states (DoS) is constant and given by $\mathrm{DoS} = g_s g_v \dfrac{m}{2\pi\hbar^2}$ where g_s and g_v are spin and valley degeneracies. Once a magnetic field is applied perpendicular to the plane $B = B\hat{z}$, the momentum operator will be transformed to

$$\boldsymbol{p} \to \Pi = \boldsymbol{p} + e\boldsymbol{A}(\boldsymbol{r}) \tag{3.2}$$

where A is the vector potential obeying the identity $\nabla \times \boldsymbol{A} = \boldsymbol{B}$. Here, I will use the Landau gauge $\boldsymbol{A}_L(\boldsymbol{r}) = B(-y, 0, 0)$ which yields the following Hamiltonian

$$H = \frac{[\boldsymbol{p} + e\boldsymbol{A}(\boldsymbol{r})]^2}{2m^*} = \frac{1}{2m^*}\left(p_x - eBy\right)^2 + p_y^2 \tag{3.3}$$

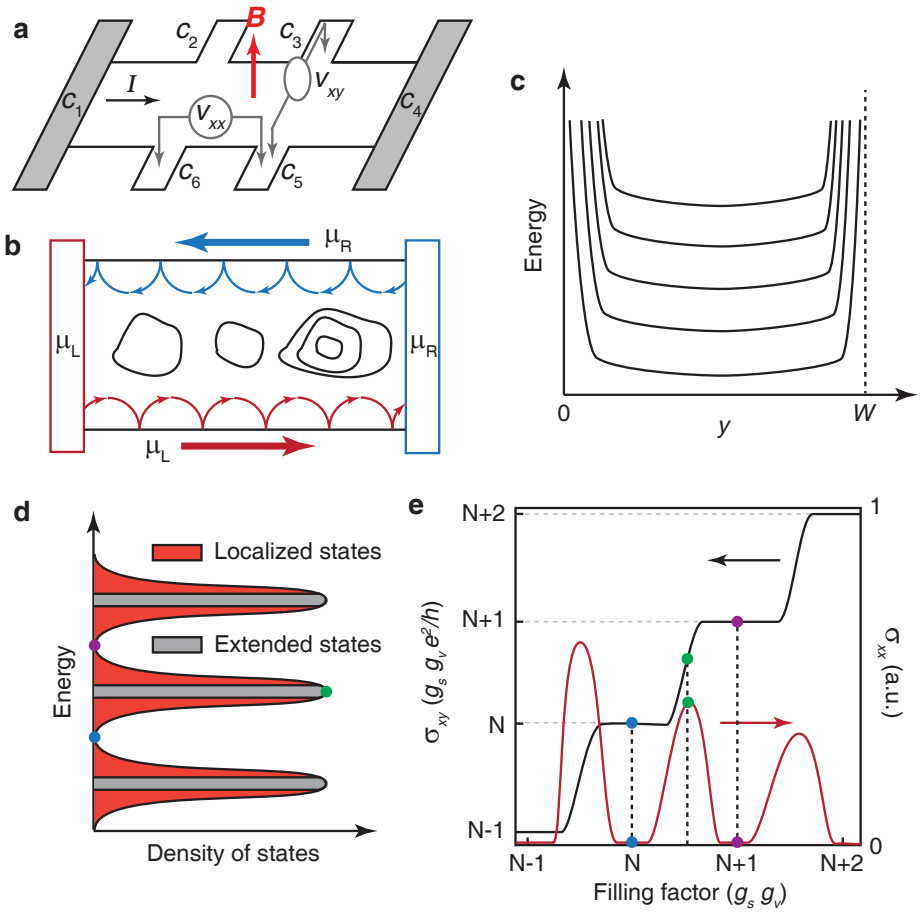

Figure 3.1: **a**, Hall bar geometry with four-terminal measurement configuration. The longitudinal resistance $R_{xx} = V_{xx}/I$ and the Hall resistance $R_{xy} = V_{xy}/I$. **b** A cartoon depicting edge states (blue and red curves) and localized states in the bulk (black lines), **c**, Landau levels as a function of distance from one edge to the other. The confining potential at the edges causes the LLs to rise up in energy. **d**, Density of states showing LL broadening from potential fluctuation in the bulk. Extended states are saturated about the center of LLs while localized states live in the tails. **e**, Hall conductance $\sigma_{xy} = \dfrac{\rho_{xy}}{\rho_{xx}^2 + \rho_{xy}^2}$ and longitudinal conductance $\sigma_{xx} = \dfrac{\rho_{xx}}{\rho_{xx}^2 + \rho_{xy}^2}$ as a function of filling factor.

Since the vector potential only depends on y, p_x is a constant and can be eliminated from the hamiltonian by using $\boldsymbol{A}(\boldsymbol{r}) = \boldsymbol{A}_L + (p_x/e, 0, 0)$ (I have used the fact that A is unique up to the addition of the gradient of an arbitrary derivable function). With the new vector potential, the Hamiltonian becomes $H = \frac{1}{m^*}\left((eBy)^2 + p_y^2\right)$. Defining the ladder operators $a = \frac{1}{\sqrt{2}}\left(\frac{y}{l_B} - i\frac{p}{p_0}\right)$ and $a^\dagger = \frac{1}{\sqrt{2}}\left(\frac{y}{l_B} + i\frac{p}{p_0}\right)$ where $l_B = \sqrt{\hbar/eB} = 26 \text{ nm}/\sqrt{B[\text{T}]}$ and $p_0 = \sqrt{\hbar eB}$, the Hamiltonian now reads

$$H = \hbar\omega_c\left(a^\dagger a + \frac{1}{2}\right), \tag{3.4}$$

where $\omega_c = eB/m^*$. Therefore, the eigen-energies of the system become quantized into levels called Landau levels (LLs) and their value is given by $E(B, n) = \hbar\omega_c(n + 1/2)$ where $n = 0, 1, \ldots$. It is worth noting that the energy of a Landau level for non-relativistic particles is linear in B, and there is no zero energy state. These two properties are the main difference between non-relativistic fermions and the massless Dirac fermions in MLG, which I will discuss in the next section.

One important question regarding each Landau level is its degeneracy, i.e. how many electrons a Landau level can hold. From the derivation, it is evident that the eigen-energy does not depend on momentum in the x-direction, p_x. Hence, the number of states will be proportional to the possible values of p_x as well as the spin and valley degrees of freedom. Since the wave function has to reside inside the sample, one can show from Eq. 3.3 that the value of p_x has to be between 0 and eBW, where W is the width of the sample. Using periodic boundary conditions, the value of p_x is an integer multiple of $p_x^0 = 2\pi\hbar/L$ where L is the length of the sample. This implies that the number of possible states for p_x per unit area is $n_B = B/(h/e)$. Hence, taking spin and valley degeneracies into account, each Landau level contains $g_v g_s n_B$ states. One often is interested in the number of filled

Landau levels. Therefore, it is useful to define the dimensionless quantity $\nu = n_e/n_B$ called the filling factor, where n_e is the electron density.

Bulk and Edge states

One assumption which is often made when one calculates Landau levels is that the sample size is infinite. However, a real sample has finite size and, therefore, the electrons are subjected to a confining potential at the edges which causes the energy of the Landau level to rise up (Fig. 3.1c). Therefore, when one considers conductance in the quantum Hall regime, the sample has to be divided into two regions, namely the edge and the bulk. In addition, states in a Landau level in the bulk are not completely degenerate owing to disorder which induces a spatially-varying potential. This causes the Landau level to broaden. Furthermore, electrons in the bulk whose energy is away from the center of a Landau level become localized. For example, if the Landau level is much less than half-filled, the occupied states will form islands across the sample with a gapped region in between (Fig. 3.1b). As a result, electrons on these islands cannot propagate from one end to the other and the bulk becomes insulating. As density is increased to near half-filled Landau level (the center of LLs), the islands grow larger and merge together to form a pathway for electrons to percolate through the sample. As a result, the bulk becomes conductive. This happens repeatedly as the density is tuned from one LL to another (Fig. 3.1d)

Along one edge, electrons will propagate in a skipping orbit fashion in the direction opposite to that from the edge from the other side (Fig. 3.1b). If the Fermi energy is such that the bulk is insulating, this will prevent electrons along the edge from back scattering because, in order to propagate backward, they would need to scatter to the opposite edge which has been prevented by the insulating bulk. Therefore, the longitudinal resistance

$R_{xx} = V_{xx}/I$ is zero because there is no drop in voltage (Fig. 3.1d and e, blue and magenta dots). If the Fermi energy is around the center of a Landau level (half filled LL), the bulk becomes conductive. Hence, it is possible for electrons, propagating along one edge, to back scatter as they can now travel to the opposite side through the conductive bulk. As a result, there is some voltage drop and R_{xx} becomes finite (Fig. 3.1c and d, green dot). The oscillations observed in R_{xx} at finite magnetic field are called Shubnikov-de Haas oscillations.

I now concentrate on the quantization of Hall resistance R_{xy}. When the Fermi energy is between two LLs (completely filled LL), the bulk is insulating and electrons propagating along the edges effectively travel in one dimension. Since backscattering is suppressed, electrons entering edge states from the left and the right will maintain their electrochemical potential at μ_L and μ_R respectively. Electrons moving in one dimensional channel will have a conductance equal to $g_v g_s N \frac{e^2}{h}$ where N is the number of modes which is equal to the number of LLs below the Fermi energy. Therefore, the net current from the left to the right contacts is given by

$$I = g_v g_s N \frac{e^2}{h} \frac{(\mu_L - \mu_R)}{e} = g_v g_s N \frac{e^2}{h} V_{xy} = \nu \frac{e^2}{h} V_{xy} \tag{3.5}$$

and the Hall conductance is $\sigma_{xy} = g_v g_s N \frac{e^2}{h} = \nu \frac{e^2}{h}$, when $R_{xx} = 0$.

The plateaus observed in Hall resistance or conductance require the presence of disorder. As density is increased away from a completely filled LL, injected electrons will enter the bulk and be localized somewhere in the bulk. Hence, they do not contribute to the transport measurement. As a result, the Hall conductance stays constant as density is tuned between fully occupied LLs and shows up as a plateau in quantum Hall regime. As density is increased further to reach the center of the LL where extended states lie,

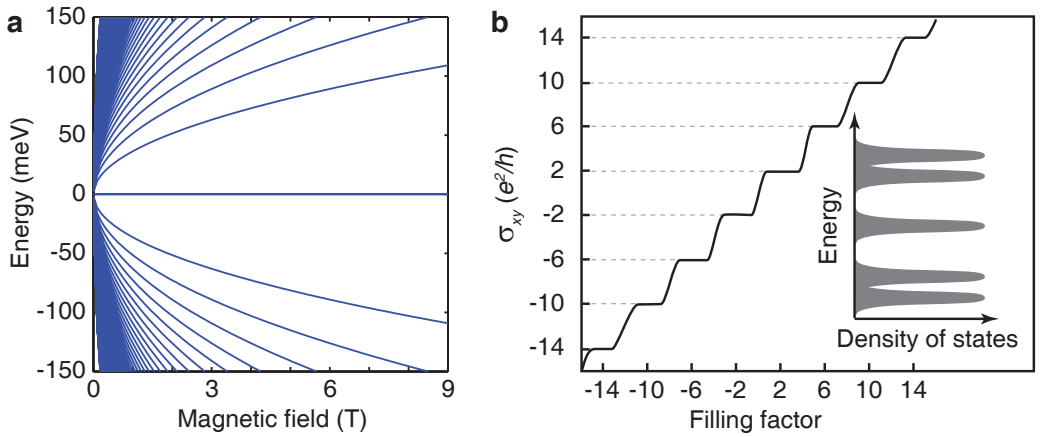

Figure 3.2: **a**, Landau levels in MLG as a function of magnetic field. **b**, Hall conductance in MLG as a function of filling factor. Inset: Density of states as a function of energy.

electrons in the bulk can now propagate across the sample and edge states can backscatter. The value of the Hall conductance thus varies to reach a new plateau.

3.2 Quantum Hall effect in monolayer graphene

Due to the chiral and massless nature of electrons in MLG, the QHE in MLG displays new features which do not exist for non-relativistic electrons in conventional 2DEGs. In this section, I will investigate these new features, namely the zero energy Landau level and half-integer QHE.

Landau levels in monolayer graphene

Using the Hamiltonian in Eq. 2.9, I again replace $\boldsymbol{p} \rightarrow \boldsymbol{p} + e\boldsymbol{A}(\boldsymbol{r})$ and the operator $\pi = p_x + \xi i p_y$ can be rewritten as $\pi = \sqrt{2\hbar eB}a$ for the K valley or $\pi = \sqrt{2\hbar eB}a^\dagger$ for the K' valley. The Hamiltonian at a finite magnetic field in the vicinity of the K point thus

reads

$$H^B_{\rm MLG} = v_{\rm F}[\boldsymbol{p} + e\boldsymbol{A}(\boldsymbol{r})] \cdot \boldsymbol{\sigma} = \sqrt{2}\frac{\hbar v_{\rm F}}{l_B}\begin{bmatrix} 0 & a \\ a^\dagger & 0 \end{bmatrix}. \tag{3.6}$$

The eigen-energy can be obtained by considering

$$(H^B_{\rm MLG})^2 = 2\left(\frac{\hbar v_{\rm F}}{l_B}\right)^2 \begin{bmatrix} a^\dagger a + 1 & 0 \\ 0 & a^\dagger a \end{bmatrix} \tag{3.7}$$

where I have used the identity $[a, a^\dagger] = 1$. Since $a^\dagger a$ is the number operator $\hat{n}$, $H^B_{\rm MLG}$ can be diagonalized by the eigenstates $\psi_n = [|n-1\rangle, \pm|n\rangle]^\dagger$ for $n \neq 0$ and $\psi_0 = [0, |0\rangle]^\dagger$ for $n = 0$ for the K valley. Similarly, the eigenstates for the K' valley are given by $\psi_n = [|n\rangle, \pm|n-1\rangle]^\dagger$ for $n \neq 0$ and $\psi_0 = [|0\rangle, 0]^\dagger$ for $n = 0$. As a result, the energy of the Landau levels for MLG is given by

$$E_{\rm MLG}(B, n) = \pm\frac{\hbar v_{\rm F}}{l_B}\sqrt{2n} = \pm v_{\rm F}\sqrt{\hbar e B}\sqrt{2n} \tag{3.8}$$

The differences between the Landau levels in MLG and non-relativistic particles are evident. First, the energy of the Landau levels in MLG is proportional to $\sqrt{B}$ and $\sqrt{n}$ instead of B and n. Second, the Landau levels in MLG have both positive and negative energies. Most importantly, there exists the zero-energy Landau level which results in a half-integer quantum Hall effect ($\sigma_{xy} = 4(n + 1/2)e^2/h$ where the factor of 4 comes from valley and spin degeneracies).

To understand how the zero-energy LL can produce the half-integer QHE, one needs to look at the behavior of the zero-energy LL from the K and K' valleys as it approaches the edge. Since spin degeneracy does not get affected by the edge, let me ignore it for the moment. For the armchair edge, the K and K' degeneracy is lifted near the edges as the energy of one valley disperses up while the other valley disperses down. As

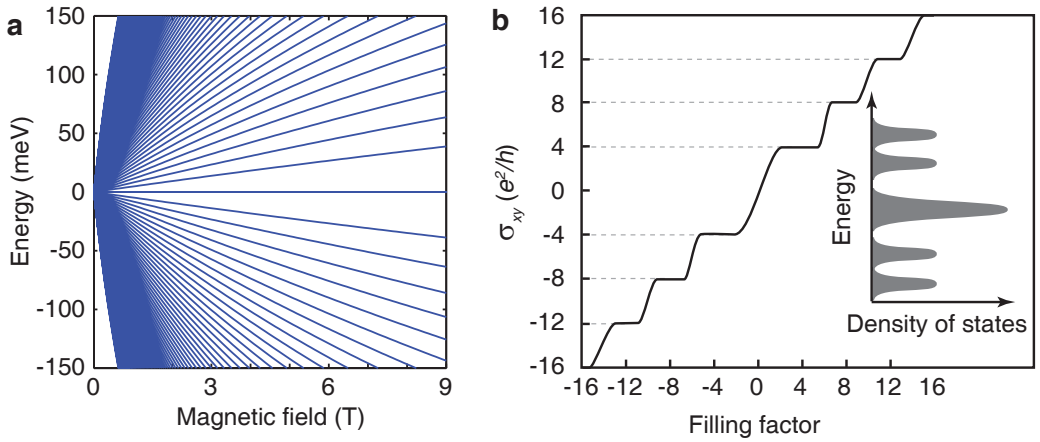

Figure 3.3: **a**, Landau levels in BLG as a function of magnetic field. **b**, Hall conductance in BLG as a function of filling factor for the case of $V = 0$. The 8-fold degenerate LL is evident at zero filling factor when the conductance plateaus change from $-4e^2/h$ to $4e^2/h$. Inset: Density of states as a function of energy.

a result, one ends up with odd number of modes. For the zigzag edge, the K valley morphs into dispersionless surface mode which does not contribute to the edge current. However, the K' valley mixes with the surface mode and give rise to two dispersing edge states, one up and one down in energy [68]. Hence, both armchair and zigzag edges result in the odd number of modes and once spin degeneracy is taken into account, the Hall conductance is $2(2n+1)e^2/h$ as observed experimentally.

3.3 Quantum Hall effect in bilayer graphene

For BLG, the low-energy effective hamiltonian in Eq. 2.15 is considered. I first neglect the effect of a potential difference between layers V. Similar to MLG, I replace π

by $\sqrt{2\hbar eB}a$ which results in the following Hamiltonian:

$$H^B_{\rm BLG} = \hbar\omega_c \begin{bmatrix} 0 & a^2 \\ (a^\dagger)^2 & 0 \end{bmatrix} \quad \rightarrow \quad (H^B_{\rm BLG})^2 = (\hbar\omega_c)^2 \begin{pmatrix} a^2(a^\dagger)^2 & 0 \\ 0 & (a^\dagger)^2 a^2 \end{pmatrix} \tag{3.9}$$

where $\omega_c = eB/m^*$. It can be shown that $a^2(a^\dagger)^2 = (\hat{n}+1)(\hat{n}+2)$ and $(a^\dagger)^2a^2 = (\hat{n}-1)\hat{n}$. Hence, the eigen-state is $\psi = [0, |0\rangle]^\dagger$ and $[0, |1\rangle]^\dagger$ for $n = 0, 1$ and $\psi = [|n-2\rangle, \pm|n\rangle]^\dagger$ for $n \geq 2$. The energy of a LL is

$$E_{\rm BLG}(B, n) = \pm\hbar\left(\frac{eB}{m^*}\right) = \pm\hbar\omega_c\sqrt{n(n-1)}. \tag{3.10}$$

Now, the energy of a LL depends linearly on B, the same as the non-relativistic case. In contrast, the energy depends on $\sqrt{n(n-1)}$ instead of $n + 1/2$ on the non-relativistic case. It is evident that both the zeroth and first LLs are degenerate and have zero energy. Therefore, the zero-energy LL in BLG has 8-fold degeneracy coming from spin, valley, and $n = 0$ and 1 while other LLs only have 4-fold degeneracy from spin and valley. Thus, the Hall conductance is given by $\sigma_{xy} = \pm Ne^2/h$ where $N = 4, 8, 12, \ldots$.

Now reintroducing a finite potential difference V, the 8-fold degeneracy for the zero energy LL is lifted. This electric field breaks inversion symmetry and the valley degeneracy is lifted. In fact, charge carriers for the K valley in the zero-energy LLs reside in the bottom layer while those for the K' valley reside in the top layer (see eigen-states for the zero-energy LLs). Hence, with an applied electric field, those charge carriers are subjected to different on-site potential causing the 8-fold LL to split into two 4-fold LLs.

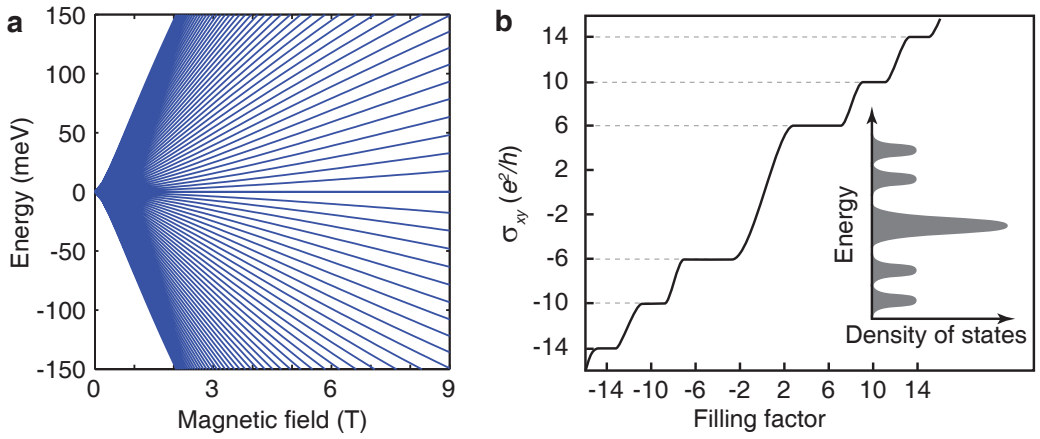

Figure 3.4: **a**, Landau levels in ABC trilayer graphene as a function of magnetic field. **b**, Hall conductance in ABC trilayer graphene as a function of filling factor. The 12-fold degeneracy of zero-energy LL is evident at zero filling factor when the conductance plateaus change from $-6e^2/h$ to $6e^2/h$. Inset: Density of states as a function of energy.

3.4 Quantum Hall effect in trilayer graphene

Quantum Hall effect in ABC trilayer graphene

I first concentrate on ABC trilayer graphene whose electronic properties are a natural extension of those in MLG and BLG. Since only the low-energy band is involved in electronic transport measurement, the low-energy Hamiltonian is considered:

$$H^B_{ABC} = \frac{v_F^3(2\hbar eB)^{3/2}}{\gamma_1^2}\begin{bmatrix} 0 & a^3 \\ (a^\dagger)^3 & 0 \end{bmatrix} \quad \rightarrow \quad (H^B_{ABC})^2 = \frac{v_F^6(2\hbar eB)^3}{\gamma_1^4}\begin{bmatrix} a^3(a^\dagger)^3 & 0 \\ 0 & (a^\dagger)^3a^3 \end{bmatrix} \tag{3.11}$$

Similar to both MLG and BLG cases, the diagonal entries of $(H^B_{ABC})^2$ can be rearranged as $a^3(a^\dagger)^3 = (\hat{n}+1)(\hat{n}+2)(\hat{n}+3)$ and $(a^\dagger)^3a^3 = (\hat{n}-2)(\hat{n}-1)\hat{n}$. The eigen-states of H^B_{ABC} are thus $\psi = [0, |n\rangle]^\dagger$ for $n = 0, 1, 2$ and $\psi = [|n-3\rangle, \pm|n\rangle]^\dagger$ for $n \geq 3$ and the

eigen-energies are

$$E_{ABC}(B,n) = \pm\frac{v_{\mathrm{F}}^3(2\hbar eB)^{3/2}}{\gamma_1^2}\sqrt{n(n-1)(n-2)} \tag{3.12}$$

The energy of a LL is therefore proportional to $B^{3/2}$ instead of $\sqrt{B}$ or B as in MLG and BLG respectively. And its dependence of LL index is $\sqrt{n(n-1)(n-2)}$ as opposed to $\sqrt{n}$ and $\sqrt{n(n-1)}$ for MLG and BLG. As a result, the zeroth, first, and second LLs all live at zero energy, resulting in 12-fold degeneracy while other LLs have 4-fold degeneracy. The first conductance plateau will be observed at $\pm 6e^2/h$ and then followed by $\pm 10e^2/h, \pm 14e^2/h, \ldots$. This sequence of plateaus is the same as MLG except the absence of $\pm 2e^2/h$ plateaus.

Quantum Hall effect in ABA trilayer graphene

As mentioned in section 2.3, the Hamiltonian of ABA trilayer graphene can be divided into MLG-like and BLG-like sectors. The interaction between these two sectors depends only on the potential difference between the first and the third layers ($\Delta_1 = (U_1 - U_3)/2$). If $\Delta_1 = 0$, these two sectors do not interact and the quantum Hall effect in ABA trilayer graphene will be the combination of those from MLG and BLG (Fig. 3.5). The small difference arises in the BLG-like sector as the value of γ_1 now becomes $\sqrt{2}\gamma_1$. As a result, the cyclotron gap in BLG-like sector of ABA trilayer graphene is smaller than that of BLG by a factor of $\sqrt{2}$.

At zero energy, there lies the zeroth LL from MLG-like subband and the zeroth and first LLs from BLG-like subband. Hence, the zero-energy LL in ABA trilayer graphene has the same 12-fold degeneracy as that in ABC trilayer graphene. However, the coexistence of these subbands leads to Landau level crossings which do not occur in ABC trilayer

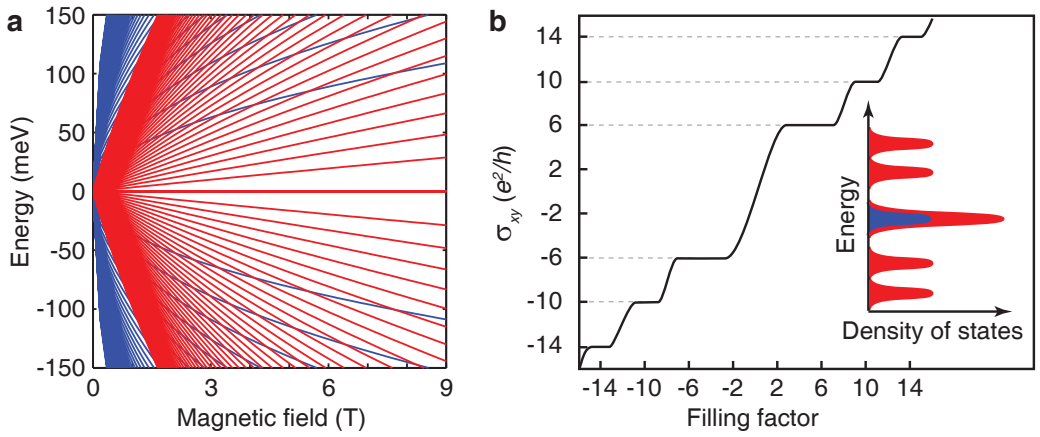

Figure 3.5: **a**, Landau levels from MLG-like subband (blue lines) and BLG-like subband (red lines) in ABA trilayer graphene as a function of magnetic field. Due to their different dependence on B, the LLs from these two subbands cross at finite B and density, resulting in 8-fold degenerate LL at the crossings. **b**, Hall conductance in ABA trilayer graphene as a function of filling factor. Inset: Density of states as a function of energy.

graphene. Since $E_{\mathrm{MLG}} \sim \sqrt{B}$ and $E_{\mathrm{BLG}} \sim B$, the LLs from these two subbands have to cross at some finite magnetic fields and filling factors (Fig. 3.5). At the crossing points, the degeneracy increases to 8-fold because each of the crossing LLs has 4-fold degeneracy.

Quantum Hall effect in TLG with full parameter model

So far, the energy of LLs is calculated within a simple model in which only γ_0 and γ_1 are taken into account. In this section, I will outline a numerical method used to calculate LLs for full-parameter model which is necessary to explain experimental data of QHE in ABA trilayer graphene (chapter 5).

To calculate LLs in the full-parameter model, one needs to start from 6-by-6 Hamiltonians in Eq. 2.24 and 2.25 for ABC and ABA trilayer graphene, respectively. I again replace π with $\sqrt{2\hbar eB}a$ for the K point and $\sqrt{2\hbar eB}a^{\dagger}$ for the K' point. The resulting Hamiltonians are too complicated to diagonalize analytically. Therefore, a numerical

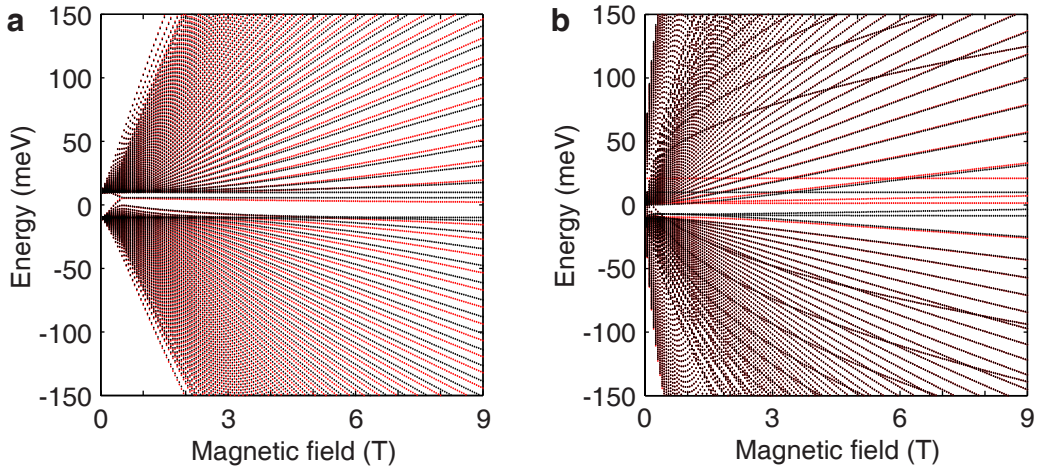

Figure 3.6: **a**, LLs of ABC trilayer graphene using full-parameter model with $\gamma_0 = 3.1$, $\gamma_1 = 0.39$, $\gamma_2 = -0.028$, $\gamma_3 = 0.315$, $\gamma_4 = 0.041$, and $U_1 = U_2 = U_3 = 0$ eV. **b**, LLs of ABA trilayer graphene using full-parameter model with $\gamma_0 = 3.1$, $\gamma_1 = 0.39$, $\gamma_2 = -0.028$, $\gamma_3 = 0.315$, $\gamma_4 = 0.041$, $\gamma_5 = 0.05$, $\delta = 0.046$ and $U_1 = U_2 = U_3 = 0$ eV [46]. The red and black lines in both **a** and **b** are spin-degenerate LLs for K and K' valleys.

calculation is needed. To diagonalize the hamiltonians numerically, I will work in the basis of $|n\rangle$ which satisfies the relations $a\,|n\rangle = \sqrt{n}\,|n-1\rangle$ and $a^\dagger\,|n\rangle = \sqrt{n+1}\,|n+1\rangle$. In the matrix form, a can be expressed as

$$a = \begin{bmatrix} 0 & \sqrt{1} & 0 & 0 & \cdots & 0 & \cdots \\ 0 & 0 & \sqrt{2} & 0 & \cdots & 0 & \cdots \\ 0 & 0 & 0 & \sqrt{3} & \cdots & 0 & \cdots \\ 0 & 0 & 0 & 0 & \ddots & \vdots & \cdots \\ \vdots & \vdots & \vdots & \vdots & \ddots & \sqrt{n} & \cdots \\ 0 & 0 & 0 & 0 & \cdots & 0 & \ddots \\ \vdots & \vdots & \vdots & \vdots & \vdots & \vdots & \ddots \end{bmatrix} \tag{3.13}$$

whose dimension is infinite. The matrix a needs to be truncated to a finite dimension for numerical calculation. For instance, if LLs between LL index ± 30 are needed, one might

want to truncate a to ∼100-by-100 dimension which would result in a Hamiltonian of 600-by-600 dimension to diagonalize. An unwanted consequence of truncating a is that it creates extra "parasitic" LLs at low energy. To eliminate these extra LLs, the eigenvectors have to be examined because some of the entries from these parasitic LLs are unusually large. This allows one to distinguish real LLs from the parasitic ones. Figures 3.6a and b show LLs calculated numerically using the full-parameter model for ABC and ABA trilayer graphene respectively. These higher order hopping parameters break valley degeneracy and the LLs from the K and K' valleys (Fig. 3.6 red and blue lines) are no longer degenerate. One thing which still remains the same for both simple and full-parameter models is that Landau level crossings exist only in ABA trilayer graphene. Therefore, this would allow for the use of quantum Hall measurement to distinguish between ABA and ABC trilayer graphene. In chapter 5, the effect of each parameter on the LLs will be discussed in detail. Also, the position of the crossings in B–ν space will be utilized to determine the SWMcC parameters.

3.5 Beyond single-particle picture

I thus far have discussed the quantum Hall effect within the single-particle framework and have ignored the effect of electron-electron interactions. However, several experiments have observed broken-symmetry states in MLG and BLG or even the fractional quantum Hall effect in MLG. In these broken-symmetry states, the valley and/or spin degeneracies are lifted by means of electron-electron interactions. They are generally observed in very clean devices because the energy scale of electron-electron interactions is very small, and as a result disorder could prevent one from observing these states. In ad-

dition, the strength of the interaction also depends on electron density and it is strongest in the vicinity of zero density due to reduced screening. Even though much effort has been put to investigating these interaction-driven states, their nature is still under debate, and further work is necessary.

Chapter 4

Electronic transport in dual-gated bilayer graphene at large displacement fields

Abstract

We study the electronic transport properties of dual-gated bilayer graphene devices. We focus on the regime of low temperatures and high displacement fields, where we observe a clear exponential dependence of the resistance as a function of displacement field and density, accompanied by a strong non-linear behavior in the transport characteristics. The effective transport gap is typically two orders of magnitude smaller than the optical band gaps reported by infrared spectroscopy studies. Detailed temperature dependence measurements shed light on the different transport mechanisms in different temperature regimes.

4.1 Introduction

The ability to electrostatically tune and deplete the charge density in two dimensional electron gases enables the fabrication of basic mesoscopic devices, such as quantum point contacts or quantum dots, which enhance our understanding of electronic transport in nanostructures [69]. Creating such electrically tunable nanostructures in monolayer graphene, a novel two-dimensional system [3], is far more challenging due to its gapless nature. In this respect, Bernal-stacked bilayer graphene (BLG) is an interesting material, because of the possibility of opening a band gap by breaking the symmetry between the top and bottom graphene sheets [70–72].

The low-energy band structure of free-standing BLG is gapless but in the presence of an on-site energy difference between the bottom and top layers a band gap develops. Different methods have been employed to induce a band gap including molecular doping, coupling to the substrate, and electric displacement field generated by gate electrodes [51, 52, 73–77]. However, the low-temperature ($\leq$ 100 K) transport characteristics of dual-gated BLG devices do not exhibit the strong suppression of conductance expected given the large band gaps (up to 250 meV) measured by infrared spectroscopy [52, 75–77]. In addition, only very weak non-linearities were found in the current versus source-drain voltage (I-V_{SD}) characteristics [52], in contrast with the strong non-linear behavior of typical semiconducting devices. A more complete study is needed to address the transport characteristics of gapped BLG devices as well as the role played by disorder.

In this chapter, we discuss the electronic transport properties of dual-gated (back-gated (BG) and top-gated (TG)) BLG devices. We focus on the regime of large transverse electric displacement fields, 0.8 V/nm $< |D| <$ 2.5 V/nm, over 3 times larger than in previ-

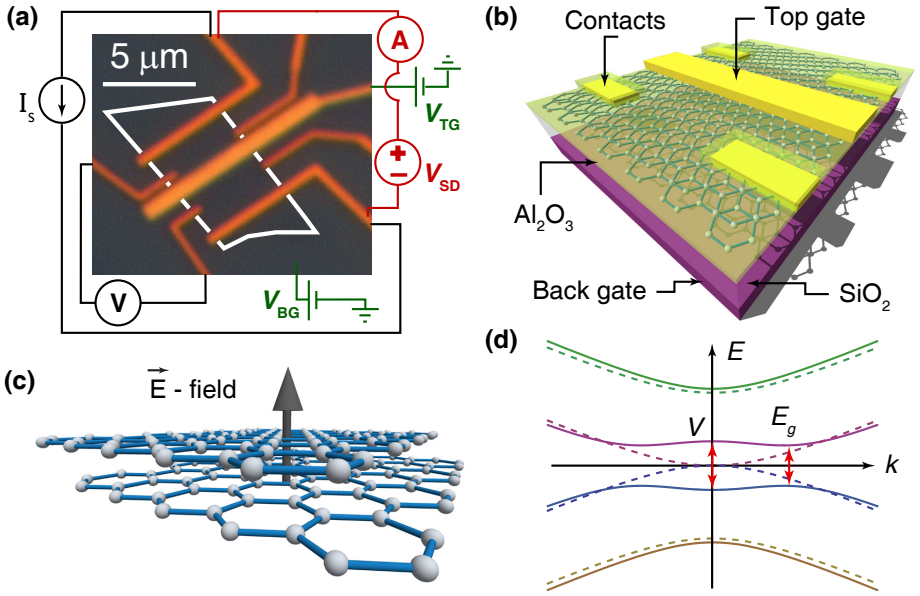

Figure 4.1: (a) Optical image of a BLG (outlined by white line). A, B, C, and D are contact electrodes and TG is a 1 μm-wide top gate electrode. The red and black diagrams are set-ups for two and four probe measurements respectively. (b) Schematic diagram of the measured device (not drawn to scale). (c) When BLG is subject to a transverse electric field, a potential difference is induced between top and bottom layers. (d) Band structure of free standing BLG (dashed lines) and band structure of BLG subject to transverse electric field (solid lines).

ous low-temperature experiments [52]. Upon the application of a large displacement field, we observe an exponential dependence of the device resistance on $|D|$ and density, which is accompanied by a strong non-linear behavior in the I-V_{SD} characteristics. However, the size of the effective transport gap is on the order of a few meV, two orders of magnitude smaller than the optical band gaps at the same D [76, 77], suggesting a strong role played by disorder. Temperature dependent measurements in the 300 mK to 100 K range show that the conductivity follows an activated behavior with three different activation energies, including a nearest neighbor hoping regime at the lower temperatures. However, it is the conduction mechanism at intermediate temperatures (2-70 K) which is responsible for most of the temperature variation of the conductivity of our devices, in which conductivity increases by several orders of magnitude.

4.2 Fabrication Process of Dual-gated Bilayer Graphene

We exfoliate Kish graphite onto 285 nm thick SiO_2 on top of degenerately doped silicon substrate. Bilayer graphene is identified by green value from RGB value of the optical microscope images. We calibrate green value of each graphene flake by subtracting off the green value of SiO_2 nearby the flake. After spinning poly(methyl methacrylate) (PMMA), we define contacts using electron beam lithography. After development, Cr/Au of 1/50 nm are deposited by thermal evaporator followed by standard lift-off in acetone. The chip is annealed at 350 °C in forming gas for 20 minutes to get rid of PMMA residue. We then deposit 3 nm of Al_2O_3 by E-beam evaporator as a seed layer [78]. Additional layer of 20 nm thick Al_2O_3 is deposited by atomic layer deposition at 250 °C. Top gates are defined as a last step with the same recipe as the contacts.

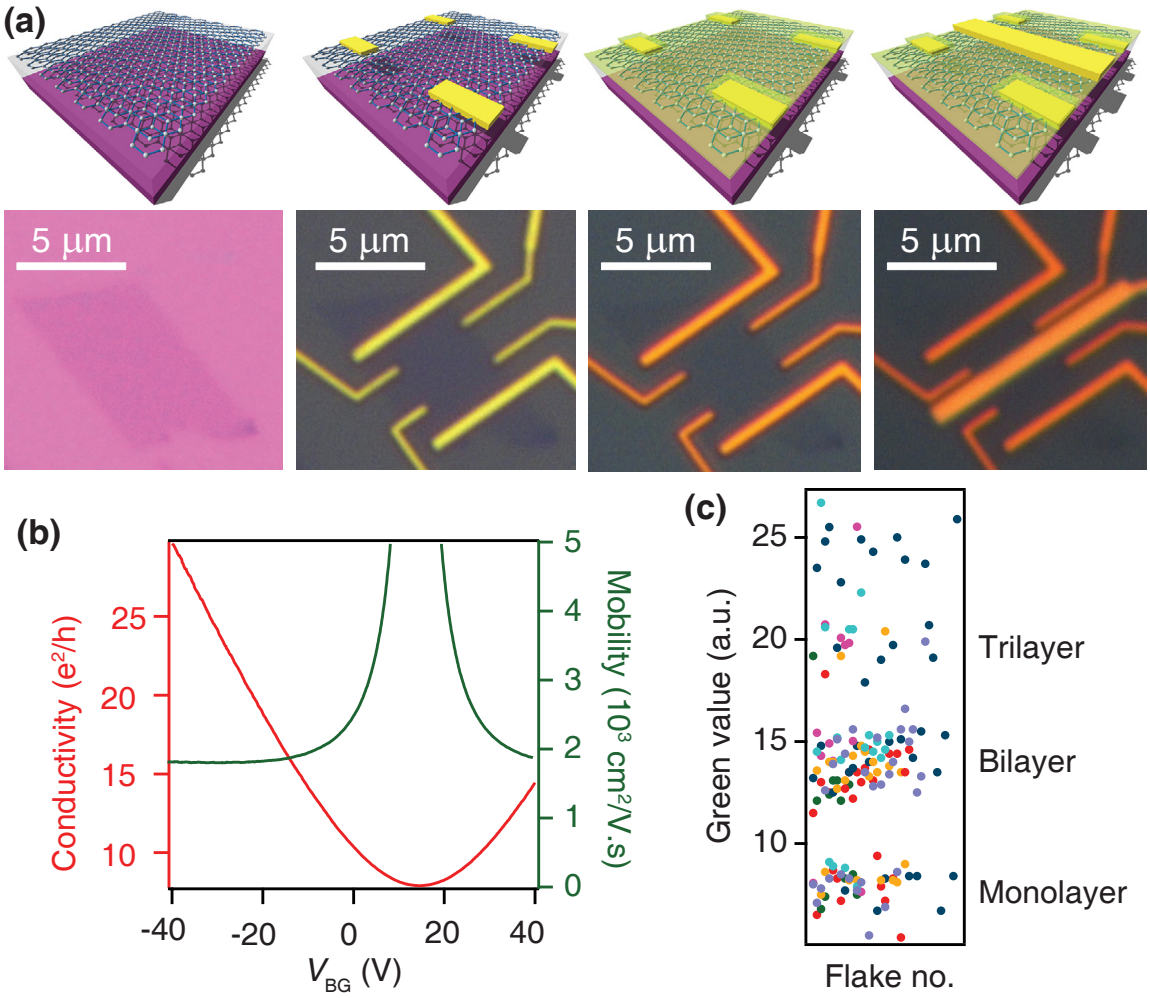

Figure 4.2: (a) Fabrication procedure of dual-gated bilayer graphene. (b) Conductivity and mobility as a function of back gate voltage of a 1 μm wide top gate. The mobility is calculated from the formula $\sigma = \mu en$. (c)The calibrated green value from different flakes obtained from the difference between the green value of SiO_2 and that of graphenes.

4.3 Device characteristics

Inferring from the slope of the charge neutrality point in the top-gated region, we find that a top gate capacitive coupling C_{TG} is ∼19.2 times larger than a back gate capacitive coupling C_{BG}. Using $\epsilon_{\mathrm{SiO_2}} = 3.9$ and $d_{\mathrm{TG}} = 23\,\mathrm{nm}$, we can calculate the dielectric constant of Al_2O_3 from $C_{\mathrm{TG}}/C_{\mathrm{BG}} = \frac{\epsilon_{\mathrm{Al_2O_3}}}{d_{\mathrm{TG}}}\frac{d_{\mathrm{BG}}}{\epsilon_{\mathrm{SiO_2}}} = 19.2$. With $d_{\mathrm{BG}} = 285\,\mathrm{nm}$, the effective dielectric constant of Al_2O_3 is $\epsilon_{\mathrm{Al_2O_3}} = 6$. This number we obtain is lower than a typical value of $\epsilon_{\mathrm{Al_2O_3}}$ (7-9). However, given the imperfection of the first 3 nm of our Al_2O_3 deposited by electron beam evaporation, such lower value is not surprising.

The typical mobility of our devices before oxide growth is between 1500 and 2000 $\mathrm{cm^2/V{\cdot}s}$. The mobility can degrade significantly after oxide deposition (by ∼30% in the device shown) which indicates that additional impurities have been introduced to the system during the oxide deposition. Charge and resonant impurities have been proposed to be dominant sources of scattering in graphene [19, 21, 79–81]. The impurities alter the potential profile experienced by the charge carriers and lead to the formation of electron and hole puddles [21, 56, 82]. They also induce tail states as well as localized states inside the band gap [83–86]. In addition, in BLG devices, charged impurities could lead to a spatial variation of the band gap. This suggests that adsorbates and/or charged impurities in the oxide may play a significant role in electronic transport in BLG.

4.4 Inducing a band gap with displacement field

We first focus on the transport properties at 300 mK. Fig. 4.3(a) shows the zero-bias resistance measured between electrodes A and B in Fig. 4.1(a). A parallel plate capacitor model yields a charge density under the top-gated region $n = C_{\mathrm{BG}}(V_{\mathrm{BG}} - V^D_{\mathrm{BG}}) +$

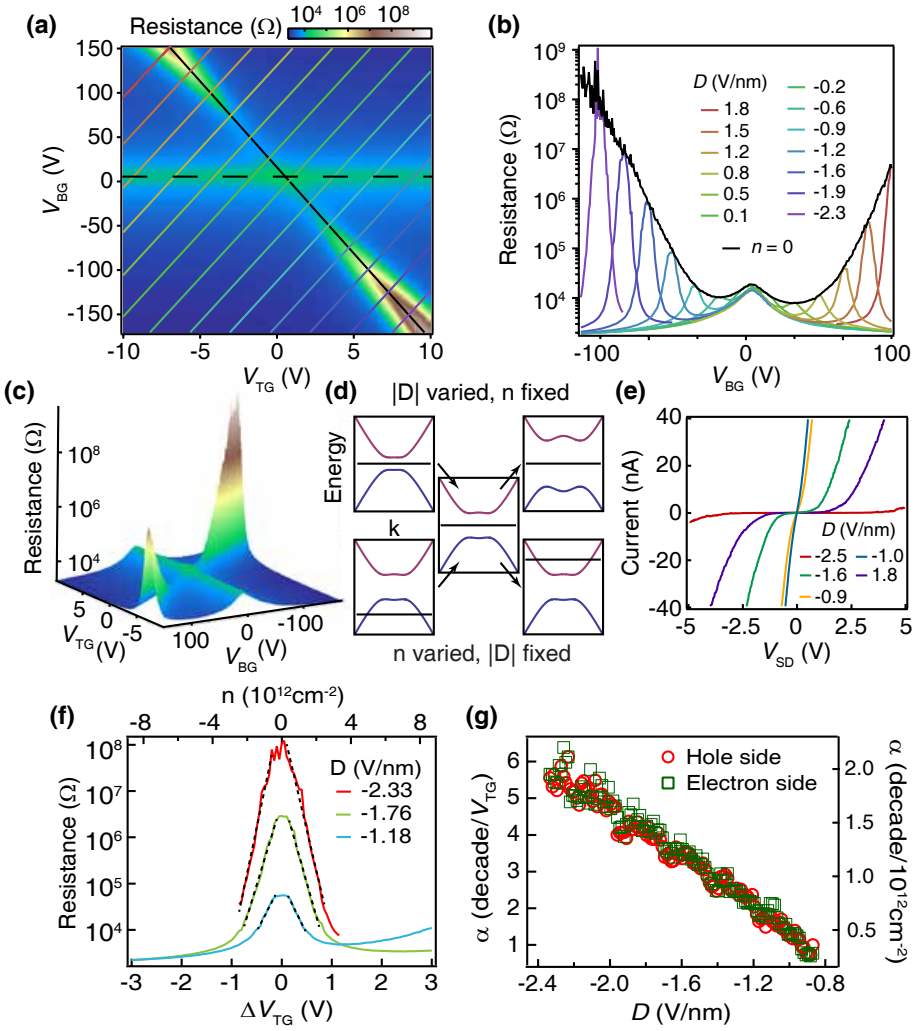

Figure 4.3: (a) Differential resistance at zero bias as a function of top and back gate voltages at $T = 300\,\mathrm{mK}$ (log scale). The black horizontal (dashed) and black diagonal (solid) lines correspond to zero charge densities in non top-gated and top-gated regions, respectively. (b) Cuts in (a) at different displacement fields D (colored lines) and at $n = 0$ (black line). Each cut corresponds to the lines in (a) with the same color. (c) 3D plot of (a). (d) Schematic band structure and E_F. As D is varied at fixed n, the size of the band gap changes while E_F remains fixed. We can also shift E_F and keep the band gap constant by varying n and keeping D the same. (e) I-V_SD characteristics at different values of D for $n = 0$ at $T = 300\,\mathrm{mK}$. (f) The resistance as a function of carrier density and offset top gate voltages at various D's. The black dashed lines are linear fits in log-scale. (g) The slope α of the linear fits in (f) as a function of D. The slope α decreases linearly with decreasing D.

$C_{\rm TG}(V_{\rm TG} - V^D_{\rm TG})$ where C is the capacitive coupling, V is the gate voltage, and $(V^D_{\rm BG}, V^D_{\rm TG})$ is the charge neutrality point (CNP) in the top-gated region. Following the convention from Zhang *et al* [76], we define the average electric displacement field $D = (D_{\rm BG} + D_{\rm TG})/2$.

4.4.1 Exponential dependence of resistance with displacement field

In this experiment, we concentrate on the case when $D_{\rm BG} = D_{\rm TG} = \epsilon_{\rm BG}(V_{\rm BG} - V^D_{\rm BG}/d_{\rm BG})$ where $\epsilon_{\rm BG} = 3.9$ is the relative dielectric constant of SiO_2 and $d_{\rm BG} = 285\,$nm. The sharp rise in resistance along the $n = 0$ [Fig. 4.3(b)] is characteristic of BLG [52, 75, 87].The maximum on-off ratio we can achieve in this device at 300 mK is on the order of 10^6, with a minimum resistance of $\sim 300\,\Omega$ [measured in a four probe geometry at $(V_{\rm BG}, V_{\rm TG}) = (-170, -10)\,$V]. We note that our high quality oxides enable us to apply a displacement field over 3 times larger than in previous low temperature experiments [52], resulting in an on-off ratio and insulating resistivity well over three orders of magnitude larger at 300 mK. Such insulating behavior makes BLG a good candidate for the fabrication of electrostatically designed mesoscopic devices.

The black diagonal curve in Fig. 4.3(a-b) shows a slice of the resistance for $n = 0$. Along this curve, we vary D in the range $[-2.5, +1.8]\,$V/nm, while keeping $E_{\rm F}$ in the top-gated region at the CNP [top path in Fig. 4.3(d)]. Beyond $|D| \sim 1\,$V/nm the resistance exhibits a clear exponential behavior with increasing $|D|$. Such resistance, if arising from a thermally activated behavior across a band gap, would be proportional to $\exp(E_g(D)/2k_BT)$ where $E_g(D)$ is the D-dependent band gap, k_B is Boltzmann's constant, and T is the temperature of the system. However, a fit to our data using the $E_g(D)$ obtained by infrared spectroscopy [76], yields an effective $T \approx 70\,$K, which is much higher than the 300 mK at which the measurement is performed. Hence, the conduction we observe

cannot be explained by activated behavior across such an optical band gap: disorder plays an important role, and the associated energy scale for transport is about two orders of magnitude smaller.

4.4.2 Non-linear I–V curve

This exponential increase in resistance is also accompanied by the development of strong non-linear transport characteristics. Figure 4.3(e) shows measurements of the DC current between A and B electrodes as a function of bias voltage and D, while keeping $n = 0$. We observe a clear non-linear behavior, which is consistent with the presence of an effective transport gap. However, the onset of non-linearity occurs on a scale of a few meV (2.2 meV for $|D| \sim 2.5\,\mathrm{V/nm}$), again about two orders of magnitude smaller than the optical band gap.

We now consider the behavior of the resistance versus gate voltage at various constant D [Fig. 4.3(b), colored lines]. By sweeping the gates along a constant D line, we effectively hold the size of the band gap fixed and shift the Fermi energy E_F from the valence band to the conduction band [bottom path in Fig. 4.3(d)]. We observe an exponential decrease in resistance as we sweep the gate voltages away from the CNP ($n = 0$), followed by a slower decrease, which we associate with E_F reaching the valence and conduction band mobility edges. The decrease appears symmetric on both the electron and hole sides, and depends on D. Figure 4.3(f) shows a few traces in detail, together with the fitted straight lines in the exponential regions, and Fig. 4.3(g) shows the slope α of these lines as a function of D, which exhibitis an approximately linear behavior.

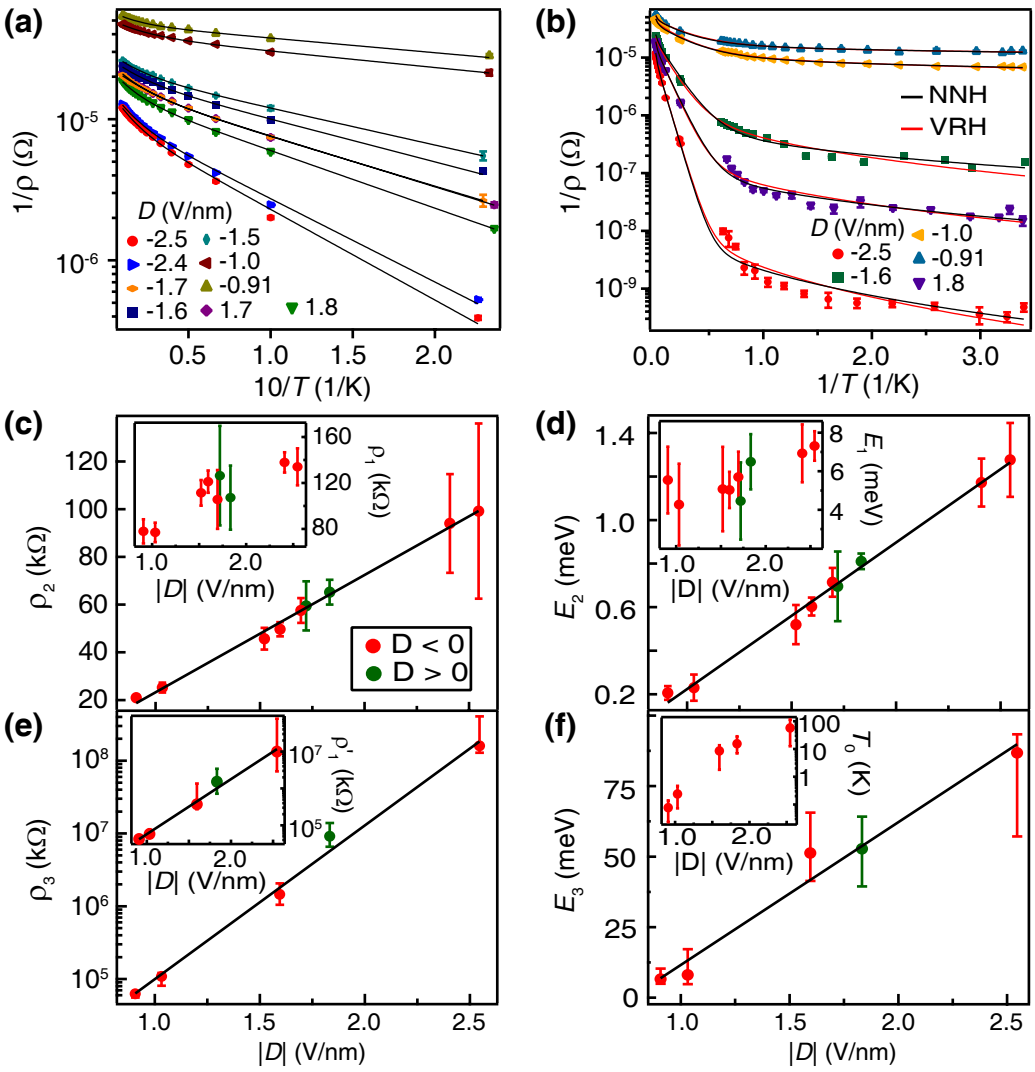

Figure 4.4: (a) Conductivity as a function of inverse temperature from 4.2 - 100 K. (b) Conductivity as a function of inverse temperature from 300 mK to 100 K. The black and red curves are the fits to the equation 4.2 with NNH and VRH terms respectively. (c)-(f) The extracted parameters from the fits plotted as a function of $|D|$.

4.5 Temperature dependence of the conductivity

To gain further insight into the transport properties, we study the temperature dependence of the conductivity in the 300 mK to 100 K range at different D's, and at $n = 0$. Figure 4.4(a) shows the conductivity measured using a four probe geometry in the temperature range 4-100 K for nine different values of D, while Fig. 4.4(b) shows the conductivity over the entire temperature range for five different values of D. In contrast to previous low temperature experiments at low D-fields [52], we observe two distinct temperature regimes, which become more pronounced at high D: a two-component fast decrease of the conductivity from 100 to 2 K, followed by a relatively weak T-dependence from 2 K to 300 mK, which we associate with thermally activated hopping (see below).

4.5.1 Activated behavior at intermediate temperature

At intermediate to high temperatures, we find that the conductivity is well described by an activated behavior with two different activation energies,

$$\frac{1}{\rho} = \sum_{i=1}^{2} \frac{1}{\rho_i} \exp(E_i/k_B T) \tag{4.1}$$

where ρ and E are resistivity and activation energy respectively [black lines in Fig. 4.4(a)]. The extracted fit parameters (ρ_1, ρ_2, E_1, and E_2) are plotted in Fig. 4.4(c-d). The higher energy scale, E_1, may be related to thermal activation across the optical band gap [75]. However, due to the very limited high-T range (70-100K), our data barely probe the onset of this exponential increase, and the values of E_1 obtained are very likely underestimated. The intermediate energy scale, E_2, exhibits a linear dependence on D, and is therefore approximately proportional to the band gap [76]. However, its value is two orders of magnitude smaller than the observed optical band gap at the same $|D|$ [76]. Still, it is the

conduction mechanism in this intermediate T-regime that is responsible for most of the measured variation in conductivity of the devices.

The overall behavior of the conductivity with T is reminiscent of that observed in disordered semiconductors [88], where transport via impurity bands and thermally activated hopping dominate transport at low temperatures. However, BLG devices are unique, in that their band gap can be continuously tuned by electrostatic means, and also because its two-dimensionality means that all disorder effects are surface rather than bulk effects. Compressibility measurements [89, 90] have shown that a very large density of states exists in gapped BLG on SiO_2, even in moderate D fields. Most of these states, however, are localized and do not contribute to transport, and in general the relationship between density of states and conductivity is more complex in the insulating regime.

To explain the origin and some of the qualitative features of the conductivity at intermediate T, we consider a model of an impurity band arising from the interaction of negatively charged donors [91]. Such model has been used to explain the observed conduction in the intermediate temperature regime in germanium semiconductors [92, 93]. Disorder can lead to the formation of an impurity band in which charge carriers are localized and a hopping mechanism dominates the conduction as we will show below. At low temperature, the majority of these localized states are empty or singly occupied. However, some of the states can become doubly occupied which leads to an extra band at higher energy due to the Coulomb interaction. Carriers in this band are weakly localized and hence possess a higher mobility. We can estimate the localization length of these states by equating E_2 with a charging energy $e^2/\epsilon r$ where $\epsilon \sim 5$ is the average dielectric constant of our top and bottom oxides, and r is the localization length. This estimate yields a localization length on the order of 100 nm (at $|D| = 2.5\,\mathrm{V/nm}$) to 1 μm at ($|D| = 0.9\,\mathrm{V/nm}$), comparable

with the width of the top gate. Such large localization length supports that the states are weakly bound. While this model accounts for some of the features present in the data, a rigorous theoretical model which takes into account the geometry and particularities of disorder in BLG, beyond the scope of this paper, is needed for a direct comparison and understanding of the complex relationship between transport and density of states, specially in the non-linear regime. In addition, compressibility measurements at larger D and lower temperatures [89, 90] may have enough resolution to observe the effects of disorder at these energy scales.

4.5.2 Hopping conduction at low temperature

The conductivity between 2 K and 300 mK decreases weakly with temperature, which indicates that we enter a hopping conduction regime through strongly localized states [88]. We perform a fit to the conductivity for the complete temperature range and all D with

$$\frac{1}{\rho} = \frac{1}{\rho_1 \exp(\frac{E_1}{k_B T})} + \frac{1}{\rho_2 \exp(\frac{E_2}{k_B T})} + \frac{1}{\Xi}, \tag{4.2}$$

where $\Xi = \rho_3 \exp(E_3/k_B T)$ for nearest neighbor hopping (NNH) or $\rho_3' \exp(T_0/T)^{1/3}$ for variable range hopping (VRH) [88]. Both the NNH and VRH fits agree reasonably well with the data [Fig. 4.4(b)]. VRH has been proposed to be the transport mechanism for gapped BLG at intermediate and low T [52]. However our measurements yield a value of ρ_3' that grows exponentially with $|D|$ [Fig. 4.4(e) inset]. Such strong dependence is unexpected because, in VRH, the factor $\exp(T_0/T)^{1/3}$ already includes the strong exponential contributions from both hopping between sites and differences in energy levels [88]. Hence, we propose that the transport mechanism in our BLG devices is NNH in the temperature and D regime explored.

For NNH, $\rho_3 = \rho_3^0 \exp(2r/a)$ where r is the distance between hopping sites and a is the localization length [88]. The magnitude of r can be approximated from the density of impurities, n_i, by $r = n_i^{-1/2}$. The CNP in this device is located at $(V_{\mathrm{BG}}^D, V_{\mathrm{TG}}^D) \approx (16, 0)\,\mathrm{V}$, which corresponds to $n_i \approx 10^{12}\,\mathrm{cm}^{-2}$ and $r \approx 10\,\mathrm{nm}$. The linear fit from Fig. 4.4(e) yields a localization length $a \approx 4/[D(\mathrm{V/nm})]\,\mathrm{nm}$. This allows us to estimate the crossover temperature T^{VRH} at which the conduction mechanism changes from NNH at high T to VRH at low T. As the temperature is lowered, it is feasible for electrons to hop to further sites but closer in energy due to the reduced coulomb interaction. This transition takes place when $2r/a$ and E_3/k_BT are comparable [88], which yields $T^{\mathrm{VRH}} \lesssim 80\,\mathrm{mK}$ for $|D| < 2.5\,\mathrm{V/nm}$. This crossover temperature is almost 4 times smaller than the lowest T we have studied (300 mK) which supports that NNH dominates the conduction.

In addition, the hopping activation energy E_3 decreases with decreasing $|D|$ [Fig. 4.4(f)]. This is an indication of the BLG making a transition from a strong to a weakly insulating state. As the band gap gets smaller, the electron-hole puddles start to merge and hence create a channel for carriers to percolate from one electrode to the other [94]. Extrapolating the fit to $E_3 = 0$, we obtain a value for the displacement field corresponding to this transition of $|D| = 0.7\,\mathrm{V/nm}$ corresponding to $E_g/2 \approx 35\,\mathrm{meV}$ which is consistent with BLG E_{F} fluctuations for an impurity density $n_i \approx 10^{12}\,\mathrm{cm}^{-2}$.

Chapter 5

Quantum Hall effect and Landau level crossing of Dirac fermions in trilayer graphene

Abstract

The physics of Dirac fermions in condensed matter systems has received extraordinary attention following the discoveries of two new types of quantum Hall effect in monolayer (MLG) and bilayer graphene (BLG) [4,5,95]. The electronic structure of trilayer graphene (TLG) has been predicted to consist of both massless MLG-like and massive BLG-like Dirac subbands [96–99], which should result in novel types of mesoscopic and quantum Hall phenomena. However, the low mobility exhibited by TLG devices on conventional substrates has led to few experimental studies [87, 100]. Here we investigate electronic transport in high mobility (>100,000 $cm^2/V{\cdot}s$) trilayer graphene devices on hexagonal boron nitride, which enables the observation of Shubnikov-de Haas oscillations and an

unconventional quantum Hall effect. The massless and massive characters of the TLG subbands lead to a set of Landau level crossings, whose magnetic field and filling factor coordinates enable the direct determination of the Slonczewski-Weiss-McClure (SWMcC) parameters [58] used to describe the peculiar electronic structure of TLG. Moreover, at high magnetic fields, the degenerate crossing points split into manifolds indicating the existence of broken-symmetry quantum Hall states.

5.1 Introduction

Bernal or ABA stacked TLG (Fig. 5.1b) is an intriguing material to study Dirac physics and quantum Hall effect (QHE) because of its unique band structure which, in the simplest approximation, consists of massless MLG-like and massive BLG-like subbands at low energy (Fig. 5.1c) [96–99]. The energies of the Landau levels (LLs) for massless charge carriers depend on the square root of the magnetic field $\sqrt{B}$ [4,5,101,102] while for massive charge carriers they depend linearly on B [54, 95, 101]. Therefore, the LLs from these two different subbands in TLG should cross at some finite fields, resulting in accidental LL degeneracies at the crossing points. However, one of the major challenges so far to observe QHE in TLG has been its low mobility on SiO_2 substrates [87, 100]. To overcome this problem, we use high quality hexagonal boron nitride (hBN) single crystals [103] as local substrates, which have been shown to reduce carrier scattering in graphene devices [40]. Substrate supported devices also allows us to reach higher carrier density than suspended samples [104], which is necessary for the observation of the LL crossings.

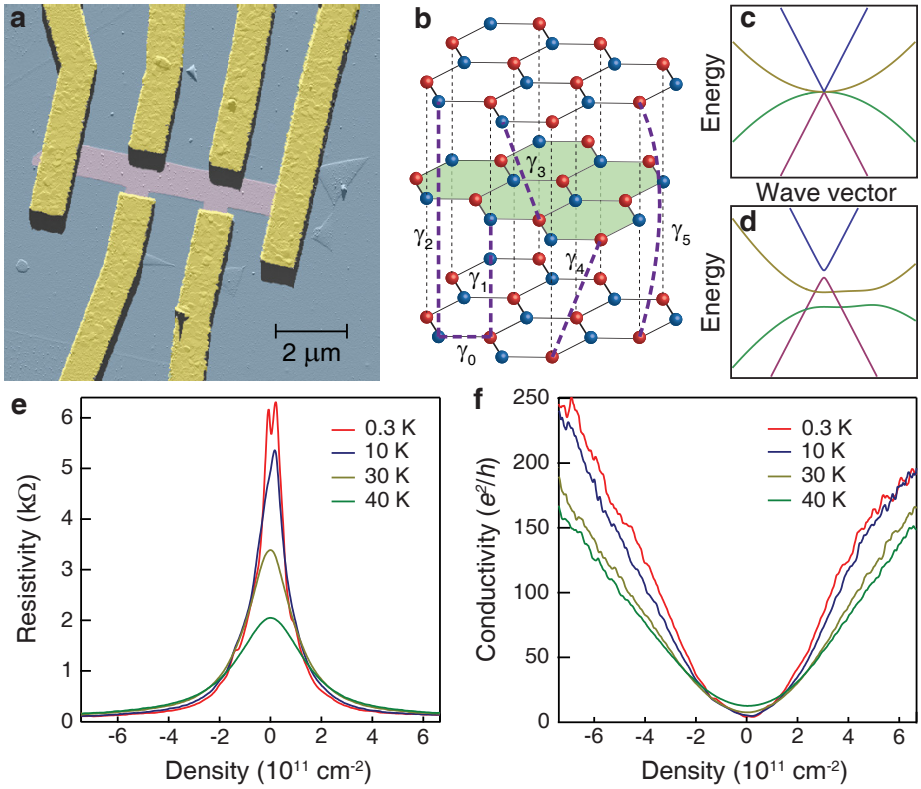

Figure 5.1: **Electronic properties of Bernal stacked TLG at zero magnetic field. a,** False color atomic force microscopy image of a TLG Hall bar device on hBN. **b,** Bernal stacked TLG atomic lattice. The SWMcC hopping parameters, γ_i, are shown by purple dashed lines connecting the corresponding hopping sites. In addition to γ_i, the SWMcC parameters also include the on-site energy difference, δ, between A and B sublattices (blue and red lattices). **c,** Band structure of TLG at low energy, which takes into account only the nearest neighbour intra- and inter-layer hopping parameters γ_0 and γ_1. **d,** Band structure of TLG within a full parameter model, with the parameters calculated from the SdH oscillations in Fig. 5.6b. **e,** Resistivity as a function of density and temperature for TLG. The double peak structure starts to emerge as temperature decreases below 10 K. **f,** Conductivity as a function of density and temperature.The field-effect mobility at 300 mK reaches ∼110,000 cm^2/V·s and decreases to ∼65,000 cm^2/V·s at 40 K

5.2 Fabrication process of graphene on hBN

Figure 1a shows an atomic force microscope image of a Hall bar shaped TLG device on hBN. In summary, Our fabrication process consists of mechanically exfoliating hBN and graphene flakes on different supports, and a flip chip bonding step to align them on top of each other. The graphene flakes are then patterned into a Hall bar geometry and contacted by electron beam lithography. The device is then annealed in forming gas to remove residue and cooled down in a He-3 cryostat.

For a detailed process, We first spin polyvinyl alcohol (PVA) on an oxidized silicon substrate at 3000 rpm for 60 s and bake the chip at 75 °C for 4 minutes. We then spin Poly(methyl methacrylate) (PMMA) 950 A5 on top of PVA at 1500 rpm for 60 s and heat it at 75 °C for 10 minutes (Fig. 5.2a). Graphene is deposited on to the polymer stack by mechanical exfoliation (Fig. 5.2b and c). After exfoliation, the polymer stack is peeled off from the substrate and a graphene flake is identified using an optical microscope (Fig. 5.2d).

After we find the flake we want to transfer, we lay a washer atop the polymer film on the side opposite to the graphene flake. The washer acts as a support frame for the polymer film and is backed by a piece of tape to keep it in place (Fig. 5.2e and f). Since the washer is in between the polymer film and the tape, it prevents the polymer film from sticking to the tape. We then cut the tape into a small piece around the washer for transferring.

Similar to graphene, we prepare a thin sheet of hexagonal Boron Nitride (hBN) by mechanical exfoliation onto an oxidized silicon substrate (Fig. 5.3a). A potential hBN flake is identified by optical microscopy and we subsequently perform atomic force microscopy (AFM) to determine its roughness and thickness. We typically choose flakes with thickness

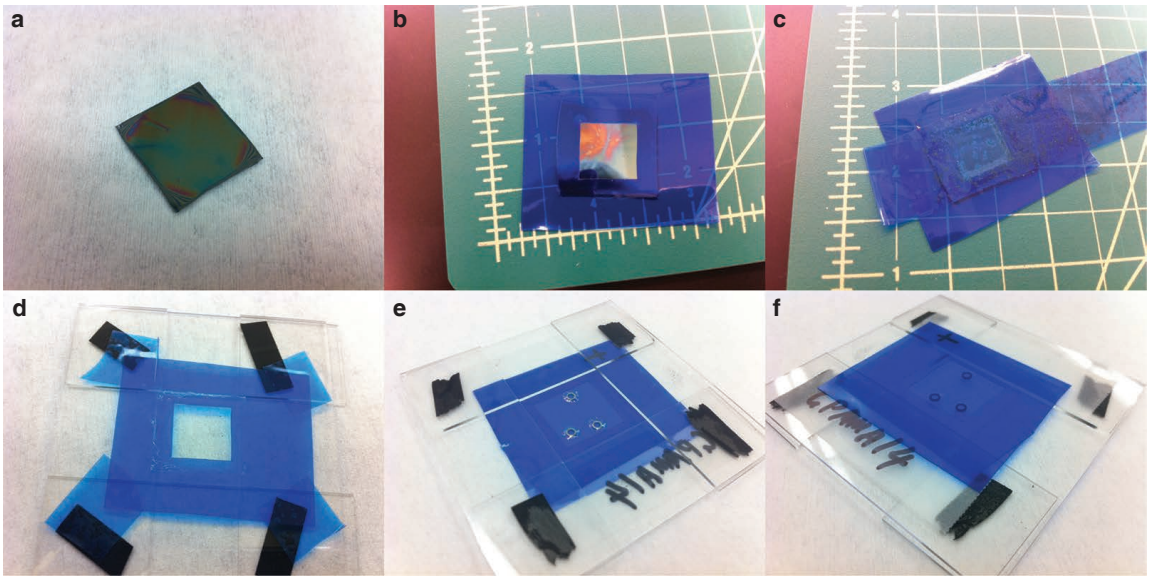

Figure 5.2: **Graphene transfer. a,** An oxidized silicon substrate covered by PVA and PMMA. **b,** The substrate is held in place by an acetone-soluble blue tape. This blue tape will later be used to peel off PVA and PMMA from the substrate. **c,** Graphene is mechanically exfoliated onto the polymer stack. **d,** The polymer stack (PVA and PMMA) with graphene on top is peeled off from the substrate. **e,** After identifying graphene, we put a washer around it and finally cover it by another tape. This allows us to use more than one piece of graphene per one preparation as opposed to a wet process in which only one graphene can be used. **f,** The back side of **e** showing another piece of tape used to cover the washers.

less than 30 nm and without atomic steps/terraces. hBN flakes of such thickness appear blueish under an optical microscope.

Once a graphene flake on a suspended polymer film and a hBN flake on SiO_2 are ready, we use a flip chip bonder to align the graphene flake to the hBN flake. Upon transferring, we heat up the substrate to 120 °C. We then press the polymer film onto the substrate for 5 minutes while keeping the temperature at 120 °C.

After the transfer process, often some areas of the graphene flake will have bubbles and/or ripples with smaller areas laying flat on hBN (Fig. 5.3b). To remove non-flat regions,

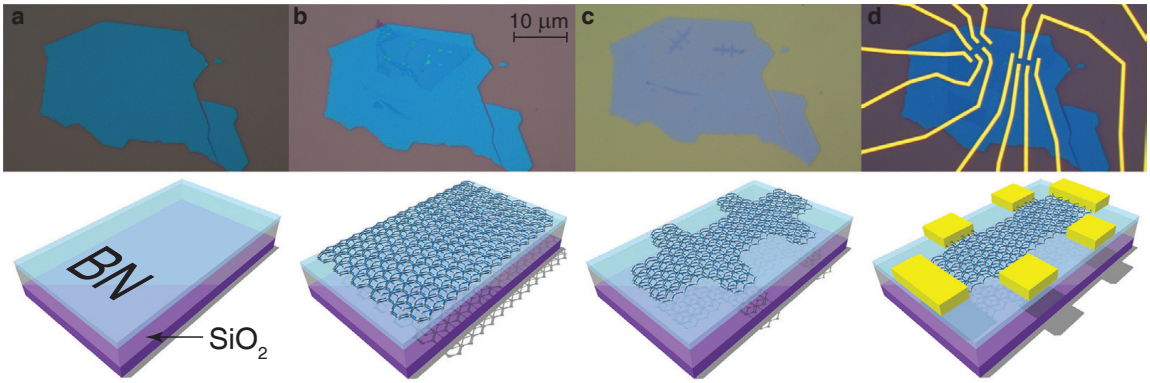

Figure 5.3: **Device fabrication. a,** Hexagonal boron nitride is exfoliated onto an oxidized silicon substrate. **b,** A piece of graphene is transferred onto hBN. Ripples and bubbles, forming after the transfer process, can be seen in the optical image. **c,** Graphene is etched by oxygen plasma into hall bar geometry to avoid the ripples and bubbles. **d,** Contacts are defined by electron beam lithography and Cr and Au are deposited by thermal evaporation.

we use PMMA as an etch mask and pattern a Hall bar geometry by standard electron beam lithography. Oxygen plasma etching is then used to etch uncovered graphene (Fig. 5.3c). After dissolving PMMA in acetone, we heat anneal the sample in forming gas (300 sccm of Ar and 700 sccm of H_2) to get rid of PMMA residue. The sample is heated up from room temperature to 350 °C for 1 hour and then held 350 °C for 2 more hours. After 2 hours, we turn off the heater and let the sample cool down slowly to room temperature. Contacts are then defined using electron beam lithography. We thermally evaporate 0.7 nm of Cr and 80 nm of Au, and lift off metals in acetone (Fig. 5.3d). We do a final heat annealing before cooling down the sample using the same recipe as above.

5.3 Current annealing

After cooling down, we perform current annealing to further improve the quality of the sample (Fig. 5.5) [105]. The procedure we use for current annealing is the following:

- Ramp source-drain bias V_{SD} slowly from 0 to a set voltage V_{set}, while monitoring an I–V_{SD} curve (the ramping time is on the order of a few minutes) (Fig. 5.4b).
- Once the set voltage is reached, monitor I as a function of time. The current I can, at first, increase or decrease but it will eventually get saturated (Fig. 5.4c). The magnitude of the change of the current has no clear relation with the quality of the Dirac peak after this current annealing. It is worth noting that, at the saturation, the current will change in a step-like fashion with the size of the step similar to the noise level in our system (Fig. 5.4d). This often indicates that there will be some changes in the Dirac peak.
- Ramp V_{SD} back to zero and check the Dirac peak (Fig. 5.4a).
- If the quality of the Dirac peak is not satisfying, We increase V_{set} by 0.5–1 V and repeat the procedure again.

It is useful to plot Dirac peaks after each current annealing on the same plot in order to compare them (Fig. 5.4a). We tend to be less aggressive at high bias ($V_{SD} > 10$ V) because a device could die at any moment. The maximum current at which graphene still survives is usually about 1 mA/micron/layer. One thing to keep in mind is that contact resistance could be much higher. Therefore, if it is a two-probe device, using high current density might not be an option as high contact resistance could effect the quality of transport data. For a 4-terminal device, we once found that current annealing between outer terminals alone did not improve the quality of the device but, with current annealing with both outer and inner pairs, the device produced much better data.

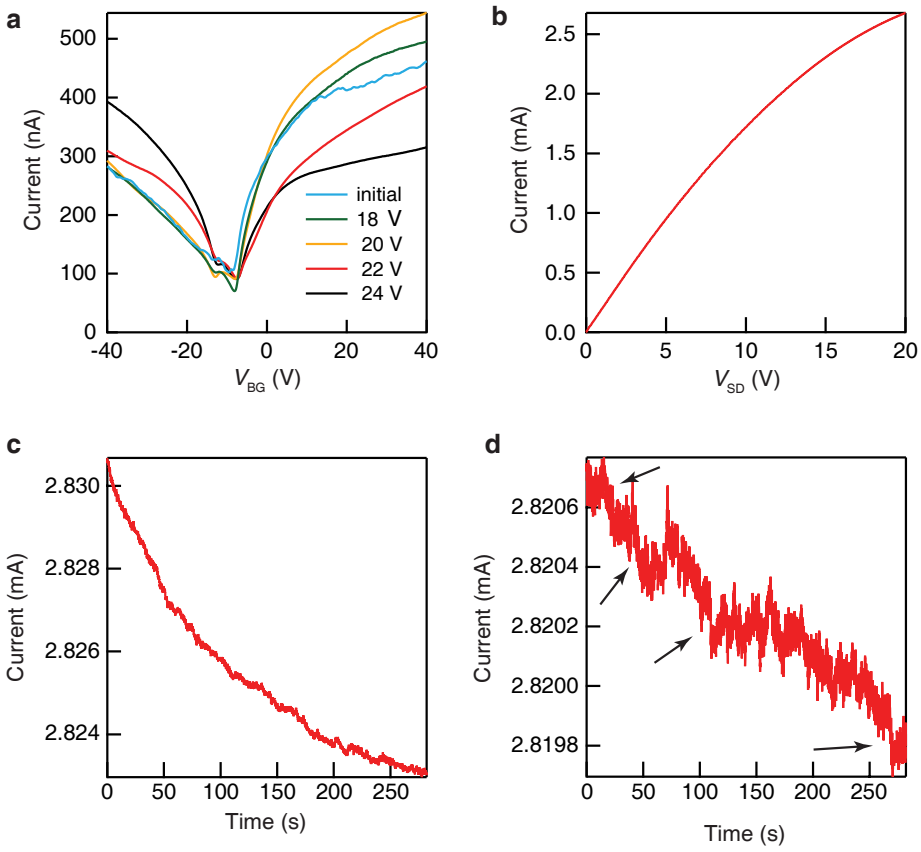

Figure 5.4: **Current annealing procedure. a**, Two-terminal measurement of current as a function of back gate voltage using 1 mV DC-bias. Each curve is measured right after the sample is subjected to an extremely high bias indicated in the inset for current annealing. **b**, A typical current–voltage characteristic of graphene when subjected to very high bias. The curve displays a sub-linear behavior. The sample's width is $\sim$1 μm. **c**, Current as a function of time at $V_{\mathrm{SD}} = 20$ V. The current decreases significantly at first and starts to saturate at the end. **d**, Current as a function of time after the current starts to saturate in **c**. The plot shows step-like changes (see arrows). This typically indicates that some changes are happening in the sample.

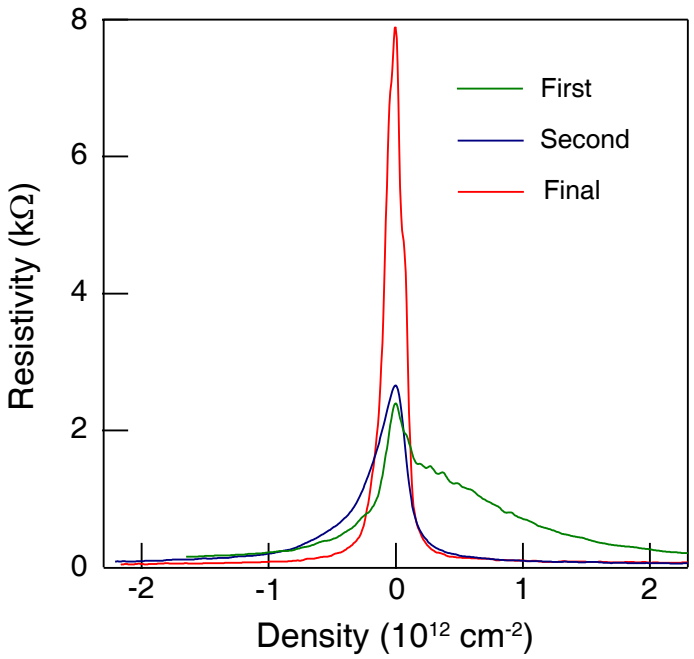

Figure 5.5: **Dirac peaks after current annealing.** Resistivity as a function of density after the first (green), second (blue), and final (red) current annealing steps. The Dirac peak becomes symmetric after the final current annealing step.

5.4 Device characteristic at zero magnetic field

Figures 1e and 1f show the resistivity and conductivity of a TLG device at zero magnetic field after current annealing. The resistivity at the Dirac peak exhibits a strong temperature dependence, which in MLG is a strong indication of high device quality [22, 106]. In addition, we also observe a double-peak structure at low temperatures (Fig. 5.1e). This double-peak structure is likely due to the band overlap which occurs in TLG when all SWMcC parameters are included in the tight-binding calculation of its band structure, as we show below. The field effect mobility of this device reaches $110,000\ \mathrm{cm}^2/\mathrm{V{\cdot}s}$ at 300 mK at densities as high as $6\times10^{11}\ \mathrm{cm}^{-2}$. This mobility value is two orders of magnitude higher than previously reported values for supported TLG [87,100] and comparable to suspended MLG-TLG samples [104,106].

5.5 Quantum Hall effect and Landau level crossings

The low disorder and high mobility enable us to probe LL crossings of Dirac fermions through the measurement of Shubnikov-de Hass (SdH) oscillations. Figure 2a shows longitudinal resistivity ρ_{xx} as a function of $1/B$, for a carrier density $n = -4.4\times10^{12}\,\mathrm{cm}^{-2}$. A pattern of SdH oscillations is clearly visible, albeit with different visibility and features depending on the B range. At low B (below $\sim$ 1 T), there are a number of oscillations characterized by broad minima separated by relatively narrower maxima. Beyond $\sim$ 1 T, the minima become sets of narrower oscillations, and a clear pattern emerges: each minimum in the oscillations indicates a completely filled LL with corresponding filling factor $\nu = hn/eB$, where h is Planck's constant, and e is the electron charge. Within a single particle picture, each LL is 4-fold degenerate, the degeneracy originating from the

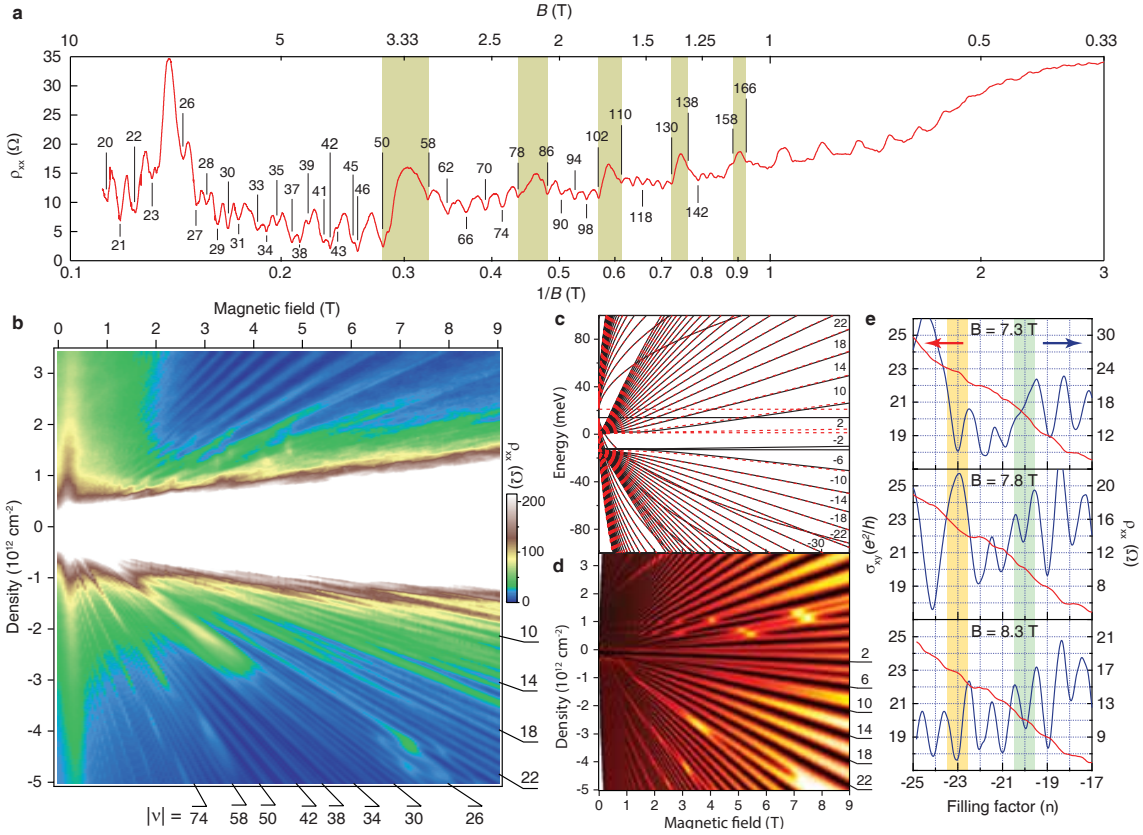

Figure 5.6: **SdH oscillations and Landau fan diagram in TLG. a,** ρ_{xx} as a function of inverse magnetic field at 300 mK. The numbers inside the figure indicate the filling factors at the SdH oscillation minima. The highlighted bands show the regions of 8-fold degeneracy, which provide evidence for LL crossings of the MLG- and BLG-like subbands. For $B > 4$ T, the SdH minima are separated by $\Delta\nu = 1$ or 2, indicating the splitting of LLs. **b,** Color map of ρ_{xx} versus n and B at 300 mK. The diagonal lines correspond to constant filling factor lines. The beating pattern, most visible at negative densities, is a consequence of LL crossings. The white central region corresponds to an insulating state at zero density (see supplementary information). **c,** Calculated LL energy spectrum in TLG for the SWMcC parameters obtained from **b**. The red dashed and black lines are LLs at K and K′ points respectively. The roughly $\sqrt{B}$-like and linear B-like dispersion from the MLG- and BLG-like subbands is evident. Each line corresponds to a spin degenerate LL. **d,** Calculated density of states as a function of density and B from the LL spectrum in **c**. Apart from the LL splitting, the location of the LL crossings agrees very well with the experimental data in **b**. **e,** ρ_{xx} and σ_{xy} as a function of filling factor for $B = 7.3, 7.8$, and 8.3 T. The highlighted orange region shows the appearance of the LL crossing at $\nu = -23$ while the green highlighted region shows the LL splitting occurring at $\nu = -20$.

valley (K and K′) and spin (up and down) degrees of freedoms in both the MLG-like and BLG-like subbands. When LLs from these two subbands cross at a given B, the coexistence of two 4-fold degenerate LLs increases the degeneracy to 8-fold. This 8-fold degeneracy is highlighted by the green bands in Fig. 5.6a, where ν changes by 8 from minimum to minimum instead of by 4. For $B \geq 4$ T, the splitting of the LLs results in ν changing by either 1 or 2, as the different broken-symmetry quantum Hall states are occupied.

A more complete understanding of the TLG LL energy spectrum is obtained by plotting ρ_{xx} as a function of n and B as shown in Figure 2b. The resulting fan diagram lines correspond to the SdH oscillations mentioned above, while the white central region corresponds to an insulating behavior at $\nu = 0$ (see supplementary information for details). The abovementioned crossings of MLG-like and BLG-like LLs manifest themselves as a beating pattern in the SdH oscillations, with a greater number of them and more visible on the hole side ($n < 0$). This electron-hole asymmetry results from the TLG band structure, as we show below. In addition, the LL splittings appear as finer split lines in the SdH oscillations. For each LL crossing, there is an enhancement of ρ_{xx} due to the enhanced density of states [107, 108], and each crossing point can be uniquely identified by B and ν. For instance, at $B \sim 3\,\mathrm{T}$ and $n \sim -4 \times 10^{12}\,\mathrm{cm}^{-2}$, the filling factors associated with the minima in the corresponding SdH oscillations change from 50 to 58 indicating that the crossing occurs at $\nu = 54$.

The positions of the crossings in B and ν space depend sensitively on the TLG band structure, and therefore enable a direct electronic transport determination of the relevant SWMcC parameters for TLG. These parameters, proposed to explain the band structure of graphite [58], describe the different intra- and inter-layer hopping terms in the different graphene sheets (Fig. 5.1b). We note that TLG is the fewest layer graphene

system whose description includes all the SWMcC parameters. The simplest TLG model, in which only the nearest intra- and inter-layer couplings (γ_0 and γ_1) are considered (the ones typically used to describe MLG and BLG), results in symmetric electron and hole bands (Fig. 5.1c) and therefore is clearly insufficient to explain the experimental data. We therefore use all the relevant SWMcC parameters to numerically calculate the LL energy spectrum (Fig. 5.6c) and density of states as a function of B (Fig. 5.6d), and perform a minimization procedure to fit the experimental data in Fig. 5.6b. In order to lower the number of parameters, we take $\gamma_0 = 3.1$ eV, $\gamma_1 = 0.39$ eV and $\gamma_3 = 0.315$ eV (see supplementary information), and we obtain from our fit the following values of the SWMcC parameters; $\gamma_2 = -0.028(4)$ eV, $\gamma_4 = 0.041(10)$ eV, $\gamma_5 = 0.05(2)$ eV, and $\delta = 0.046(10)$ eV. The definitions of the γ_i can be found in Fig. 5.1b and δ is the on-site energy difference between the two-inequivalent carbon sublattices residing in the same graphene layer. The values of the SWMcC parameters obtained are similar to previously reported values for graphite [58] and, apart from the broken-symmetry states (see discussion below), our data agree very well with the LLs corresponding to Bernal stacked TLG, and not to rhombohedral stacked TLG [61]. These parameters result in the overall electron-hole asymmetric band structure shown in Fig. 5.1d, with small band gaps $E_{\mathrm{g,S}} \sim 7$ meV and $E_{\mathrm{g,B}} \sim 14$ meV, for the MLG- and BLG-like subbands, and a band overlap $E_{\mathrm{o}} \sim 14$ meV.

5.6 Landau level crossings between broken-symmetry states

The LLs in TLG are not truly 4-fold degenerate even in a single particle picture, owing to the finite value of γ_2, γ_5, and δ, which break valley degeneracy (Fig. 5.6c) [109], in addition to the Zeeman interaction which breaks spin degeneracy. Our data at high B

(Fig. 5.6a and 5.6b) show that the splitting of 4-fold degenerate LLs is observed up to filling factors as high as $\nu = 46$. While single particle effects may partly explain these broken-symmetry QH states (e.g. from the width of the LLs crossings, we estimate the disorder broadening of the LLs to be $\sim$1 mV which is similar to the the Zeeman splitting at $\sim$8 T), it is likely that electron-electron (e-e) interactions play a significant role too, as it is the case in MLG and BLG [27, 40, 110–112]. For example, the insulating behavior we observe at $\nu = 0$, cannot be explained by single particle effects, given the band overlap between the MLG- and BLG-like subbands, and the single particle LL energy spectrum shown in Fig. 5.6c. However, a more detailed study including measurements of the gap energies and measurements in tilted magnetic fields, beyond the scope of this paper, is necessary to investigate the precise role of e-e interactions in TLG. Figure 2e shows example traces where the different behavior of LL crossings and LL splitting can be seen.

At high B, the LL crossing points should become crossing manifolds due to the crossing between the split MLG- and BLG-like LLs. One such example is shown in Fig. 5.8a. From the LL energy spectrum shown in Fig 5.6c, the manifold corresponds to the crossing between the $N = -1$ LL of the MLG-like subband, $\mathrm{LL}_{\mathrm{S}}^{-1}$, and the $N = -5$ LL of the BLG-like subband, $\mathrm{LL}_{\mathrm{B}}^{-5}$. In order to reproduce the observed degeneracies at the crossings, the 4-fold $\mathrm{LL}_{\mathrm{S}}^{-1}$ has to completely split into four singly-degenerate LLs while the 4-fold $\mathrm{LL}_{\mathrm{B}}^{-5}$ splits into 3 LLs: two singly degenerate LLs and one doubly degenerate LL. Figure 3b shows schematically the full 12-point manifold, of which only 6 crossing points are visible in our density and B range. We have found that this splitting scheme is the only one that yields the correct result for both the degeneracies at the crossings and the filling factors at which they occur. The observation of the full 4-fold splitting of the $\mathrm{LL}_{\mathrm{S}}^{-1}$ in TLG, although expected, is remarkable since previous transport studies of the $N = 1$ LL in MLG

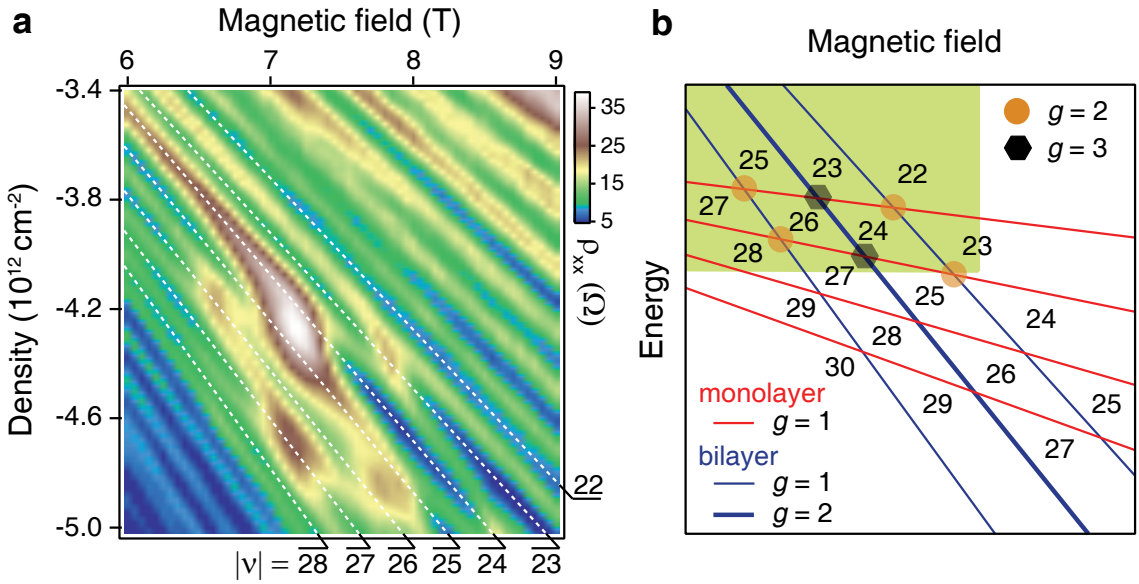

Figure 5.7: **LL crossings between broken-symmetry states. a,** ρ_{xx} as a function of density and B at 300 mK showing a manifold of LL crossing points. The high ρ_{xx} regions correspond to enhanced degeneracy due to LL crossings. Five crossing points are clearly visible and the sixth point is starting to appear in the lower-right corner. White dashed lines are guides to the eye for each ν labeled on the edges. **b,** Schematic splitting and crossing of LLs yielding the manifold of crossings shown in **a**. Red and blue lines represent the split LL spectrum for the broken-symmetry QH states of the $N = -1$ LL from the MLG-like subband and the $N = -5$ LL from the BLG-like subband, respectively. The degeneracies for each level are $g = 1$ for thin lines and $g = 2$ for the thick line. The highlighted green area corresponds to the region observed in the data in **a**. The numbers inside each region show the corresponding filling factors

had reported only the breaking of some of the degeneracies [25, 110], and the full 4-fold splitting has only been seen in recent STM experiments [113]. The 1-2-1 splitting of LLs from the BLG-like subband, however, is more anomalous. Naively, one would expect the splitting to be either 2 fold or 4 fold, depending on whether one of the two degrees of freedom (valley or spin) is split or both are [27, 112]. However, we note that this 1-2-1 splitting may also be present in a recent study of BLG on hBN in the intermediate B-regime [40], and may possibly indicate a richer phase diagram based on SU(4) rather than SU(2)xSU(2) symmetry breaking. A detailed study of the crossing between spin/valley polarized LLs of massless and massive Dirac Fermions, together with the aforementioned possible role of e-e interactions, could potentially lead to some intriguing phenomena such as phase transitions in quantum Hall ferromagnets [107, 114].

5.7 Unconventional quantum Hall effect in TLG

Although the splitting of the LLs at high B provides insight into broken symmetries in TLG in the QH regime, it also masks out the QH plateaus expected within the simplest single particle model for TLG. The sequence of plateaus arising from such simple models has proven a useful tool in identifying MLG and BLG [4, 5, 95]. For completeness, Figure 4 shows ρ_{xx} and σ_{xy} at $B = 9$ T before current annealing, i.e. in the presence of increased disorder which prevents the observation of LL splitting. In the simplest model, the QHE plateaus are expected at $\sigma_{xy} = \pm 4(N + 1/2 + 1)e^2/h$ for $N = 0, 1, \ldots$ where the 12-fold zero energy LL results from the 4-fold and 8-fold zero energy LLs of the MLG- and BLG-like subbands, respectively [60, 115]. Our observations agree with this simple prediction for $|\nu| \geq 10$ (with observed plateaus at $\pm 10, \pm 14, \pm 18e^2/h$), but we observe in

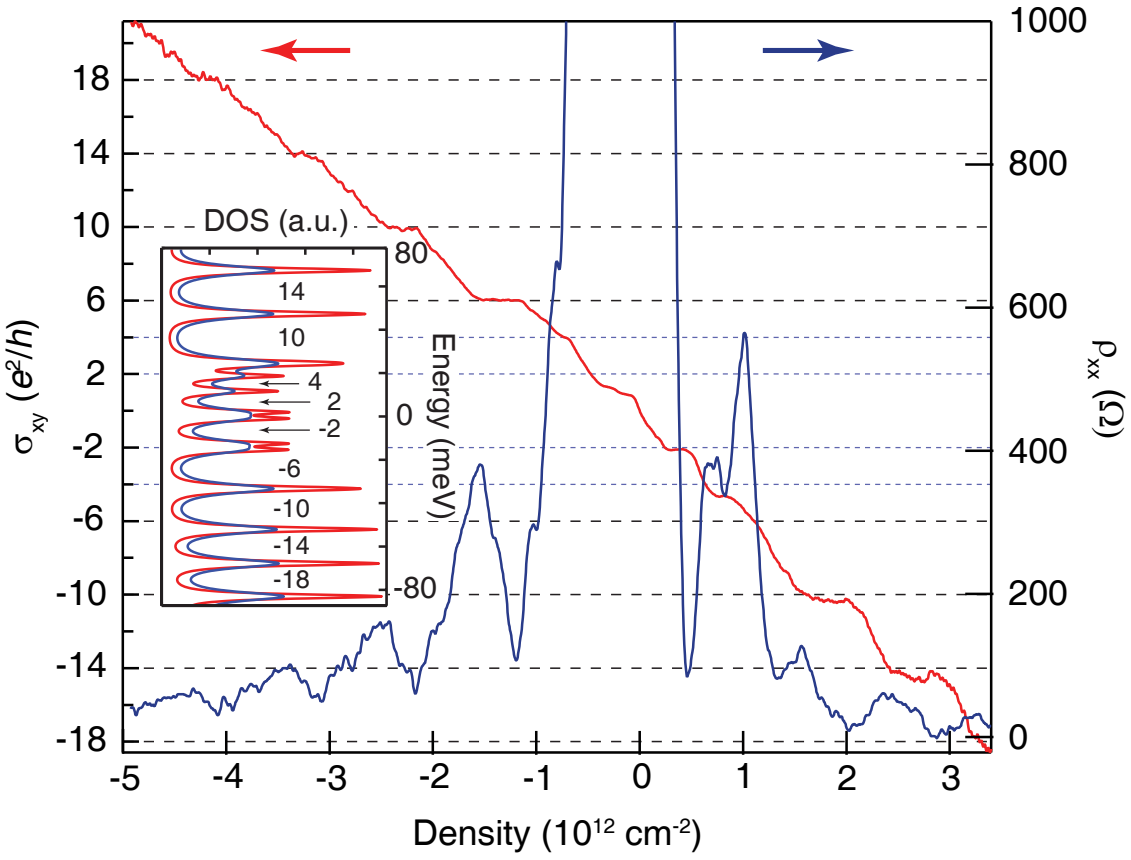

Figure 5.8: **Unconventional quantum Hall effect in TLG.** σ_{xy} and ρ_{xx} as a function of density at $B = 9$ T and $T = 300$ mK, and before the last current annealing step. The dashed lines indicate the expected QH plateaus based on the simplest TLG model approximation. The dotted lines indicate the extra QH plateaus based on the full band structure determined from Fig. 5.6c. (Inset) Calculated Density of states using full SWMcC parameter model. The blue line is calculated using higher disorder broadening than the red line.

addition extra plateaus for $\nu = \pm 2$ and ± 4 as well as the absence of a plateau at $\nu = +6$. This unconventional QHE can be explained within the band model calculated using the SWMcC parameters obtained from Fig. 5.6a-c. In such model, the non-zero values of γ_2, γ_5, and δ lift the degeneracy of the "zero-energy" LLs of the MLG- and BLG-like subbands (Fig. 5.6c). In addition, the 4-fold degenerate $N = 0$ LL of the MLG-like subband splits into two 2-fold degenerate valley polarized LLs and the 8-fold degenerate (spin, valley and N=0,1 LLs) zero energy LLs of the BLG-like subband splits into two 4-fold degenerate LLs (the splitting between $N = 0$ and $N = 1$ LLs remains relatively small compared to the valley splitting). We note that the Zeeman splitting is at least an order of magnitude smaller than other types of splitting even at 9 T which is the reason why LLs remain spin degenerate in this non-interacting model.

The inset to Fig. 5.7 shows the calculated density of states as a function of energy at 9 T. The zero density is located between two nearly degenerate LLs, each with 2-fold degeneracy which explains the observed plateaus at $\nu = \pm 2$. The absence of a plateau at $\nu = 0$ is likely due to disorder, which smears out the small energy gap between these two LLs. The plateaus at $\nu = \pm 4$ stem from the next 2-fold degenerate LLs. However, these plateaus are not yet completely developed at 9 T, especially the one at $\nu = -4$ ($\sigma_{xy} = 4e^2/h$) which coincides with the small energy gap between this LL and the next one. Finally, the absence of a plateau at $\nu = +6$ ($\sigma_{xy} = -6e^2/h$) is due to the crossing between a 2-fold and a 4-fold degenerate LL. The degeneracy at the crossing becomes 6-fold and causes the position of the plateau to step from $\nu = 4$ to $\nu = 10$ (the non-developed $\nu = 4$ plateau does not reach its exact value at $\sigma_{xy} = -4e^2/h$). Unlike MLG and BLG in which the sequence of the plateaus are the same for all B, the observed plateaus in TLG depend on B because of the LL crossing.

5.8 Supplementary information

5.8.1 Determination of SWMcC parameters

The hamiltonian for Bernal stacked TLG with SWMcC parameters is given by [116]

$$H = \begin{bmatrix} H_m & D \\ D^\dagger & H_b \end{bmatrix},$$

where

$$D = \begin{bmatrix} \Delta_1 & 0 & 0 & 0 \\ 0 & 0 & 0 & \Delta_1 \end{bmatrix}, \quad H_m = \begin{bmatrix} \Delta_2 - \gamma_2/2 & v_0\pi^\dagger \\ v_0\pi & \Delta_2 - \gamma_5/2 + \delta \end{bmatrix},$$

$$H_b = \begin{bmatrix} \Delta_2 + \gamma_2/2 & \sqrt{2}v_3\pi & -\sqrt{2}v_4\pi^\dagger & v_0\pi^\dagger \\ \sqrt{2}v_3\pi^\dagger & -2\Delta_2 & v_0\pi & -\sqrt{2}v_4\pi \\ -\sqrt{2}v_4\pi & v_0\pi^\dagger & -2\Delta_2 + \delta & \sqrt{2}\gamma_1 \\ v_0\pi & -\sqrt{2}v_4\pi^\dagger & \sqrt{2}\gamma_1 & \Delta_2 + \gamma_5/2 + \delta \end{bmatrix}.$$

The SWMcC parameters γ_i for Bernal stacking TLG are shown in Fig. 5.1b with the corresponding effective velocity $v_i = (\sqrt{3}/2)a\gamma_i/\hbar$ and δ is the on-site energy difference between A and B sublattices. The parameters $\Delta_1 = (U_1 - U_3)/2$ and $\Delta_2 = (U_1 - 2U_2 + U_3)/3$ describe energy difference between layers where U_i is the potential of layer i. The basis for this hamiltonian is $(\psi_{\mathrm{A1}} - \psi_{\mathrm{A3}})/\sqrt{2}$, $(\psi_{\mathrm{B1}} - \psi_{\mathrm{B3}})/\sqrt{2}$, $(\psi_{\mathrm{A1}} + \psi_{\mathrm{A3}})/\sqrt{2}$, ψ_{B2}, ψ_{A2}, and $(\psi_{\mathrm{B1}} + \psi_{\mathrm{B3}})/\sqrt{2}$ which reflects the even and odd parity with respect to mirror symmetry of Bernal stacked TLG. We use this hamiltonian to calculate Landau levels numerically by rewriting $\pi^\dagger$ as $\sqrt{2\hbar eB}a^\dagger$ for K′ point and $\sqrt{2\hbar eB}a$ for K point respectively where $a^\dagger$ and a are creation and annihilation operators for simple harmonic oscillation [61]. Figure 5.9 shows how the different parameters affect the band structure and LL energy spectrum.

To determine the SWMcC parameters, we set $\gamma_0 = 3.1$ eV which corresponds to $v_0 = 1 \times 10^6$ m/s [4,5,101,102,113,117] and $\gamma_1 = 0.39$ eV [49,51,58,101,118–120]. We vary γ_2, γ_3, γ_4, γ_5 and δ and numerically determine the magnetic fields B^{t} and filling factors ν^{t} at which LL crossings occur. We then compare B^{t} and ν^{t} with the crossing points observed experimentally. Twelve crossing points can be resolved in the data (Fig. 5.6, 5.10 and Table 5.1). The best set of SWMcC parameters is the one which yields the correct ν^{t} and the minimum value of

$$\xi = \sum_{i=1}^{12} \left(\frac{B_i^{\mathrm{t}} - B_i^{\mathrm{exp}}}{\Delta B_i^{\mathrm{exp}}} \right)^2 ,$$

where B_i^{exp} and $\Delta B_i^{\mathrm{exp}}$ are the values of magnetic field and their uncertainties at the crossing points, determined experimentally (Fig. 5.6 and 5.10). In addition, according to the data at 9 T (Fig. 5.7), in which we observe the quantized conductance at $\nu = 4$ but not at $\nu = 6$, we require that the energy gap at $\nu = 4$ has to be larger than the gap at $\nu = 6$.

We find that the positions of the crossing points depend much more strongly on γ_2, γ_5, and δ than on γ_3 and γ_4 (see Fig. 5.9. In fact, the crossing points are almost not affected by γ_3. This is because the effect of γ_3 on the band structure is to introduce trigonal warping in the bilayer-like subband at very low energies. This trigonal warping causes only a slight change in the very low-lying LLs at low magnetic field [54], and these are not well resolved in our data (Fig. 5.6 and Fig. 5.13), which prevents us from using those LL crossings in our fitting procedure. Therefore we set γ_3 to a fixed value of 0.315 eV [58], and vary γ_2, γ_4, γ_5, and δ. We obtain $\gamma_2 = -0.028(4)$ eV, $\gamma_4 = 0.041(10)$ eV, $\gamma_5 = 0.05(2)$ eV, and $\delta = 0.046(10)$ eV. Our data cannot determine γ_5 and δ individually accurately because we can access only the low lying term $-\gamma_5/2 + \delta$ in the hamiltonian while the other term $\gamma_5/2 + \delta$ is much higher in energy due to the hybridization through the

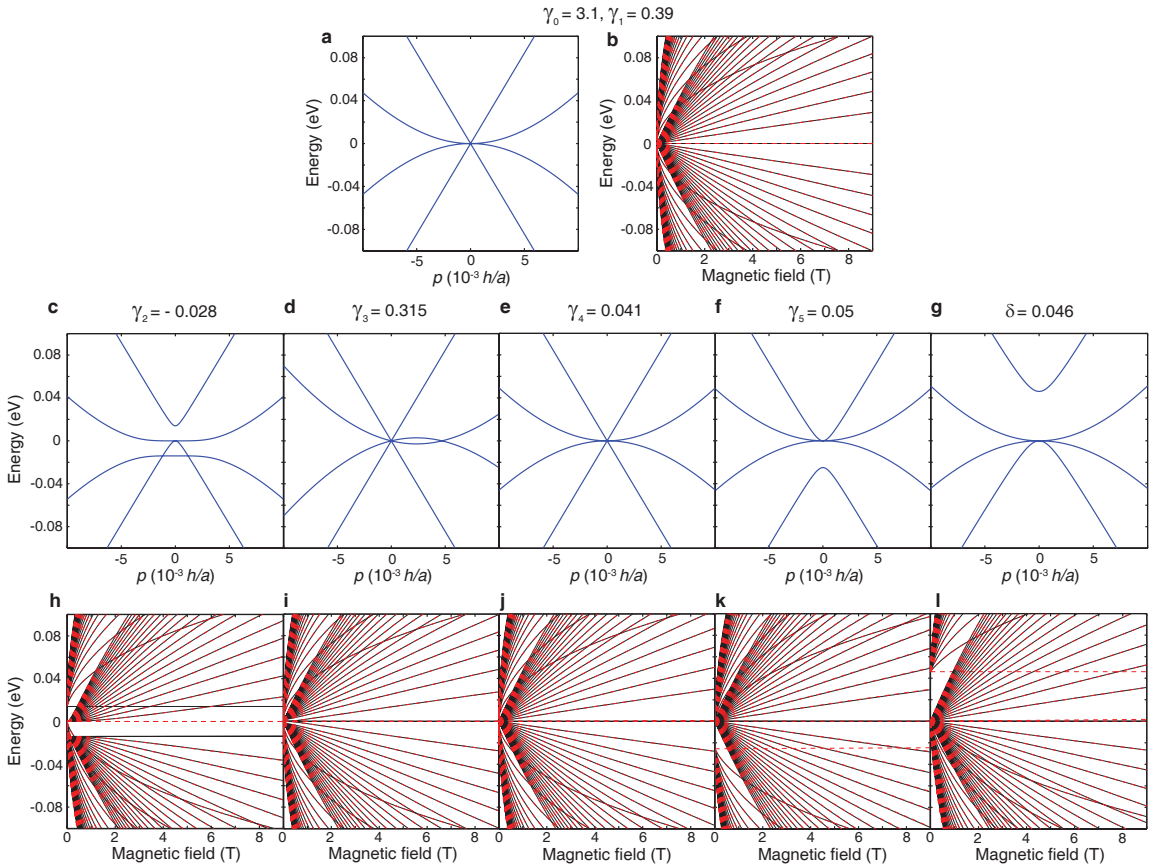

Figure 5.9: **Dependence of TLG band structure and Landau levels on the SWMcC parameters. a-b,** Band structure and Landau levels of TLG with $\gamma_0 = 3.1$ eV and $\gamma_1 = 0.39$ eV. **c-l,** Band structure and Landau levels of TLG with nonzero γ_i (shown on top of each plot) and $\gamma_0 = 3.1$ eV and $\gamma_1 = 0.39$ eV.

Table 5.1: **Magnetic fields and filling factors at which LL crossings occur.** We determine B^{exp} from the position of magnetic field at which σ_{xx} is locally maximum (data not shown).

N^{th} $\mathrm{LL_S}$	N^{th} $\mathrm{LL_B}$	ν^{exp}	B^{exp} (T)
-1	-5	-26	7.31
-1	-6	-30	3.04
-2	-11	-54	3.07
-2	-12	-58	2.09
-3	-16	-78	2.57
-3	-17	-82	1.98
-3	-18	-86	1.51
-4	-22	-106	1.78
-4	-23	-110	1.44
-5	-27	-130	1.56
-5	-28	-134	1.35
0	6	23	1.75

nearest inter-layer coupling γ_1. However, we can determine $-\gamma_5/2+\delta$ with better accuracy and obtain $-\gamma_5/2+\delta = 0.021(3)$ eV.

We have also tried varying γ_0 and γ_1 in order to determine how sensitively the other SWMcC parameters depend on these two parameters. We perform a calculation of the influence of a $\pm 10\%$ variation in the value of γ_0. For γ_0 in the range of $[2.8, 3.4]$ eV ($\pm 10\%$ of 3.1 eV), the values of γ_2, γ_4, γ_5, and δ still fall within their estimated errors, as long as the ratio between $\gamma_0/\gamma_1 = 8.0 \pm 0.2$. For γ_0 values of 2.8, 3.1, and 3.4 eV, this results in γ_1 values of 0.35, 0.39, and 0.43 eV, respectively. The reason for the linear relation between γ_0 and γ_1 stems from the fact that the Landau level dispersions for MLG and BLG are proportional to γ_0 and γ_1 respectively. Hence, in order for the Landau levels from both subbands to cross at the same magnetic field and filling factors, both γ_0 and γ_1 have to change proportionally.

We note that we have set $\Delta_1 = 0$ and $\Delta_2 = 0$. The effect of Δ_1 is to hybridize the

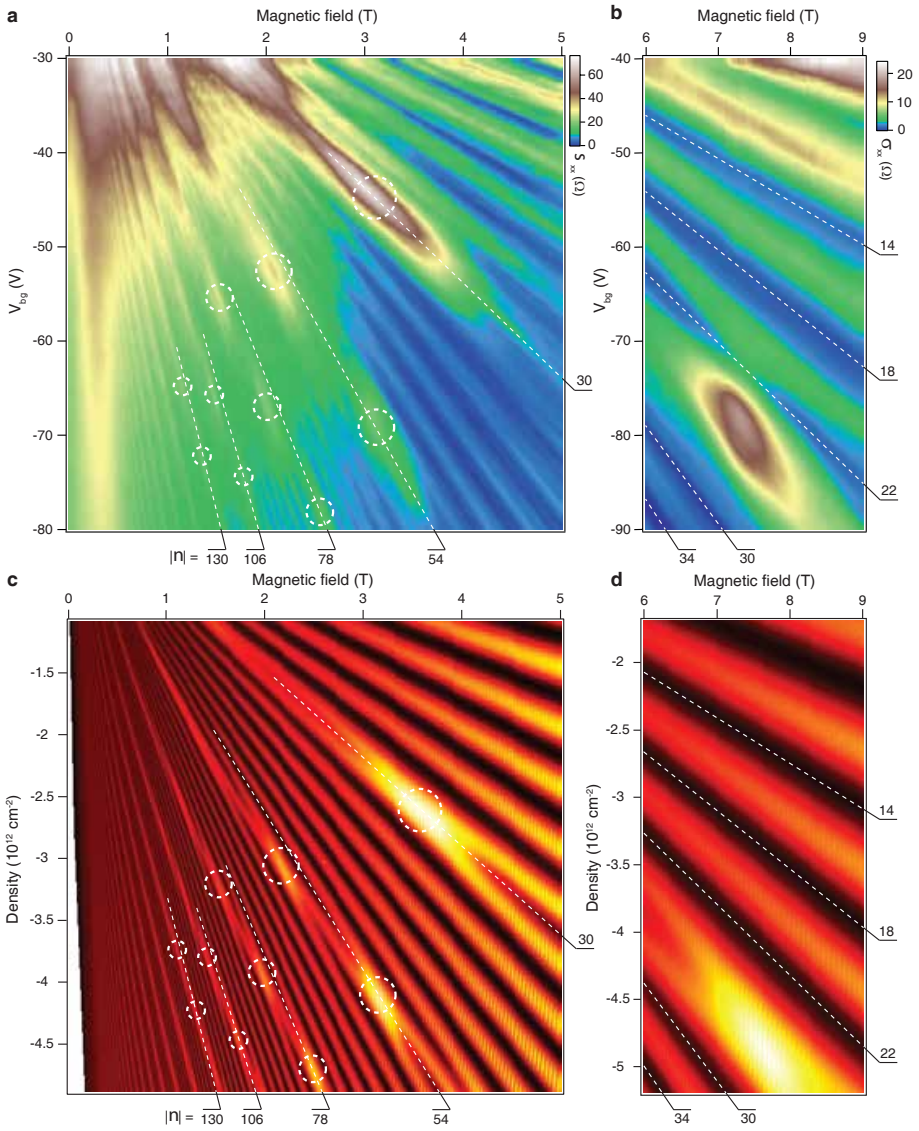

Figure 5.10: **Landau fan diagram. a,** Color map of Landau fan diagram as a function of back-gate voltage and magnetic field at 300 mK. White dashed lines are guides to the eye with filling factors labeled on the edge and the white dashed circles indicate crossing points. **b,** Landau fan diagram from 6 to 9 T at 300 mK. The measurement is taken when the sample quality is not high enough to observe LL splitting (Fig. 5.8a). The absence of the minimum at $\nu = -26$ can be seen clearly indicating Landau level crossing. **c,** Calculated DOS as a function of density and magnetic field. Here we use $\Gamma = 1$ mV and the following SWMcC parameters: $\gamma_0 = 3.1$ eV, $\gamma_1 = 0.39$ eV, $\gamma_2 = -0.028$ eV, $\gamma_3 = 0.315$ eV, $\gamma_4 = 0.041$ eV, $\gamma_5 = 0.05$ eV, and $\delta = 0.046$ eV. **d,** Calculated DOS as a function of density and magnetic field with $\Gamma = 2.5$ mV and the same SWMcC parameters as in **c**.

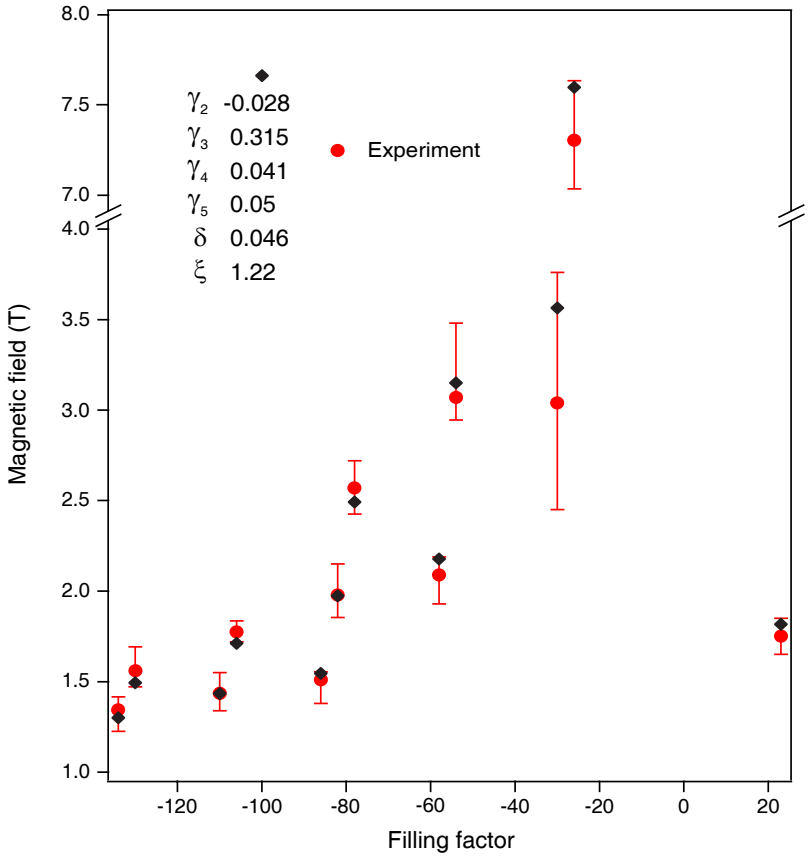

Figure 5.11: **Crossing coordinates.** The positions of the crossing points in magnetic field and filling factor for different sets of parameters. The red circles are the positions of the crossing points determined experimentally.

MLG-like and BLG-like subbands, which lifts two of the four low energy subbands to higher energy. Δ_2 induces a small gap in the BLG-like subband. It is reasonable to set $\Delta_2 = 0$ because, in a linear response calculation, Δ_2 is always zero and, using a self-consistent calculation, Δ_2 is still less than 1 mV [116]. However, the value of Δ_1 could be as high as 50 mV at the density of $\sim 4 \times 10^{12}$ cm^{-2} ($\sim$60 V in back gate voltage) which we access experimentally [116]. Such value of Δ_1 should affect the LL spectrum, and therefore the crossing points, strongly. However, we were unable to find a set of SWMcC parameters which would describe our crossing points for values of Δ_1 larger than about 10 meV, and the agreement was best for values of Δ_1 equal to zero. The naive picture of using a single value of Δ_1 to describe the data at all densities is clearly not sufficient, because Δ_1 depends on the carrier density we induce in the system via the back gate voltage. Therefore we have also performed the calculation with Δ_1 varying linearly with energy ($\Delta_1 = E/2$) (in a phenomenological model similar to the results obtained in ref.S1), and we still find disagreement between our data and the Landau level spectra expected for those values of Δ_1. One possible reason may be that this model is for zero magnetic field, while our Landau level crossings occur at finite field. Another posibility contributing may be the assumed value of the TLG dielectric constant [116], which may not be known precisely. A more extensive calculation, which includes non-linear screening as a function of density and magnetic field, as well as the possible roles of small disorder and the dielectric response of TLG will have to be developed, and is beyond the scope of this paper. The fact that we can reproduce the experimentally observed LL crossing points with $\Delta_1 = 0$ may imply that high mobility TLG can screen electric field very well at high densities (where the LL crossing points are measured), causing the potential of each layer to be similar.

After obtaining the Landau level spectrum, we calculate the density of states

(DOS) by assuming that the DOS of each Landau level is of the form

$$\mathrm{DOS}(E; E_{\mathrm{LL}}) = \frac{2B}{h/e}\frac{1}{\pi}\frac{\Gamma/2}{(E - E_{\mathrm{LL}})^2 + (\Gamma/2)^2},$$

where E_{LL} is the energy of the LL and Γ is the broadening of the LL due to disorder. The factor of 2 in front comes from spin degeneracy. We calculate the LL spectrum separately for K and K′ because of their non degeneracy. The total DOS can be obtained by summing over the DOS of each Landau level

$$\mathrm{DOS}_{\mathrm{total}}(E) = \sum_{E_{\mathrm{LL}}} \mathrm{DOS}(E; E_{\mathrm{LL}}).$$

We then integrate total DOS in order to obtain the DOS as a function of density and B which can be used to compare with the experimental data. Figure 5.12 shows the different LL energy spectra and fan diagrams for the SWMcC parameters for graphite from different sources (see Table 5.2), and the comparison with the spectrum and fan diagram for the SWMcC parameters for TLG obtained in this work.

We note that Landau level spectra of both massless and massive Dirac fermions have been observed previously in scanning tunneling spectroscopy measurements on HOPG graphite surfaces [101, 117]. Although this is similar to what occurs in TLG, the results are very different (for example those measurements show that the Landau levels of these two species share the same Dirac point in contrast to our extracted Landau levels). There is no contradiction however because the two systems are very different. Those two groups regard these linear and $\sqrt{B}$ dispersing LLs as surprising, since this behavior is not observed in Kish graphite, and speculate that perhaps their HOPG graphite flakes contain stacking faults or turbostratic groups of sheets. The authors however cannot extract how many stacking faults they have or if these are indeed ABA stacked. Moreover, both papers find an effective mass for the massive states which is equal to that of pure BLG, whereas the

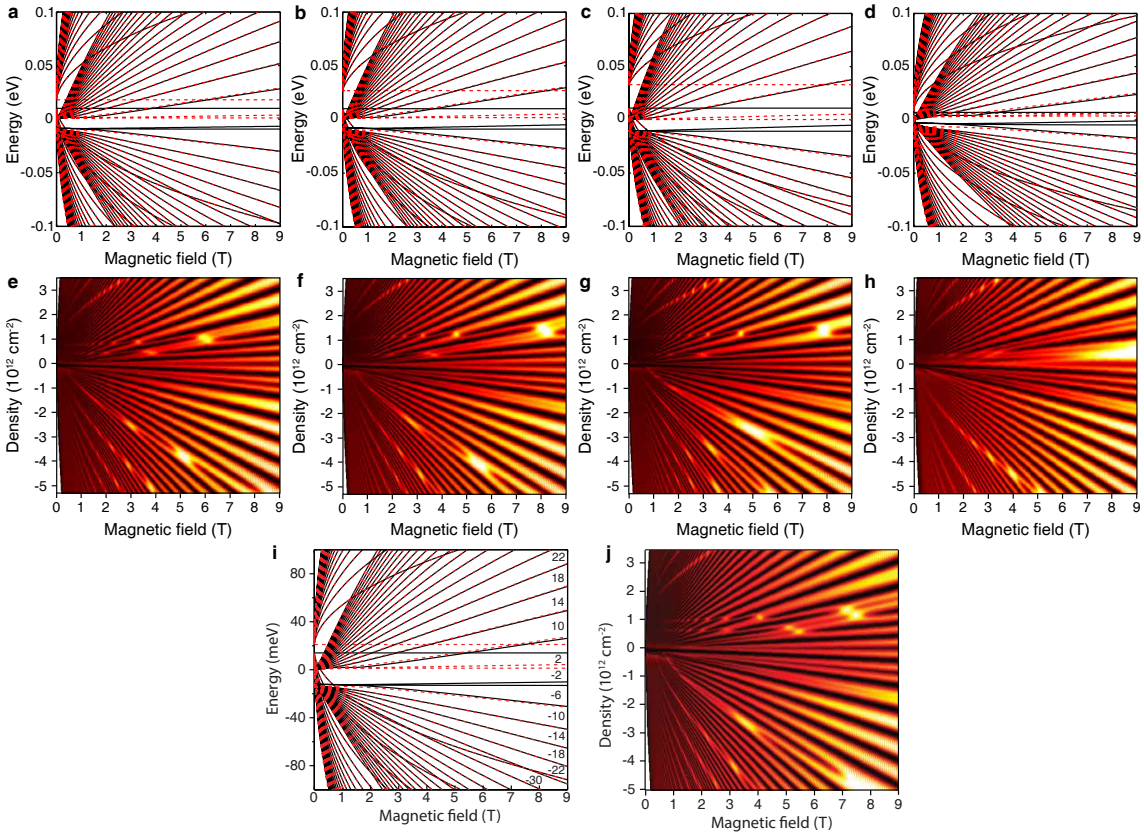

Figure 5.12: **Landau fan diagrams with SWMcC parameters from graphite. a-d,** Landau level energy spectrum as a function of magnetic field using the SWMcC parameters determined from graphite from references [58], [121], [122], and [123] respectively (Table 5.2). Red and black curves represent Landau level from K and K′. **e-f,** Density of states as a function of magnetic field and density calculated from the energy spectrum in **a**, **b**, **c**, and **d** respectively. Figures **e** and **f** looks similar to our data but the crossing point at high field (∼5 T) occurs at $\nu = 30$ instead of $\nu = 26$ observed experimentally. **i-j,** Landau level energy spectrum and density of states using the SWMcC parameters from our TLG data.

BLG-like subband of TLG has an effective mass which is $\sqrt{2}$ larger [116]. Therefore, it is not possible that these experiments are describing ABA stacked trilayer graphene (or higher number of layers, for similar reasons), and these experiments may be equivalent to measuring MLG and BLG independently, and that may explain why their Landau levels

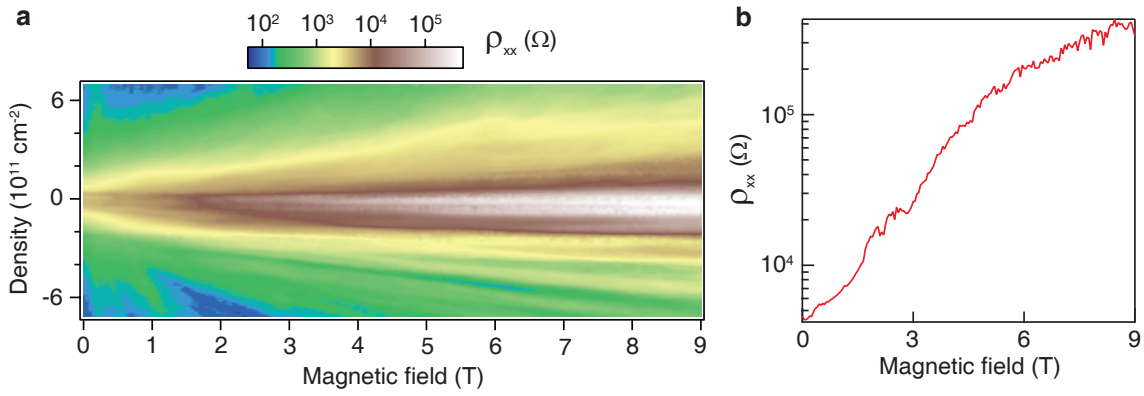

Figure 5.13: **Landau fan diagram at $\nu = 0$. a,** Color map of ρ_{xx} versus density and B at 300 mK. **b,** A slice from **a** at zero density.

share the same Dirac point. In trilayer graphene, however, a spectrum of massless and massive Dirac fermions is theoretically expected to coexist, but it was not demonstrated before due to poor sample quality. In TLG, the offset between the Dirac points, as well as the small gaps in the subbands, are expected [87, 116], in agreement with our data.

5.8.2 Insulating behavior at $\nu = 0$

We observe an insulating behavior in ρ_{xx} at zero density as we increase B. The longitudinal resistivity ρ_{xx} increases from 4.5 kΩ at 0 T to 400 kΩ at 9 T. This insulating behavior at ν=0 is also observed in MLG and BLG [27, 40, 110, 112]. In those systems, electron-electron interactions are required to break the symmetry of the zero energy LL. In TLG, due to the finite values of γ_2, γ_5, and δ, which cause valley splitting in the MLG- and BLG-like subbands LLs as well as breaking of the $N = 0$ and 1 LLs in BLG-like subband, there are no LLs at zero density. In general, the valley degeneracy is associated with a spacial inversion symmetry which is present in both MLG and BLG. However, Bernal

stacked TLG does not preserve spatial inversion symmetry and hence the valley degeneracy is not guaranteed [60]. However, the finite band overlap implies that there should be edge modes present always, for any value of the Fermi energy (or density) [124]. Therefore, electron-electron interactions may play a role in this insulating behavior. Note that this insulating phase has also been observed in a suspended TLG sample [104].

Table 5.2: **SWMcC parameters.** SWMcC parameters obtained from fitting the positions of the LL crossings are shown in row 1. The parameters obtained previously on graphite by means of experiment (Exp) and density functional theory (DFT) are listed in rows 2 to 4. In the last row, the parameters for BLG as determined by infrared spectroscopy. We note that γ_2 and γ_5, which describe the hopping between the first and the third layers, are not present in BLG. Rows 2-5 of this table are adopted from Zhang *et al* [49].

Source	γ_0	γ_1	γ_2	γ_3	γ_4	γ_5	δ
TLG (Pres. Result)	3.1[†]	0.39[†]	-0.028(4)	0.315[†]	0.041(10)	0.05(2)	0.046(10)
Graphite Exp [58]	3.16(5)	0.39(1)	-0.020(2)	0.315(15)	0.044(24)	0.038(5)	0.037(5)
Graphite Exp [121]	3.11	0.392	-0.0201	0.29	0.124	0.0234	0.0386
Graphite DFT [122]	2.92	0.27	-0.022	0.15	0.10	0.0063	0.0362
Graphite DFT [123]	2.598(15)	0.364(20)	-0.014(8)	0.319(20)	0.177(25)	0.036(13)	0.024(18)
BLG [49]	3.0	0.40(1)	0.0	0.3	0.15(4)	0.0	0.018(3)

[†] The values of γ_0 and γ_1 are taken from literature where the reported values from different experiments have been consistent. The value of γ_3 cannot be determined accurately and hence is taken from ref. [58].

Chapter 6

Electrically tunable transverse magnetic focusing in graphene

Abstract

Electrons in a periodic lattice can propagate without scattering for macroscopic distances despite the presence of the non-uniform Coulomb potential due to the nuclei [125]. Such ballistic motion of electrons allows the use of a transverse magnetic field to focus electrons [126]. This phenomenon, known as transverse magnetic focusing (TMF), has been used to study the Fermi surface of metals [127] and semiconductor heterostructures [128], as well as to investigate Andreev reflection [127], spin-orbit interaction [129], and to detect composite fermions [130, 131]. Here we report on the experimental observation of transverse magnetic focusing in high mobility mono-, bi-, and tri-layer graphene devices. The ability to tune the graphene carrier density enables us for the first time to investigate TMF continuously from the hole to the electron regime and analyze the resulting "focusing fan". Moreover, by applying a transverse electric field to tri-layer graphene, we use TMF as a

ballistic electron spectroscopy method to investigate controlled changes in the electronic structure of a material. Finally, we demonstrate that TMF survives in graphene up to 300 K, by far the highest temperature reported for any system, opening the door to novel room temperature applications based on electron-optics.

6.1 Introduction

The concept of TMF can be illustrated by considering electrons entering a two-dimensional system through a narrow injector (origin in Fig. 6.1a). In the presence of a magnetic field B, electrons will undergo cyclotron motion with radius r_c and get focused on the caustic (a quarter of a circle with radius $2r_c$) on which the electron density becomes singular. (Fig. 6.1a, top). Moreover, the specular reflection of electrons at the boundary of the two-dimensional system causes a skipping orbit motion which results in focal points at integer multiples of $2r_c$ along the x-axis (Fig. 6.1a, bottom). This basic behavior still holds for electron motion in a solid as long as the Fermi surface has cylindrical symmetry [127]. Hence, the magnetic field, B_f, required to focus electrons at a distance L is

$$B_{\mathrm{f}}^{(p)} = \left(\frac{2\hbar k_{\mathrm{F}}}{eL}\right) p = \left(\frac{2\hbar\sqrt{\pi n}}{eL}\right) p \tag{6.1}$$

where $p-1$ is the number of reflections off the edge of the system (e.g. $p = 1$ corresponds to direct injector to collector trajectory, without reflections), $\hbar$ is the reduced Planck's constant, e is the elementary charge, k_{F} is the Fermi momentum, and where we have used $k_{\mathrm{F}} = \sqrt{\pi n}$, n being the carrier density.

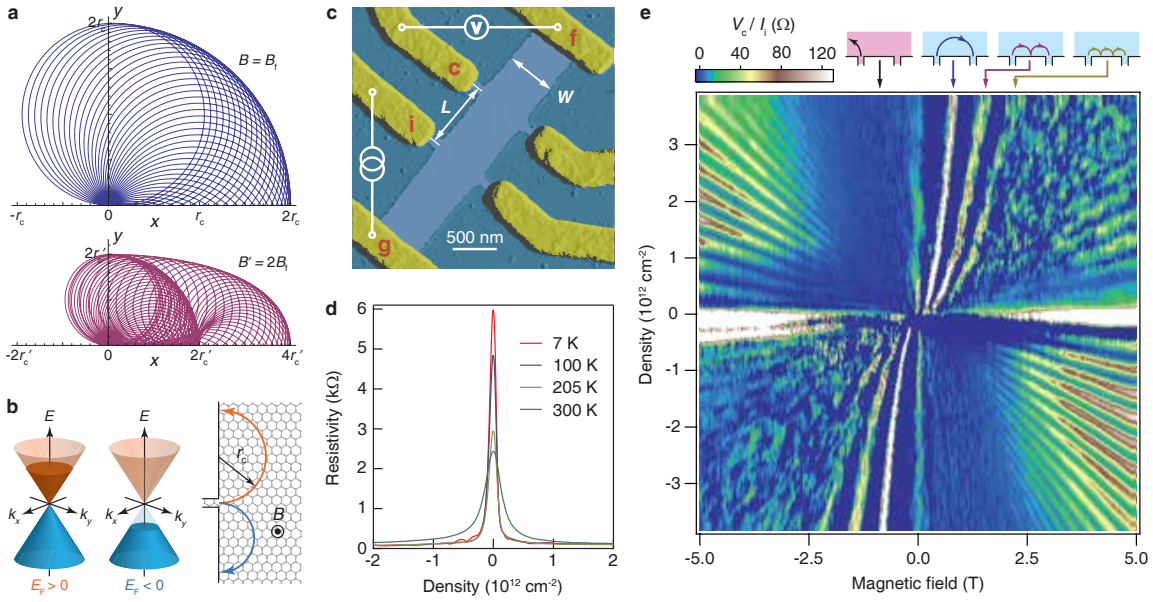

Figure 6.1: **Transverse magnetic focusing schematics.** **a**, Classical trajectories of electrons injected isotropically from the origin at $B = B_{\mathrm{f}}$ (top) and $B' = 2B_{\mathrm{f}}$ (bottom, including one bounce off the edge). Electrons are focused at an integer multiple of $2r_{\mathrm{c}}$ along the x-axis. **b**, Cartoons depicting the band structure of MLG at positive (left) and negative (center) electron density. Electron's trajectories at a finite B are shown on the right for Fermi energy $E_{\mathrm{F}} > 0$ (orange line) and $E_{\mathrm{F}} < 0$ (blue line). **c**, False color atomic force microscopy (AFM) image of a TMF device. In the TMF measurement, contact i injects current I_i into graphene and the voltage V_c is measured at the collector (contact c) relative to contact f. L is the measured distance between the centers of contacts i and c. **d**, Resistance versus gate voltage of MLG at various temperatures measured in the usual 4-probe Hall bar geometry. **e**, TMF spectrum in MLG at 5 K. TMF peaks from first, second, and third modes can be observed clearly for $|B| < 2.5$ T. The top insets show representative trajectories for each corresponding mode. At higher B, SdHOs are also present.

6.2 Device fabrication and characteristic

In order to study TMF in graphene, we fabricate Hall bar devices based on high mobility mono- (MLG), bi- (BLG), and tri-layer (TLG) graphene on hexagonal boron nitride (hBN) substrates [40] (see Methods and Fig. 6.1c). The multi-terminal geometry required to study TMF imposes a minimum mean free path of the order of several hundred nm, which has only been possible with the advent of G on hBN devices [40, 46, 47]. Figure 6.1d shows the resistivity of a MLG device as a function of density at zero magnetic field. The device exhibits a narrow Dirac peak with a strong temperature dependence, which indicates low disorder [22, 106]. Its field effect mobility is $\sim$100,000 $\mathrm{cm^2\,V^{-1}\,s^{-1}}$ at low temperature, corresponding to a mean free path of $\sim$1 μm. A similar behavior is observed for BLG and TLG devices. The high mobility and low disorder enable us to probe TMF in these devices.

6.3 Non-local measurement for TMF

We employ the measurement configuration shown in Fig. 6.1c to probe the focusing of electrons. Current I_i is injected through contact i while contact g is grounded and voltage V_c is measured at the collector (contact c) relative to contact f. The magnetic field is applied normal to graphene. Figure 6.1e shows the normalized $V_\mathrm{c}(B, n)$ in MLG, at 5 K. Two sets of features are immediately apparent: for $|B| \geq 2.5$ T, we observe Shubnikov-de Hass oscillations (SdHOs), forming a usual Landau fan, as expected from the measurement setup, which is topologically equivalent to a longitudinal resistance measurement. While the SdHOs are very pronounced in quadrants 2 and 4 (top-left and bottom-right), they are nearly invisible in quadrants 1 and 3, due to the interference of different trajecto-

ries of electrons propagating coherently to the collector [128, 132–134](see supplementary information).

6.4 TMF in monolayer graphene

In the low field regime, $|B| \leq 2.5$ T, we observe three unusual peaks which do not resemble SdHOs. For positive density, these peaks appear on the positive B side. The location of these features in the $B - n$ plane (see Eq. 1) indicates that these peaks can be associated with TMF. The peaks arise when electrons are focused onto the collector, resulting in a build up of V_c. The first peak corresponds to electrons propagating directly from the injector to the collector while for the higher order peaks electrons reflect off the edge before reaching the collector (Fig. 6.1e, top insets). For negative B, electrons propagate away from the collector and hence no focusing peak is observed (Fig. 6.1e, top left inset). As we tune to negative density ($E_F < 0$), the sign of the charge carriers flips, and therefore B has to be reversed in order for the carriers to be focused at the collector. The ability to tune density in graphene enables us to investigate the $\sqrt{n}$ dependence of the focusing fields, or "focusing fan", continuously from the electron to hole regimes in a single device over a broad density range, which was never done in other systems.

The values of B_f can be readily calculated, since both n and L can be obtained from Hall measurements and the AFM image of the device, respectively. Figure 6.2a shows a zoom-in plot of Fig. 6.1e, where we have superimposed the calculated focusing fields (dashed lines) using the measured $L_{MLG} = 500$ nm. A discrepancy between the calculated values and the measured peak locations is clearly present. Moreover, we find that the observed $B_f^{(p)}/p$ decreases as p increases (Fig. 6.2d). The finite width of our

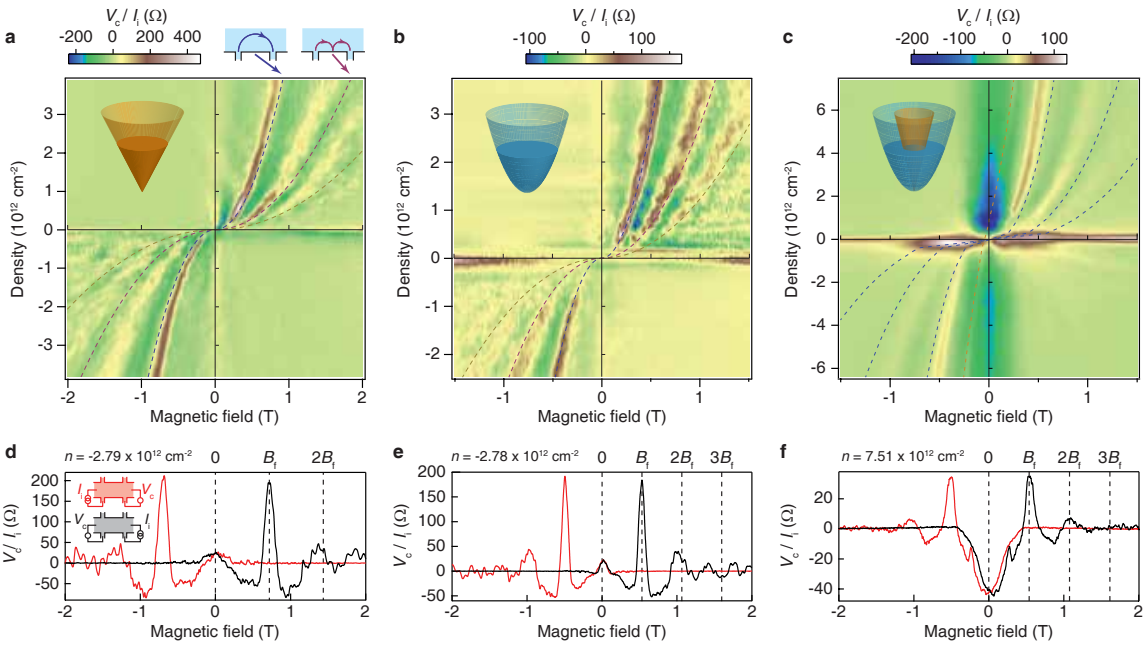

Figure 6.2: **transverse magnetic focusing in MLG, BLG, and TLG at 5 K. a-c**, The TMF spectra as a function of density and magnetic field for MLG, BLG, and TLG respectively. The dashed lines are calculated focusing fields using $L_{\mathrm{MLG}} = 500$, $L_{\mathrm{BLG}} = 775$, and $L_{\mathrm{TLG}} = 950$ nm, determined from AFM images. **d-f**, Onsager reciprocal relation in MLG, BLG, and TLG respectively. The red and black traces are measured with current and voltage contacts switched (Fig. 6.2d, insets). In these figures, B_{f} is the observed focusing field of the first mode.

injector and collector (∼100 nm in MLG and BLG and ∼240 nm in TLG, see below) could introduce an error in the determination of L and subsequently B_{f}. However, a more plausible explanation is the effect of charge accumulation near the edges owing to the finite size of our graphene devices [135]. We find that charge accumulation reduces B_{f} by the same order of magnitude as that required to correct for the discrepancy and, in addition, it also explains the decreasing $B_{\mathrm{f}}^{(p)}/p$ because, for higher p, the carrier's trajectory is closer to the edge, which further reduces $B_{\mathrm{f}}^{(p)}$ (see supplementary information). We also note that density fluctuations and small-angle scattering [133] due to impurities could also affect the carrier's path and its focus. However, a lack of knowledge of the detailed disorder potential landscape prevents us from determining the change in the value of the focusing fields.

We have observed multiple focusing peaks in all of our devices, including BLG and TLG (see below), which indicates that a significant fraction of the electrons get specularly reflected off the graphene edge. From the peak amplitudes, we can calculate the measured specularity, the ratio between the amplitude of the second mode to that of the first mode, which offers information on the specular reflection of electrons at the graphene edges. We find that the value of specularity ranges from 0.2 to 0.5 (see supplementary information). It is worth noting that specularity measurements in semiconductor heterostructures have shown values less than 1 for focused-ion-beam etched devices [127, 128] which is similar to our oxygen-plasma-etched graphene devices but greater than 1 for electrostatically-defined edges.

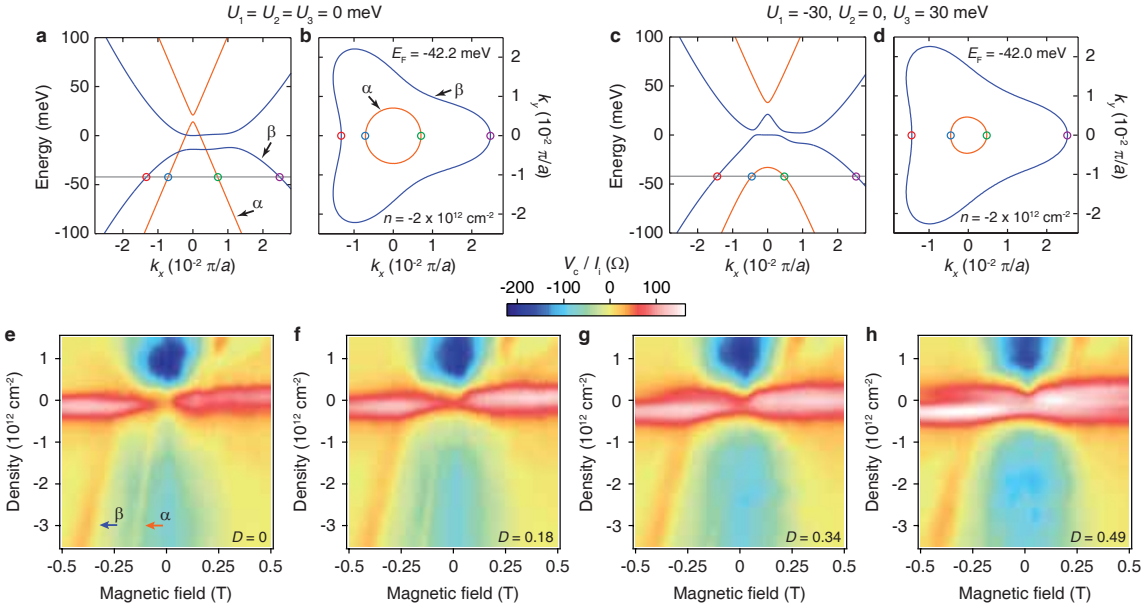

Figure 6.3: **Visualizing in-situ band structure changes in TLG with TMF. a-b**, Band structure and Fermi surface of TLG at zero D (electrostatic potential of each layer equal to zero). The band structure consists of MLG-like and BLG-like subbands, with a small band overlap. The bands α and β are MLG-like and BLG-like valence bands. The trigonal warping effect can be seen in the BLG-like subband. The lattice constant a is 2.46 Å. **c-d**, Band structure and Fermi surface of TLG at finite D (for this case, with potential difference between adjacent layers equal to 30 meV). The potential difference induces the hybridization between MLG-like and BLG-like subbands and also shifts down in energy the top of the α band. **e-h**, The TMF spectra in TLG at $D = 0$, 0.18, 0.34, and 0.49 V/nm respectively. As D increases, the α band starts to disappear while the β band remains visibly unchanged.

6.5 TMF in bilayer graphene

We now turn to TMF in BLG. Figures 6.2b and e display TMF fans for BLG at 5 K. Evidently, the TMF spectra of MLG and BLG are very similar, even though their band structures are different (Fig. 6.2a-b, insets). The similarity arises from the fact that, when only the nearest intra-layer γ_0 and inter-layer γ_1 hopping parameters are considered, both MLG and BLG have circular Fermi surfaces, resulting in the same circular orbit and $\sqrt{n}$-dependence of k_{F}. The dashed lines in Fig. 6.2b are focusing fields calculated from Eq. 1. For this device, the calculated $B_{\mathrm{f}}^{(1)}$ for the first order peak are in good agreement with the measured data, but higher order modes show a discrepancy, similar to the MLG case. An additional possible source of mismatch in BLG, which does not exist in MLG, is trigonal warping [54] of the Fermi surface due to the next nearest neighbor inter-layer hopping term γ_3. This term transforms the BLG circular Fermi surface into a partly triangular surface, altering therefore the carrier's trajectory. Hence, in principle the values of B_{f} now depend on the crystallographic orientation with respect to the sample axis, and can vary by a few tens of mT (see supplementary information).

6.6 TMF in ABA trilayer graphene

Even though TMF cannot be used to differentiate MLG from BLG, the TMF spectrum of TLG is remarkably different because of the multiband character of its band structure. Figure 6.2c and f show TMF spectra of TLG at 5 K, measured at zero electric displacement field. Taking only γ_0 and γ_1 into account, the band structure of TLG consists of a massless MLG-like and a massive BLG-like subband at low energy (Fig. 6.2c, inset) [46, 96–99]. In a magnetic field, both subbands give rise to their own TMF spectra, with the

BLG-like subband having a larger $B_f^{(1)}$ due to its larger Fermi momentum (for a given E_F) . This allows us to identify the subband corresponding to each peak observed in the data. At high density, the peak from the MLG-like subband can be seen at ∼250 mT (Fig. 6.2c, orange dashed line, and small sharp peaks at low field in Fig. 6.2f) while the peaks from the BLG-like subband are visible from ∼250 mT onward (Fig. 6.2c, blue dashed lines). We do not observe higher order modes from the MLG-like subband, probably because they are masked by the much stronger peaks from the BLG-like subband, which contains most of the charge density.

Earlier studies have shown that higher order hopping parameters in TLG significantly modify its band structure [46, 96–99] by introducing subband overlap and trigonal warping in the BLG-like subband (Fig. 6.3a). We use this full parameter model for the TLG band structure to simulate the carrier trajectories and determine the focusing fields (see supplementary information). The results are shown as dashed lines in Fig 6.2c. Although we can reproduce the focusing field for the MLG-like subband very accurately, we obtain a mismatch in the BLG-like subband, similar to those above mentioned in MLG and BLG.

6.7 Ballistic electron spectroscopy

We now focus on the previously unexplored potential of TMF as a ballistic electron spectroscopy method to investigate in-situ changes in the band structure of a material. One of the remarkable properties of TLG is that its band structure can be tuned and controlled by using a transverse electric displacement field [116], D. TMF is sensitive to the occupation of each of the TLG subbands, enabling us to use TMF as a probe of the

change in the TLG band structure with D. Figures 6.3a and b show the band structure and Fermi surface of TLG at $n = -2 \times 10^{12}$ cm^{-2} for the case $D = 0$. We denote the valence bands of the MLG-like and BLG-like subbands as α and β bands, respectively. The application of a finite D induces a potential difference between the TLG layers, breaking the mirror symmetry and causing a hybridization between the MLG-like and BLG-like subbands. Figures 6.3c and d show how a finite D results in a shift down of the top of the α band . Consequently, for a fixed density, the Fermi momentum of the α band shrinks with D while that of the β band barely changes due to its much higher density of states.

Figures 6.3e-h show the TMF spectra of TLG at various D's. We observe a relatively strong focusing peak from the α band at $D = 0$ V/nm. However, as D increases, the peak starts to shift downward and it eventually disappears at low density. The disappearance of this peak is the result of the top of the α band shifting down in energy and leaving the β band as a lone contributor to the carrier density (Fig. 6.3c-d). Therefore, within our density range, we end up observing only a single focusing peak, from the β band, at high D. The onset in the density of the focusing peak of the α band allows us to determine the potential difference among the TLG layers as a function of applied D. As a result, we can estimate the effective dielectric constant of TLG which we find to be about 3.5 ± 0.2 (see supplementary information).

6.8 Temperature dependence of TMF spectra

We now look at the temperature dependence of the TMF spectra in MLG and BLG. The TMF spectrum is affected by temperature, T, at least in two ways: through the increase in dephasing (which smoothes the quantum interference fluctuations), and

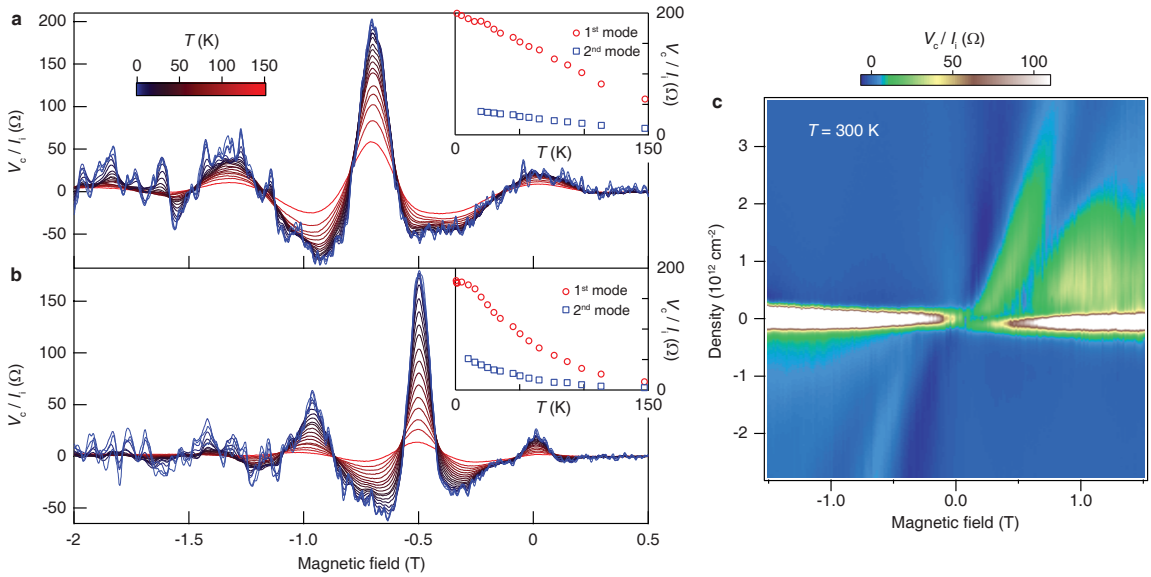

Figure 6.4: **Temperature dependence of the TMF in MLG and BLG. a-b** The TMF spectra as a function of temperature from 300 mK to 150 K for MLG and BLG, respectively, at $n = -2.8 \times 10^{12}$ cm^{-2}. Insets show the amplitudes of the first and second modes as a function of temperature (Data taken before current annealing). **c** transverse magnetic focusing in MLG at 300 K. The TMF peak as well as the $\sqrt{n}$ dependence of the focusing field can be clearly observed (Data taken after current annealing).

through the loss of ballistic transport due to new scattering channels activated at high T. Figures 6.4a and b show the TMF spectra of MLG and BLG, respectively, at $n = -2.8 \times 10^{12}$ cm^{-2} from 0.3 to 150 K. We first concentrate on the fine structure observed at low T (blue traces). This structure is the aforementioned quantum interference between different paths on which electrons propagate to the collector [128, 132–134]. When the temperature-induced broadening of the Fermi momentum is on the order of $1/L$, electrons become incoherent and the quantum interference is washed out [136], resulting in smooth focusing peaks. For our devices, this length corresponds to a temperature of about 15 K, which is in good agreement with the data.

In addition, the focusing peaks also decrease as T increases. The amplitudes of the first and second modes are shown in the insets of Fig. 6.4a and b for MLG and BLG, respectively. We observe that the focusing amplitude in MLG depends linearly on T. A potential scattering mechanism includes longitudinal acoustic phonons, which give rise to a linear temperature dependence of the scattering rate [137]. However, we observe a very different temperature dependence in BLG. The peak amplitude saturates at low temperature and decreases faster than in MLG at higher T. A similar temperature dependence of the focusing peaks has also been observed in InGaAs/InP heterojunctions [138]. Further theoretical work is needed to understand the temperature dependence of the focusing peaks as well as the difference between MLG and BLG.

6.9 Outlook

We end by commenting on the remarkable robustness of TMF in graphene. Fig. 6.4c shows the TMF fan of MLG at room temperature ($T = 300$ K), where the first

mode is clearly visible, indicating room temperature ballistic transport well into the micron regime. This lower bound temperature for the observation of TMF in graphene is at least three times higher than the highest temperature at which TMF spectrum has been observed in semiconductor heterostructures [138], the main reason probably being the lack of remote interfacial phonon scattering [139] from hBN. The ability to manipulate ballistic motion in graphene at room temperature, coupled with recent developments [140] in large area growth of graphene on hBN, paves the way towards novel applications based on electron-optics. On a more fundamental level, TMF may serve as a probe of electron-electron interaction [28, 29, 141] or strain-induced gauge field [10, 11, 37] effects in the electronic structure of graphene.

6.10 Methods

Figure 6.1c shows an atomic force microscopy image from one of our devices. Our devices are fabricated by transferring graphene onto high-quality hexagonal boron nitride [40]. We use oxygen plasma to etch graphene flakes into a Hall-bar geometry. Contacts are defined by electron-beam lithography and thermal evaporation of chromium and gold. The devices are then heat annealed in forming gas and subsequently current annealed in vacuum at low temperature [46]. We observe TMF peaks both before and after current annealing. The data after current annealing have higher quality than before current annealing, especially at low density, likely due to reduced charge density fluctuations. However, they exhibit similar quality at high density. All the data shown here are measured after current annealing, except Fig. 6.2d-e and Fig. 6.4a-b which was done before current annealing.

We identify the number of graphene layers by Raman spectroscopy and/or quantum Hall measurements. For TLG, the quantum Hall measurements reveal that it is Bernal-stacked [46]. In addition, we put a top gate onto the TLG device, using hBN as a thin dielectric. The combination of top gate (TG) and bottom gate (BG) allows us to control the charge density and the displacement field independently. We parameterize the displacement field by $D = (C_{\mathrm{TG}}V_{\mathrm{TG}} + C_{\mathrm{BG}}V_{\mathrm{BG}})/(2\epsilon_0)$ where C is the capacitive coupling, V is the applied gate voltage relative to the charge neutrality point, and ϵ_0 is the vacuum permittivity.

6.11 Supplementary information

6.11.1 Sources of discrepancy in focusing field

In MLG and BLG, we use the following formula

$$B_{\mathrm{f}}^{(p)} = \left(\frac{2\hbar k_{\mathrm{F}}}{eL}\right) p = \left(\frac{2\hbar\sqrt{\pi n}}{eL}\right) p \tag{6.2}$$

to calculate the focusing field with the assumption that the Fermi surface is circular. In this calculation, the density n and the distance L between injector and collector are determined from Hall resistance and AFM images respectively. We find however a discrepancy between the calculated and measured focusing fields (Fig. 6.2a-b). Here, we address some of the issues which could affect these parameters or assumption and consequently the value of the focusing field.

Finite width of injector and collector

Both injectors and collectors of our MLG and BLG devices have a finite width of $\sim$100 nm (Fig. 6.1a). Therefore, there is some uncertainty in L, of order 100 nm; L itself

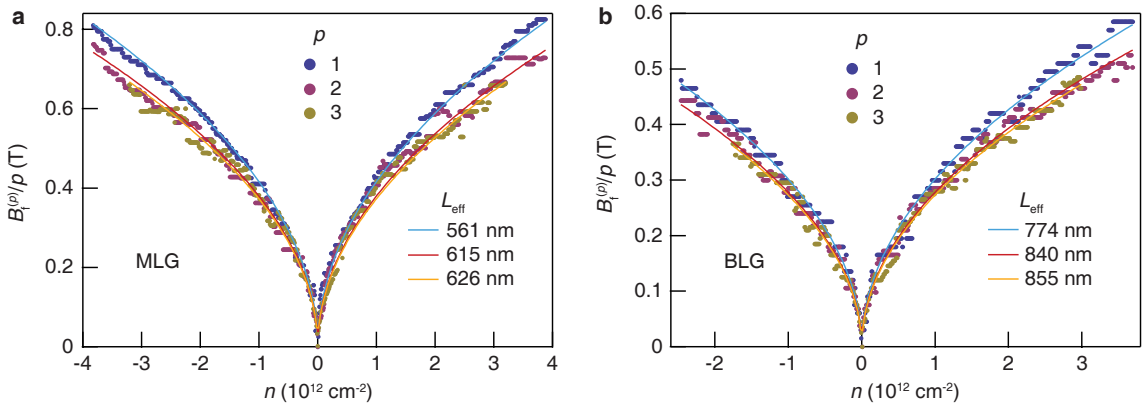

Figure 6.5: **Effective length between injector and collector. a-b,** Focusing fields normalized by the mode number as a function of density for MLG and BLG, respectively. Each solid line is the best fit to the data of each mode using Eq. 6.2.

is 500 nm for the MLG device and 775 nm for the BLG device. This uncertainty in L could change the effective distance and be partly responsible for the mismatch we observe. Below we determine the effective distance L_{eff} by fitting our TMF spectrum using Eq. 6.2 where this time we leave L as a fitting parameter.

Figure 6.5a and b show $B_{\text{f}}^{(p)}/p$ as a function of density for the first, second, and third modes ($p = 1$, 2, and 3 respectively). For a given density, the value of $B_{\text{f}}^{(p)}$ is determined from the position of magnetic field at which V_{c} is maximum locally. We find that the values of L_{eff} lie far from the expected values, except the first mode of BLG. For example, in MLG, we expect $L = 500$ nm but the fits yield 561, 615, and 626 nm for the first, second, and third modes, respectively. The values of L_{eff} for the second and third modes are actually larger than the maximum distance between the injector and collector. Even more surprising is the fact that the value of L_{eff} from the first mode is clearly smaller than those from the second and third modes for both MLG and BLG devices. This implies that the focusing peaks are not periodic in B, in contrast to Eq. 6.2. Such non-periodicity

cannot be explained by a finite width of the injector and collector. This and the fact that L_{eff} is much larger than the expected values lead us to believe that the finite width of the injector and collector is not the major factor in the quantitative discrepancy in the values of B_{f}.

Charge accumulation at the graphene edges

Due to the finite width of our graphene devices, compared to the SiO_2 thickness, the charge-density distribution induced by the back gate is no longer uniform across the graphene [135]. Electrostatically, charges tend to pile up at the edges. Such non-uniformity in density together with the small density of states in graphene lead to an electrostatic potential variation near the edges, altering the electron trajectories. Since the length (x-axis) of our graphene flakes is much longer than its width (y-axis), we can assume that the density depends on y only. Silvestrov and Efetov have shown that, up to the first order approximation, the potential variation relative to the Fermi energy due to the charge accumulation in MLG is given by [135]

$$E_{\text{F}} - U(y) = \hbar v_{\text{F}} \sqrt{\pi n(y)} = \hbar v_{\text{F}} \sqrt{n_{\text{avg}} W} \left[(W/2)^2 - (y - W/2)^2 \right]^{-1/4} \tag{6.3}$$

where n_{avg} is the average density and W is the graphene width. The electron's trajectory then follows a constant energy contour, yielding the following equation [142]

$$\frac{\mathrm{d}\, y}{\mathrm{d}x} = \frac{\sqrt{(E_{\text{F}} - U(y))^2 - v_{\text{F}}^2 (p_x - eBy)^2}}{v_{\text{F}}(p_x - eBy)}. \tag{6.4}$$

To avoid the singularity at the edges, we set the density to a constant when the distance is within 10 nm from the injector. We note that any sensible choice of the cutoff does not affect the caustic.

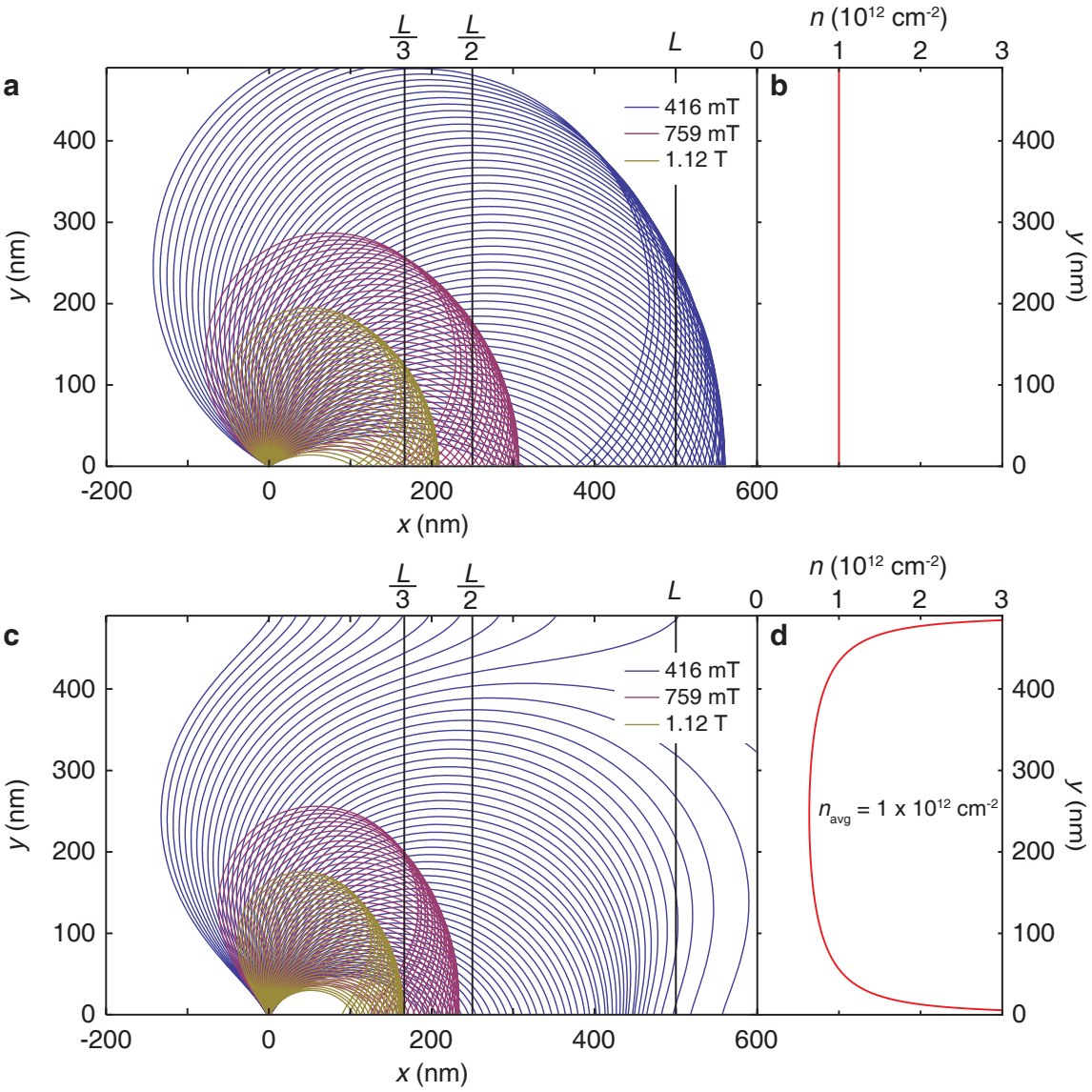

Figure 6.6: **Effect of charge accumulation on the electron trajectories. a,** Electron trajectories in the case of constant density distribution of 1×10^{12} cm^{-2} at $B = 416$ mT (blue lines), 759 mT (purple lines), and 1.12 T (yellow lines). These magnetic fields are obtained from the data for the first, second, and third modes. **b,** Density as a function of y (graphene's width) which we use to simulate the trajectories in **a**. **c,** Electron trajectories when we take charge accumulation at the edges into account. **d,** Density as a function of y which we use to simulate the trajectories in **c**. The average density is 1×10^{12} cm^{-2}.

Figure 6.6a and c show electron trajectories simulated from Eq. 6.4 for the cases of uniform charge density distribution and charge accumulation near the edges, respectively. The magnetic fields we used in these simulations are taken from the data in Fig. 6.2a where the focusing fields for the first, second, and third modes are 416 mT, 759 mT, and 1.12 T at $n = 1 \times 10^{12}$ cm^{-2}. Theoretically, at the focusing field of mode p, the caustic has to reflect off the edge at $x = L/p$. However, for the uniform density distribution, the simulation shows that the caustics meet the edge at least ∼50 nm further than the expected positions (Fig. 6.6a). Moreover, with the uniform density distribution, the focusing fields is periodic in B, contradictory to the data.

As we introduce the charge accumulation, the variation in potential acts as an in-plane electric field, pulling electrons to the edges. As a result, electrons reach the edge faster and at a shorter distance as shown in Fig. 6.6c. The positions at which the caustics meet the edge are now closer to the expected values of L/p. In addition, a non-uniform charge distribution also explains the non-periodicity of the focusing fields. For the higher order modes, the electron trajectories are closer to the edge and hence subjected to a stronger electric field owing to a faster potential variation. Therefore, a smaller magnetic field is required to focus electrons at the same distance. We observe that $B_{\mathrm{f}}^{(1)}$ is significantly higher than $B_{\mathrm{f}}^{(2)}/2$ but $B_{\mathrm{f}}^{(2)}/2$ and $B_{\mathrm{f}}^{(3)}/3$ have very similar values (Fig. 6.5a-b). This may be an indication of the expected break down of the singularity at the edges [135] which causes both of these modes to experience a similar electric field.

We also note that Eq. 6.4 does imply the $\sqrt{n}$-dependence of the focusing field. One way to determine the density dependence of the focusing field is to require $\mathrm{d}y/\mathrm{d}x$ to be invariant as we vary density in order to keep the electron's trajectory and the focal point unchanged. Since both $E_{\mathrm{F}} - U(y)$ and p_x are proportional to $\sqrt{n_{\mathrm{avg}}}$, this imposes

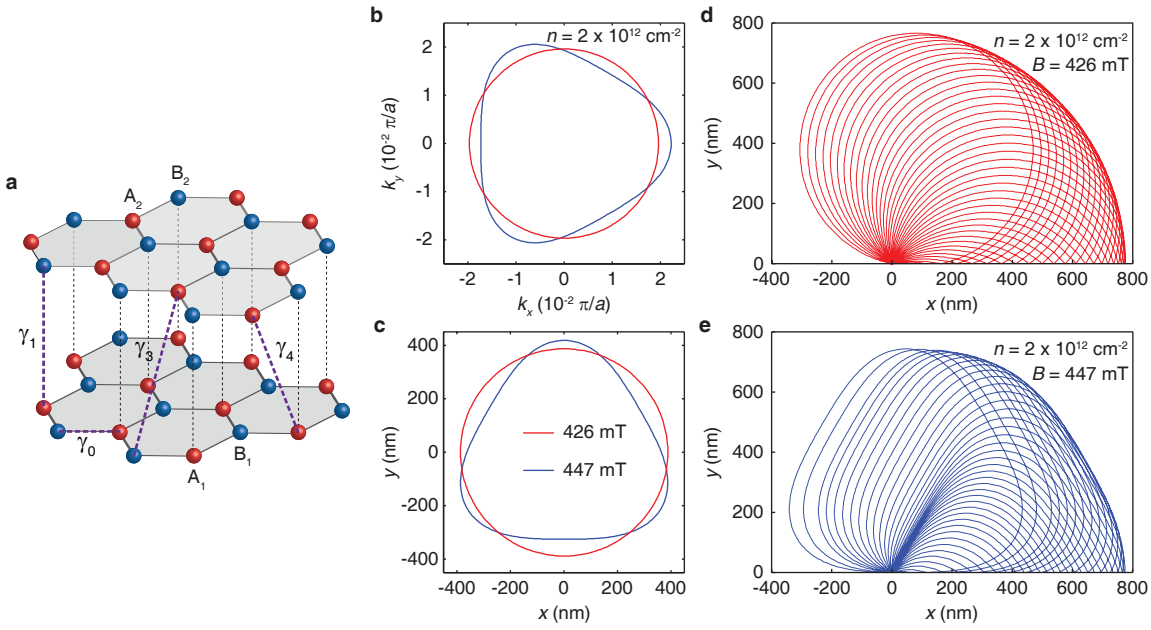

Figure 6.7: **Trigonal warping effect on BLG. a,** The crystal structure of BLG. The unit cell consists of four atoms, A_1 and B_1 from the bottom layer and A_2 and B_2 from the top layer. The hopping parameters between different sublattices are shown. **b,** Fermi surfaces of BLG for $\gamma_3 = 0$ eV and $\gamma_4 = 0$ eV (red line) and $\gamma_3 = 0.315$ eV and $\gamma_4 = 0.15$ eV (blue line) at $n = 2 \times 10^{12}$ cm^{-2}. **c,** Electron trajectories in real space for the corresponding Fermi surfaces in **b** of the same color. The magnetic fields are chosen such that the focal point is at 775 nm. **d-e,** Electron trajectories when they are injected isotropically at the origin for $\gamma_3 = 0$ eV and $\gamma_3 = 0.315$ eV, respectively, both for $n = 2 \times 10^{12}$ cm^{-2}.

B to be proportional to $\sqrt{n_{\text{avg}}}$ as well so that the ratio on the right hand side of Eq. 6.4 stays constant.

Trigonal warping

The Fermi surface in BLG is circular only if γ_0 and γ_1 are considered. However, when we take γ_3, which is the hopping parameter between B_1 and A_2 (Fig. 6.7a), into account, it introduces a trigonal warping effect to the band structure, transforming the Fermi surface from a circle to a triangular structure. Figure 6.7b shows Fermi surfaces

from a simple model (red line) and full-parameter model (blue line) at $n = 2 \times 10^{12}$ cm^{-2}, calculated from the following Hamiltonian

$$H_{\mathrm{BLG}} = \begin{bmatrix} 0 & v_3\pi & -v_4\pi^\dagger & v_0\pi^\dagger \\ v_3\pi^\dagger & 0 & v_0\pi & -v_4\pi \\ -v_4\pi & v_0\pi^\dagger & 0 & \gamma_1 \\ v_0\pi & -v_4\pi^\dagger & \gamma_1 & 0 \end{bmatrix}. \tag{6.5}$$

where $v_i = (\sqrt{3}/2)a\gamma_i/\hbar$ and $\pi = \hbar(k_x + ik_y)$. Here, we use $\gamma_0 = 3.1$ eV, $\gamma_1 = 0.39$ eV, $\gamma_3 = 0.315$ eV, and $\gamma_4 = 0.15$ eV [49]. We note that γ_4 induces electron-hole asymmetry to the band structure but does not affect the shape of Fermi surface in a significant way. To obtain the electron trajectory in real space, we apply the semiclassical equation of motion

$$\hbar \frac{\mathrm{d}}{\mathrm{d}t}\boldsymbol{k} = (-e)\frac{\mathrm{d}}{\mathrm{d}t}\boldsymbol{r} \times \boldsymbol{B}. \tag{6.6}$$

The equation 6.6 implies that, for a constant transverse B-field, the electron trajectory in real space can be obtained by rotating its Fermi surface by 90° and scaling it by a factor $\hbar/(eB)$ [127]. Figure 6.7c shows electron trajectories corresponding to the Fermi surfaces shown in Fig. 6.7b.

To determine the position of the caustic, we simulate a set of electron trajectories, assuming that electrons are injected isotropically from the origin. Figure 6.7d and e show such simulations at $n = 2 \times 10^{12}$ cm^{-2} for a simple model and full-parameter model, respectively. The magnetic fields is chosen such that the caustic encounters the x-axis at $x = 775$ nm which is the distance between the injector and the collector in our BLG device. We find that the focusing fields for the simple and full-parameter models are 426 mT and 447 mT, respectively.

The trigonal warping not only affects the value of the focusing field but it also

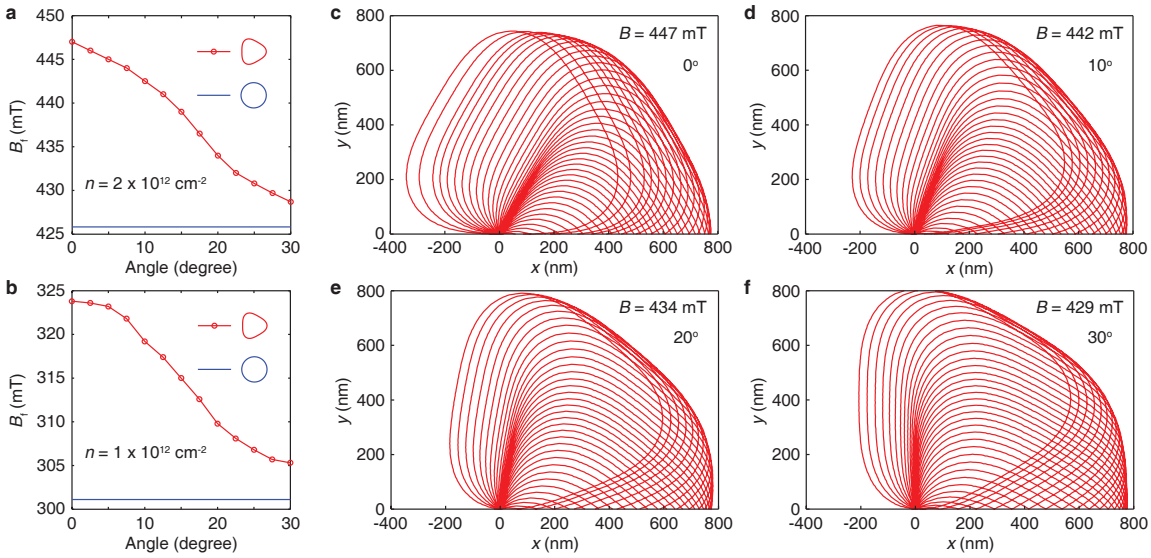

Figure 6.8: **The dependence of focusing fields on crystallographic orientation. a-b,** Focusing fields for the first mode as a function of a crystallographic orientation for $n = 2 \times 10^{12}$ cm^{-2} and $n = 1 \times 10^{12}$ cm^{-2}, respectively, for $\gamma_3 = 0$ eV and $\gamma_4 = 0$ eV (blue line), and $\gamma_3 = 0.315$ eV and $\gamma_4 = 0.15$ eV (red line). **c-f,** Electron trajectories when the angle between the BLG crystallographic orientation and the BLG edge is 0°, 10°, 20°, and 30° respectively.

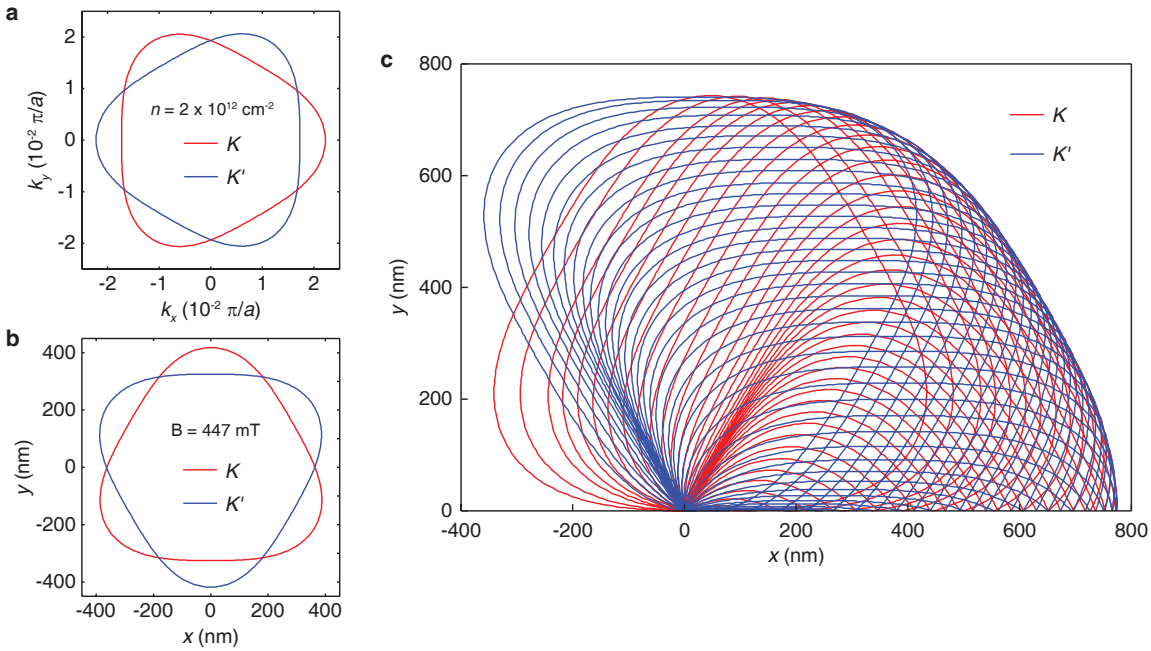

Figure 6.9: **Valley degeneracy in TMF. a,** Fermi surfaces at the K (red line) and K' (blue line) valleys for $n = 2 \times 10^{12}$ cm^{-2}. **b,** Electron trajectories in real space for the corresponding Fermi surfaces in **a** of the same color at $B = 447$ mT. **c,** Comparison between electron's trajectories at the K (red line) and K' (blue line) valleys. The focal point is evidently the same.

introduces an anisotropy to the band structure which causes the focusing field to depend on crystallographic orientation. Figure 6.8a and b show the focusing field as a function of crystal orientation at $n = 2 \times 10^{12}$ cm^{-2} and $n = 1 \times 10^{12}$ cm^{-2} respectively. We observe that the value of the focusing fields for the full-parameter model for any orientation is always larger than that of the simple model by about 5-20 mT. These numbers are similar to the mismatch between the focusing fields we measure in our data and those from the simple model. However, the measured focusing fields are smaller than the focusing field calculated from the simple model, while those calculated from the full-parameter model are larger. Therefore, trigonal warping cannot be the only source of the mismatch.

We also note that another consequence of trigonal warping is that the Fermi surfaces at the K and K' valleys are different. They are in fact the inverse of each other (Fig. 6.9a). Hence, electrons from these two valleys follow different paths under the magnetic field (Fig. 6.9b). However, their caustics line up exactly which prevents us from using the TMF to probe the distinct trajectories for the K and K' valleys (Fig. 6.9c).

6.11.2 Calculation of focusing fields and effective dielectric constant in TLG

In order to calculate focusing fields in TLG, we need to determine the Fermi surface of each band for a given Fermi energy. We use the following Hamiltonian to calculate the Fermi surface [116]

$$H = \begin{bmatrix} H_m & \Gamma \\ \Gamma^\dagger & H_b \end{bmatrix}, \tag{6.7}$$

where

$$\Gamma = \begin{bmatrix} \Delta_1 & 0 & 0 & 0 \\ 0 & 0 & 0 & \Delta_1 \end{bmatrix}, \quad H_m = \begin{bmatrix} \Delta_2 - \gamma_2/2 & v_0\pi^\dagger \\ v_0\pi & \Delta_2 - \gamma_5/2 + \delta \end{bmatrix},$$

$$H_b = \begin{bmatrix} \Delta_2 + \gamma_2/2 & \sqrt{2}v_3\pi & -\sqrt{2}v_4\pi^\dagger & v_0\pi^\dagger \\ \sqrt{2}v_3\pi^\dagger & -2\Delta_2 & v_0\pi & -\sqrt{2}v_4\pi \\ -\sqrt{2}v_4\pi & v_0\pi^\dagger & -2\Delta_2 + \delta & \sqrt{2}\gamma_1 \\ v_0\pi & -\sqrt{2}v_4\pi^\dagger & \sqrt{2}\gamma_1 & \Delta_2 + \gamma_5/2 + \delta \end{bmatrix}.$$

with $\gamma_0 = 3.1$, $\gamma_1 = 0.39$, $\gamma_2 = -0.028$, $\gamma_3 = 0.315$, $\gamma_4 = 0.041$, $\gamma_5 = 0.05$, and $\delta = 0.046$ eV [46]. The parameters $\Delta_1 = (U_1 - U_3)/2$ and $\Delta_2 = (U_1 - 2U_2 + U_3)/3$ describe

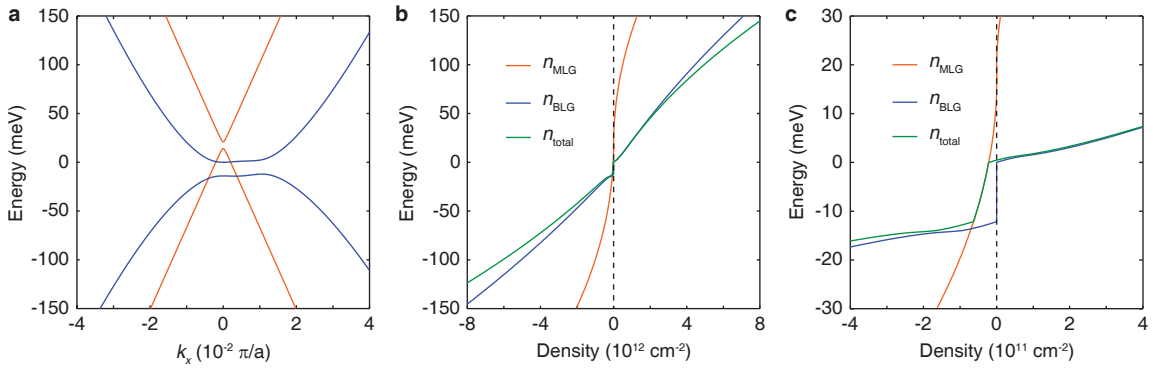

Figure 6.10: **Contribution of each band to the total density. a,** Band structure of TLG at zero displacement field. **b,** Density of MLG-like subband (orange line), density of BLG-like subband (blue line), and total density (green line) as a function of energy. **c,** Zoom-in plot of **b** showing the hole pocket of the MLG-like subband when the total density is positive.

the energy difference between layers where U_i is the potential of layer i. Figure 3b and d show Fermi surfaces calculated from such Hamiltonian for $\Delta_1 = 0$ meV and $\Delta_1 = 30$ meV, respectively, for the case $\Delta_2 = 0$ meV.

Once we obtain these Fermi surfaces, we simulate the electron trajectories in real space similar to Fig. 6.7e. We vary the magnetic field until the caustic meets the x-axis at $L = 950$ nm, which is the distance between injector and collector in our TLG device. Finally, we have to convert the Fermi energy into a total density, which is the quantity we control in the transport measurement, by calculating the area of the corresponding Fermi surface

$$n_{\text{total}} = 4\int_{(\text{MLG})} \frac{\mathrm{d}k_x \mathrm{d}k_y}{(2\pi)^2} + 4\int_{(\text{BLG})} \frac{\mathrm{d}k_x \mathrm{d}k_y}{(2\pi)^2}. \tag{6.8}$$

where (MLG) and (BLG) refer to the MLG-like and BLG-like subbands, and the factor 4 is due to spin and valley degeneracies.

Figure 6.10b shows the total density and the densities of the MLG-like and BLG-

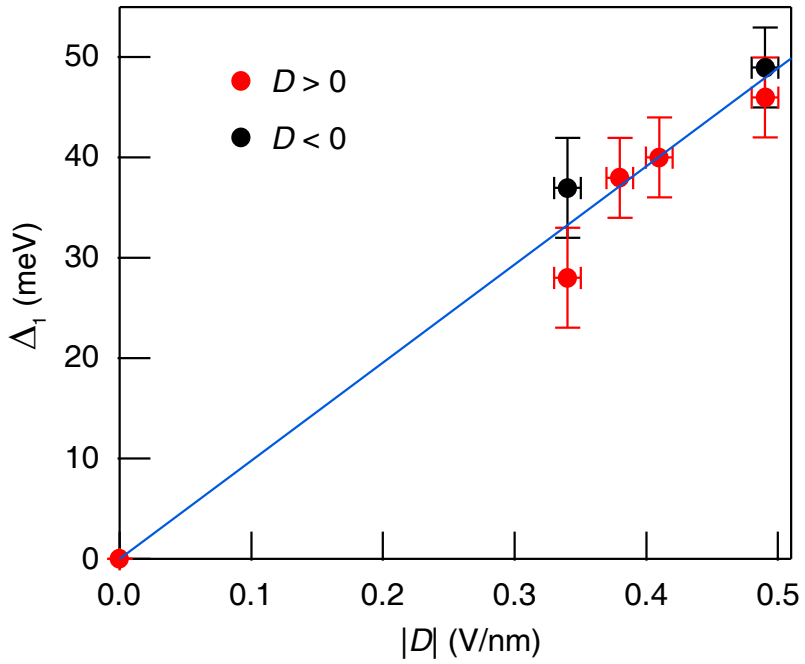

Figure 6.11: **Screening in TLG.** Δ_1 as a function of $|D|$ for TLG. The black (red) dots are data from negative (positive) D's, and the Δ_1's are determined from the bottom (top) of the conduction (valence) band of the MLG-like subband.

like subbands as a function of energy. Due to the band overlap (Fig. 6.10a), there is a hole pocket from the MLG-like subband when the total density is positive. Such overlap causes the focusing field from the valence band of the MLG-like subband to cross the zero density line at a slightly negative value instead of zero, in agreement with our measurements (Fig. 6.3e).

The correspondence between density and energy allows us to investigate screening in TLG. Under an applied displacement field, the conduction band and valence band of the MLG-like subband will shift up and down in energy, respectively (Fig. 6.3a and c). As a result, the onset of the focusing peak of the MLG-like subband in the TMF spectrum will shift in density (Fig. 6.3e-h). Therefore, we use this onset density to determine the

potential difference between adjacent layers Δ_1 by repeating the procedure described above for various values of Δ_1. Figure 6.11 shows Δ_1 as a function of the applied displacement field D. Assuming a linear response, we fit the data to $\Delta_1 = dD/\epsilon_{\mathrm{TLG}}$, where $d = 0.34$ nm is the distance between two adjacent layers and ϵ_{TLG} is the effective dielectric constant. We obtain $\epsilon_{\mathrm{TLG}} = 3.5 \pm 0.2$, comparable to bilayer graphene [76] and twisted bilayer graphene [143].

6.11.3 Specularity

The ability to control the density in graphene allows us to investigate the amplitudes of the focusing peaks and specularity as a function of density. Figure 6.12 shows the amplitudes of the first and second focusing peaks as a function of density for MLG, BLG, and TLG. Small fluctuations are the result of the quantum interference between different trajectories. Around the charge neutrality points, the focusing peaks disappear owing to electron-hole puddles causing trajectories to deflect as electrons move from one puddle to another [43, 44]. As we increase the density, the effect from charged impurities is screened and the density becomes more uniform across the sample. Hence, the focusing peaks emerge at finite density.

Theoretically, the value of the amplitude $V_{\mathrm{c}}/I_{\mathrm{i}}$ is inversely proportional to $\sqrt{n}$ [128], neglecting quantum interference and disorder. However, we only observe this $1/\sqrt{n}$-dependence in the electron regime of our MLG device which has the highest quality among the samples we measure (Fig. 6.12a). This deviation from the theoretical prediction is likely due to impurities, causing small angle scattering which could reduce the number of electrons reaching a collector but still preserves the focusing [133].

One important information we can deduce from the amplitudes is the specularity

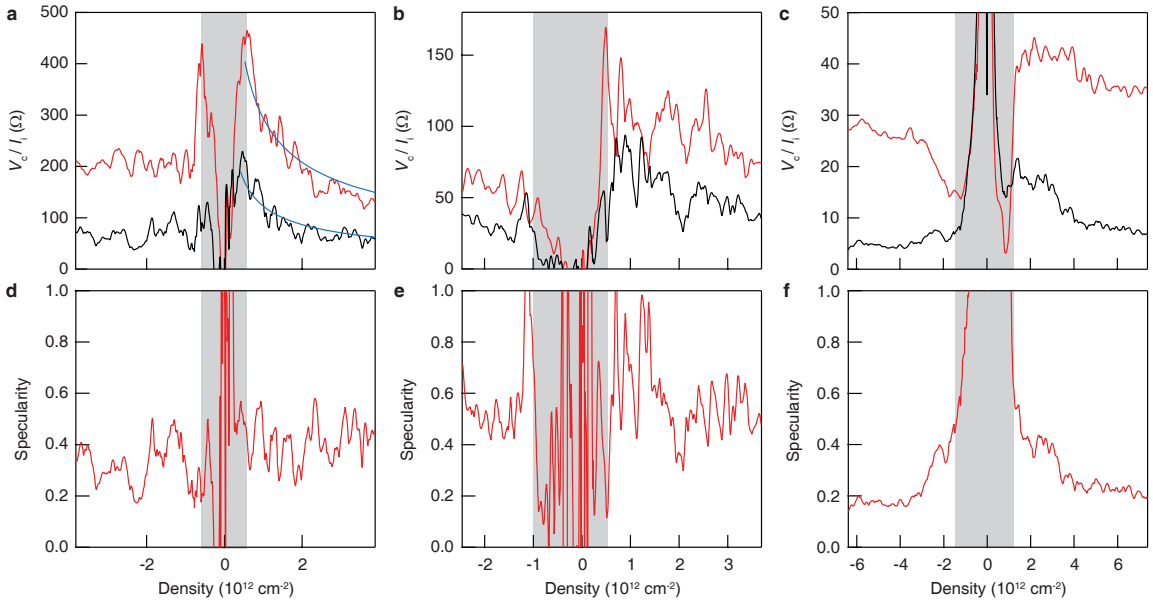

Figure 6.12: **Density dependence of the focusing peak amplitudes. a-c,** Amplitudes of the first (red) and second (black) focusing peaks as a function of density for MLG, BLG, and TLG, respectively determined from Fig. 6.2a-c. The blue lines in **a** are a fit to the data with the function $c/\sqrt{n}$ where c is a constant. **d-f,** Measured specularity as a function of density for MLG, BLG, and TLG respectively. The shaded regions are the density range where disorder dominates the focusing signals.

Table 6.1: Measured specularity in our MLG, BLG, and TLG devices for electron and hole regimes

	electron	hole
MLG	0.4 ± 0.1	0.3 ± 0.1
BLG	0.5 ± 0.1	0.5 ± 0.1
TLG	0.23 ± 0.03	0.18 ± 0.02

q which measures the probability of specular reflection off a graphene edge. The value of the specularity can be calculated from the ratio between the amplitudes from adjacent peaks. Here, we will refer to this ratio as the measured specularity q_m. In our case, we use the ratio between the second and the first peaks. We neglect the third peak because its amplitude is small and largely dominated by the interference pattern.

In order to discuss the specularity, we restrict ourselves to high density (outside the shaded regions in Fig. 6.12), to minimize electron-hole puddle influence. We find that the specularity is weakly dependent on density and it saturates at high density (Fig. 6.12) with its values ranging from 0.2 to 0.5 (see Table 6.1). However, Rakyta *et al.* have calculated the transmission probability for TMF in graphene with armchair, zigzag, or reconstructed zigzag edges and found that the transmission probability should increase with increasing magnetic field. This disagreement should not be surprising because our graphene edges are defined by electron beam lithography and oxygen plasma etching (Fig. 6.1a). Its edge structure will be ill-defined and will be much rougher at atomic scale than those used in the theoretical study. In this regard, we note that a recent experimental study on boundary scattering in ballistic graphene found a nearly zero probability of specular reflection on samples with oxygen plasma etching defined edges [144].

We point out that, in semiconductor heterostructures, the amplitude of the focusing peaks increases with increasing B for electrostatically defined edges but it decreases with increasing B for edges defined by focused ion beam (a procedure similar to our oxygen plasma etching) [127, 128]. It would be interesting to see the behavior of the focusing peaks in graphene with natural edges (those occurring from the exfoliation process, without oxygen plasma etching).

The details of the impurity-induced potential profile through which electrons prop-

agate could also play a crucial role in the measured specularity. For instance, if a single charged impurity were to sit right at the top of the first-mode trajectory which is far away from the second-mode, this impurity could affect the amplitude of the first peak significantly but hardly affect that of the second peak. One evidence which supports this claim is that, in our BLG sample, before current annealing, we observed that the amplitude from the second focusing peak was higher than that of the first focusing peak. However, after current annealing, the first peak became larger (Fig. 6.2b). The effect of current annealing is likely to only reduce the potential inhomogeneity in the sample by eliminating impurities but not strong enough to restructure the graphene's edge. Therefore, the change in the measured specularity before and after current annealing is conceivably due to the change in potential profile.

6.11.4 Visibility of Shubnikov–de Haas oscillations

In Fig. 6.1e, the SdHOs in quadrants 1 and 3 are dominated by a speckle-like feature. This feature is an interference of different trajectories of electrons propagating coherently to the collector [128,132–134]. The interference pattern does not exist in quadrants 2 and 4 because, in these configurations, electrons propagate from the injector (contact i) to contact g away from the collector (Fig. 6.1c). Contact g now acts as an injector for the voltage probes (contacts f and c). Since its size is much larger than the Fermi wavelength, contact g does not act as a coherent source for injected electrons and the interference pattern is diminished [145]. Moreover, electrons have to travel at a much longer distance before reaching the voltage probes which increases the chance of dephasing from scattering.

Bibliography

[1] Wallace, P. R. The band theory of graphite. *Phys. Rev.* **71**, 622–634 (1947).

[2] Mermin, N. D. Crystalline order in two dimensions. *Phys. Rev.* **176**, 250–254 (1968).

[3] Novoselov, K. S. *et al.* Electric field effect in atomically thin carbon films. *Science* **306**, 666–669 (2004).

[4] Novoselov, K. S. *et al.* Two-dimensional gas of massless Dirac fermions in graphene. *Nature* **438**, 197–200 (2005).

[5] Zhang, Y., Tan, Y.-W., Stormer, H. L. & Kim, P. Experimental observation of the quantum Hall effect and Berry's phase in graphene. *Nature* **438**, 201–204 (2005).

[6] Williams, J. R., DiCarlo, L. & Marcus, C. M. Quantum Hall effect in a gate-controlled p-n junction of graphene. *Science* **317**, 638–641 (2007).

[7] Özyilmaz, B. *et al.* Electronic transport and quantum Hall effect in bipolar graphene p-n-p junctions. *Phys. Rev. Lett.* **99**, 166804 (2007).

[8] Young, A. F. & Kim, P. Quantum interference and klein tunneling in graphene heterojunctions. *Nature Phys.* **5**, 222–226 (2009).

[9] Stander, N., Huard, B. & Goldhaber-Gordon, D. Evidence for klein tunneling in graphene *p-n* junctions. *Phys. Rev. Lett.* **102**, 026807 (2009).

[10] Levy, N. *et al.* Strain-induced pseudo-magnetic fields greater than 300 tesla in graphene nanobubbles. *Science* **329**, 544–547 (2010).

[11] Gomes, K. K., Mar, W., Ko, W., Guinea, F. & Manoharan, H. C. Designer Dirac fermions and topological phases in molecular graphene. *Nature* **483**, 306–310 (2012).

[12] Lee, C., Wei, X., Kysar, J. W. & Hone, J. Measurement of the elastic properties and intrinsic strength of monolayer graphene. *Sceince* **321**, 385–388 (2008).

[13] Bunch, J. S. *et al.* Impermeable atomic membranes from grahene sheets. *Nano Lett.* **8**, 2458–2462 (2008).

[14] Nair, R. R. *et al.* Fine structure constant defined visual transparency of graphene. *science* **320**, 1308 (2008).

[15] Elias, D. C. *et al.* Control of graphene's properties by reversible hydrogenation: Evidence for graphene. *Science* **323**, 610–613 (2009).

[16] Robinson, J. T. *et al.* Properties of fluorinated graphene films. *Nano Lett.* **10**, 3001–3005 (2010).

[17] Cheng, S.-H. *et al.* Reversible fluorination of graphene: Evidence of a two-dimensional wide bandgap semiconductor. *Phys. Rev. B* **81**, 205435 (2010).

[18] Martin, J. *et al.* Observation of electron-hole puddles in graphene using a scanning single-electron transistor. *Nature Phys.* **4**, 144–148 (2008).

[19] Chen, J.-H. *et al.* Charged-impurity scattering in graphene. *Nature Phys.* **4**, 377–381 (2008).

[20] Chen, J.-H., Jang, C., Xiao, S., Ishigami, M. & Fuhrer, M. S. Intrinsic and extrinsic performance limits of graphene devices on SiO_2. *Nature Nanotech.* **3**, 206–209 (2008).

[21] Zhang, Y., Brar, V. W., Girit, C., Zettl, A. & Crommie, M. F. Origin of spatial charge inhomogeneity in graphene. *Nature Phys.* **5**, 722–726 (2009).

[22] Du, X., Skachko, I., Barker, A. & Andrei, E. Y. Approaching ballistic transport in suspended graphene. *Nature Nanotech.* **3**, 491–495 (2008).

[23] Bolotin, K. I. *et al.* Ultrahigh electron mobility in suspended graphene. *Solid State Commun.* **146**, 351 (2008).

[24] Elias, D. C. *et al.* Dirac cones reshaped by interaction effects in suspended graphene. *Nature Phys.* **7**, 701–704 (2011).

[25] Du, X., Skachko, I., Duerr, F., Luican, A. & Andrei, E. Y. Fractional quantum Hall effect and insulating phase of Dirac electrons in graphene. *Nature* **462**, 192–195 (2009).

[26] Bolotin, K. I., Ghahari, F., Shulman, M. D., Stormer, H. L. & Kim, P. Observation of the fractional quantum Hall effect in graphene. *Nature* **462**, 196–199 (2009).

[27] Feldman, B. E., Martin, J. & Yacoby, A. Broken-symmetry states and divergent resistance in suspended bilayer graphene. *Nature Phys.* **5**, 889–893 (2009).

[28] Weitz, R. T., Allen, M. T., Feldman, B. E., Martin, J. & Yacoby, A. Broken-symmetry states in doubly gated suspended bilayer graphene. *Science* **330**, 812–816 (2010).

[29] Mayorov, A. S. *et al.* Interaction-drive spectrum reconstruction in bilayer graphene. *Science* **333**, 860–863 (2011).

[30] Jr, J. V. *et al.* Transport spectroscopy of symmetry-broken insulating states in bilayer graphene. *Nature Nanotech.* **7**, 156–160 (2012).

[31] Freitag, F., Trbovic, J., Weiss, M. & Schönenberger, C. Spontaneously gapped ground state in suspended bilayer graphene. *Phys. Rev. Lett.* **108**, 076602 (2012).

[32] Meyer, J. C. *et al.* The structure of suspended graphene sheets. *Nature* **446**, 60–63 (2007).

[33] Bao, W. *et al.* Controlled ripple texturing of suspended graphene and ultrathin graphite membranes. *Nature Nanotech.* **4**, 562–566 (2009).

[34] Chen, C. *et al.* Performance of monolayer graphene nanomechanical resonators with electrical readout. *Nature Nanontech.* **4**, 861–867 (2009).

[35] Pereira, V. M. & Castro Neto, A. H. Strain engineering of graphene's electronic structure. *Phys. Rev. Lett.* **103**, 046801 (2009).

[36] Fogler, M. M., Guinea, F. & Katsnelson, M. I. Pseudomagnetic fields and ballistic transport in a suspended graphene sheet. *Phys. Rev. Lett.* **101**, 226804 (2008).

[37] Guinea, F., Katsnelson, M. I. & Geim, A. K. Energy gaps and a zero-field quantum Hall effect in graphene by strain engineering. *Nature Phys.* **6**, 30–33 (2010).

[38] Lui, C. H., Liu, L., Mak, K. F., Flynn, G. W. & Heinz, T. F. Ultraflat graphene. *Nature* **462**, 339–341 (2009).

[39] Shim, J. *et al.* Water-gated charge doping of graphene induced by mica substrates. *Nano Lett.* **12**, 648–654 (2012).

[40] Dean, C. R. *et al.* Boron nitride substrates for high-quality graphene electronics. *Nature Nanotech.* **5**, 722–726 (2010).

[41] Liu, L., Feng, Y. P. & Shen, Z. X. Structural and electronic properties of h-bn. *Phys. Rev. B* **68**, 104102 (2003).

[42] Watanabe, K., Taniguchi, T. & Kanda, H. Direct-bandgap properties and evidence for ultraviolet lasing of hexagonal boron nitride single crystal. *Nature Mater.* **3**, 404–409 (2004).

[43] Xue, J. *et al.* Scanning tunnelling microscopy and spectroscopy of ultra-flat graphene on hexagonal boron nitride. *Nature Mater.* **10**, 282–285 (2011).

[44] Decker, R. *et al.* Local electronic properties of graphene on a BN substrate via scanning tunneling microscopy. *Nano Lett.* **11**, 2291–2295 (2011).

[45] Dean, C. R. *et al.* Multicomponent fractional quantum Hall effect in graphene. *Nature Phys.* **7**, 693–696 (2011).

[46] Taychatanapat, T., Watanabe, K., Taniguchi, T. & Jarillo-Herrero, P. Quantum Hall effect and Landau-level crossing of Dirac fermions in trilayer graphene. *Nature Phys.* **7**, 621–625 (2011).

[47] Mayorov, A. S. *et al.* Micrometer-scale ballistic transport in encapsulated graphene at room temperature. *Nano Lett.* **11**, 2396–2399 (2011).

[48] Zomer, P. J., Dash, S. P., Tombros, N. & van Wees, B. J. A transfer technique for high mobility graphene devices on commercially available hexagonal boron nitride. *Appl. Phys. Lett.* **99**, 232104 (2011).

[49] Zhang, L. M. *et al.* Determination of the electronic structure of bilayer graphene from infrared spectroscopy. *Phys. Rev. B* **78**, 235408 (2008).

[50] Castro, E. V. *et al.* Electronic properties of a biased graphene bilayer. *J. Phys.: Condens. Matter* **22**, 175503 (2010).

[51] Ohta, T., Bostwick, A., Seyller, T., Horn, K. & Rotenberg, E. Controlling the electronic structure of bilayer graphene. *Science* **313**, 951–954 (2006).

[52] Oostinga, J. B., Heersche, H. B., Liu, X., Morpurgo, A. F. & Vandersypen, L. M. K. Gate-induced insulating state in bilayer graphene devices. *Nature Mater.* **7**, 151–157 (2008).

[53] Efetov, D. K., Maher, P., Glinskis, S. & Kim, P. Multiband transport in bilayer graphene at high carrier densities. *Phys. Rev. B* **84**, 161412 (2011).

[54] McCann, E. & Fal'ko, V. I. Landau-level degeneracy and quantum Hall effect in a graphite bilayer. *Phys. Rev. Lett.* **96**, 086805 (2006).

[55] Guinea, F., Castro Neto, A. H. & Peres, N. M. R. Electronic states and Landau levels in graphene stacks. *Phys. Rev. B* **73**, 245426 (2006).

[56] Martin, J. *et al.* Observation of electron-hole puddles in graphene using a scanning single-electron transistor. *Nature Phys.* **4**, 144–148 (2008).

[57] McCann, E. & Koshino, M. The electronic properties of bilayer graphene. ArXiv:1205.6953.

[58] Dresselhaus, M. S. & Dresselhaus, G. Intercalation compounds of graphite. *Adv. Phys.* **51**, 1–186 (2002).

[59] Lui, C. H. *et al.* Imaging stacking order in few-layer graphene. *Nano. Lettl* **11**, 164–169 (2011).

[60] Koshino, M. & McCann, E. Parity and valley degeneracy in multilayer graphene. *Phys. Rev. B* **81**, 115315 (2010).

[61] Koshino, M. & McCann, E. Trigonal warping and Berry's phase Nπ in ABC-stacked multilayer graphene. *Phys. Rev. B* **80**, 165409 (2009).

[62] Lui, C. H., Li, Z., Mak, K. F., Cappelluti, E. & Heinz, T. F. Observation of an electrically tunable band gap in trilayer graphene. *Nature Phys.* **7**, 944–947 (2011).

[63] Jhang, S. H. *et al.* Stacking-order dependent transport properties of trilayer graphene. *Phys. Rev. B* **84**, 161408 (2011).

[64] Yankowitz, M. *et al.* Emergence of superlattice Dirac points in graphene on hexagonal boron nitride. *Nature Phys.* **8**, 382–386 (2012).

[65] Dean, C. R. *et al.* Hofstadter's butterfly in moire superlattices: A fractal quantum Hall effect. ArXiv:1212.4783.

[66] Ponomarenko, L. A. *et al.* Changes in fermi surface topology and hofstadter quantization in graphene superlattices. ArXiv:1212.5012.

[67] Klitzing, K. v., Dorda, G. & Pepper, M. New method for high-accuracy determination of the fine-structure constant based on quantized Hall resistance. *Phys. Rev. Lett.* **45**, 494–497 (1980).

[68] Abanin, D. A., Lee, P. A. & Levitov, L. S. Charge and spin transport at the quantum Hall edge of graphene. *Solid State Comm.* **143**, 77–85 (2007).

[69] Datta, S. *Electronic Transport in Mesoscopic Systems* (Cambridge University Press, 1997).

[70] McCann, E. Asymmetry gap in the electronic band structure of bilayer graphene. *Phys. Rev. B* **74**, 161403 (2006).

[71] Castro, E. V. *et al.* Biased bilayer graphene: Semiconductor with a gap tunable by the electric field effect. *Phys. Rev. Lett.* **99**, 216802 (2007).

[72] Min, H., Sahu, B., Banerjee, S. K. & MacDonald, A. H. Ab initio theory of gate induced gaps in graphene bilayers. *Phys. Rev. B* **75**, 155115 (2007).

[73] Zhou, S. Y. *et al.* Substrate-induced bandgap opening in epitaxial graphene. *Nature Mater.* **6**, 770–775 (2007).

[74] Zhou, S. Y., Siegel, D. A., Fedorov, A. V. & Lanzara, A. Metal to insulator transition in epitaxial graphene induced by molecular doping. *Phys. Rev. Lett.* **101**, 086402 (2008).

[75] Xia, F., Farmer, D. B., Lin, Y.-M. & Avouris, P. Graphene Field-Effect transistors with high On/Off current ratio and large transport band gap at room temperature. *Nano Lett.* **10**, 715–718 (2010).

[76] Zhang, Y. *et al.* Direct observation of a widely tunable bandgap in bilayer graphene. *Nature* **459**, 820–823 (2009).

[77] Mak, K. F., Lui, C. H., Shan, J. & Heinz, T. F. Observation of an electric-field-induced band gap in bilayer graphene by infrared spectroscopy. *Phys. Rev. Lett.* **102**, 256405 (2009).

[78] Kim, S. *et al.* Realization of a high mobility dual-gated graphene field-effect transistor with al2o3 dielectric. *Appl. Phys. Lett.* **94**, 062107 (2009).

[79] Tan, Y.-W. *et al.* Measurement of scattering rate and minimum conductivity in graphene. *Phys. Rev. Lett.* **99**, 246803 (2007).

[80] Xiao, S., Chen, J.-H., Adam, S., Williams, E. D. & Fuhrer, M. S. Charged impurity scattering in bilayer graphene. *Phys. Rev. B* **82**, 041406 (2010).

[81] Ni, Z. H. *et al.* On resonant scatterers as a factor limiting carrier mobility in graphene. *Nano. Lett.* **10**, 3868–3872 (2010).

[82] Deshpande, A., Bao, W., Zhao, Z., Lau, C. N. & LeRoy, B. J. Mapping the Dirac point in gated bilayer graphene. *Appl. Phys. Lett.* **95**, 243502 (2009).

[83] Stauber, T., Peres, N. M. R. & Guinea, F. Electronic transport in graphene: A semiclassical approach including midgap states. *Phys. Rev. B* **76**, 205423 (2007).

[84] Nilsson, J. & Castro Neto, A. H. Impurities in a biased graphene bilayer. *Phys. Rev. Lett.* **98**, 126801 (2007).

[85] Mkhitaryan, V. V. & Raikh, M. E. Disorder-induced tail states in gapped bilayer graphene. *Phys. Rev. B* **78**, 195409 (2008).

[86] Wehling, T. O., Yuan, S., Lichtenstein, A. I., Geim, A. K. & Katsnelson, M. I. Resonant scattering by realistic impurities in graphene. *Phys. Rev. Lett.* **105**, 056802 (2010).

[87] Craciun, M. F. *et al.* Trilayer graphene is a semimetal with a gate-tunable band overlap. *Nature Nanotech.* **4**, 383–388 (2009).

[88] Shklovskii, B. I. & Efros, A. L. *Electronic Properties of Doped Semiconductors* (Springer-Verlag, 1984).

[89] Henriksen, E. A. & Eisenstein, J. P. Measurement of the electronic compressibility of bilayer graphene. *Phys. Rev. B* **82**, 041412 (2010).

[90] Young, A. F. *et al.* Electronic compressibility of layer-polarized bilayer graphene. *Phys. Rev. B* **85**, 235458 (2012).

[91] Nishimura, H. Impurity conduction in the intermediate concentration region. *Phys. Rev.* **138**, A815–A821 (1965).

[92] Fritzsche, H. Effect of uniaxial compression on impurity conduction in n-type germanium. *Phys. Rev.* **125**, 1552–1560 (1962).

[93] Davis, E. A. & Compton, W. D. Compensation dependence of impurity conduction in antimony-doped germanium. *Phys. Rev.* **140**, A2183–A2194 (1965).

[94] Adam, S., Cho, S., Fuhrer, M. S. & Das Sarma, S. Density inhomogeneity driven percolation metal-insulator transition and dimensional crossover in graphene nanoribbons. *Phys. Rev. Lett.* **101**, 046404 (2008).

[95] Novoselov, K. S. *et al.* Unconventional quantum Hall effect and Berry's phase of 2π in bilayer graphene. *Nature Phys.* **2**, 177–180 (2006).

[96] Lu, C. L., Chang, C. P., Huang, Y. C., Chen, R. B. & Lin, M. L. Influence of an electric field on the optical properties of few-layer graphene with AB stacking. *Phys. Rev. B* **73**, 144427 (2006).

[97] Guinea, F., Neto, A. H. C. & Peres, N. M. R. Electronic states and Landau levels in graphene stacks. *Phys. Rev. B* **73**, 245426 (2006).

[98] Latil, S. & Henrard, L. Charge carriers in few-layer graphene films. *Phys. Rev. Lett.* **97**, 036803 (2006).

[99] Partoens, B. & Peeters, F. M. From graphene to graphite: Electronic structure around the K point. *Phys. Rev. B* **74**, 075404 (2006).

[100] Zhu, W., Perebeinos, V., Freitag, M. & Avouris, P. Carrier scattering, mobilities, and electrostatic potential in monolayer, bilayer, and trilayer graphene. *Phys. Rev. B* **80**, 235402 (2009).

[101] Li, G. & Andrei, E. Y. Observation of Landau levels of Dirac fermions in graphite. *Nature Phys.* **3**, 623–627 (2007).

[102] Miller, D. L. *et al.* Observing the quantization of zero mass carriers in graphene. *Science* **324**, 924–927 (2009).

[103] Taniguchi, T. & Watanabe, K. Synthesis of high-purity boron nitride single crystals under high pressure by using Ba-Bn solvent. *J. Cryst. Growth* **303**, 525–529 (2007).

[104] Bao, W. *et al.* Magnetoconductance oscillations and evidence for fractional quantum Hall states in suspended bilayer and trilayer graphene. *Phys. Rev. Lett.* **105**, 246601 (2010).

[105] Moser, J., Barreiro, A. & Bachtold, A. Current-induced cleaning of graphene. *Appl. Phys. Lett.* **91**, 163513 (2007).

[106] Bolotin, K. I., Sikes, K. J., Hone, J., Stormer, H. L. & Kim, P. Temperature-dependent transport in suspended graphene. *Phys. Rev. Lett.* **101**, 096802 (2008).

[107] Piazza, V. *et al.* First-order phase transitions in a quantum Hall ferromagnet. *Nature* **402**, 638–641 (1999).

[108] Zhang, X. C., Faulhaber, D. R. & Jiang, H. W. Multiple phases with the same quantized Hall conductance in a two-subband system. *Phys. Rev. Lett.* **95**, 216801 (2005).

[109] Koshino, M. & McCann, E. Landau level spectra and the quantum Hall effect of multilayer graphene. *Phys. Rev. B* **83**, 165443 (2011).

[110] Zhang, Y. *et al.* Landau-level splitting in graphene in high magnetic fields. *Phys. Rev. Lett.* **96**, 136806 (2006).

[111] Checkelsky, J. G., Li, L. & Ong, N. P. Zero-energy state in graphene in a high magnetic field. *Phys. Rev. Lett.* **100**, 206801 (2008).

[112] Zhao, Y., Cadden-Zimansky, P., Jiang, Z. & Kim, P. Symmetry breaking in the zero-energy Landau level in bilayer graphene. *Phys. Rev. Lett.* **104**, 066801 (2009).

[113] Song, Y. J. *et al.* High-resolution tunnelling spectroscopy of a graphene quartet. *Nature* **467**, 185–189 (2010).

[114] Jungwirth, T., Shukla, S. P., Smrčka, L., Shayegan, M. & MacDonald, A. H. Magnetic anisotropy in quantum Hall ferromagnets. *Phys. Rev. Lett.* **81**, 2328–2331 (1998).

[115] Ezawa, M. Supersymmetry and unconventional quantum Hall effect in monolayer, bilayer and trilayer graphene. *Physica E* **40**, 269–272 (2007).

[116] Koshino, M. & McCann, E. Gate-induced interlayer asymmetry in ABA-stacked trilayer graphene. *Phys. Rev. B* **79**, 125443 (2009).

[117] Niimi, Y., Kambara, H. & Fukuyama, H. Localized distributions of quasi-two-dimensional electronic states near defects artificially created at graphite surfaces in magnetic fields. *Phys. Rev. Lett.* **102**, 026803 (2009).

[118] Yan, J., Henriksen, E. A., Kim, P. & Pinczuk, A. Observation of anomalous phonon softening in bilayer graphene. *Phys. Rev. Lett.* **101**, 136804 (2008).

[119] Li, Z. Q. *et al.* Band structure asymmetry of bilayer graphene revealed by infrared spectroscopy. *Phys. Rev. Lett.* **102**, 037403 (2009).

[120] Kuzmenko, A. B., Crassee, I., van der Marel, D., Blake, P. & Novoselov, K. S. Determination of the gate-tunable band gap and tight-binding parameters in bilayer graphene using infrared spectroscopy. *Phys. Rev. B* **80**, 165406 (2009).

[121] Dillon, R. O., Spain, I. L. & McClure, J. W. Electronic energy band parameters of graphite and their dependence on pressure, temperature and acceptor concentration. *J. Phys. Chem. Solids* **38**, 635 – 645 (1977).

[122] Tatar, R. C. & Rabii, S. Electronic properties of graphite: A unified theoretical study. *Phys. Rev. B* **25**, 4126–4141 (1982).

[123] Charlier, J.-C., Gonze, X. & Michenaud, J.-P. First-principles study of the electronic properties of graphite. *Phys. Rev. B* **43**, 4579–4589 (1991).

[124] Abanin, D. A. *et al.* Dissipative quantum Hall effect in graphene near the Dirac point. *Phys. Rev. Lett.* **98**, 196806 (2007).

[125] Bloch, F. Über die Quantenmechanik der Elektronen in Kristallgittern. *Z. Phys.* **52**, 555–600 (1929).

[126] Tsoi, V. S. Focusing of electrons in a metal by a transverse magnetic field. *JETP Lett.* **19**, 70–71 (1974).

[127] Tsoi, V. S., Bass, J. & Wyder, P. Studying conduction-electron/interface interactions using transverse electron focusing. *Rev. Mod. Phys.* **71**, 1641–1693 (1999).

[128] van Houten, H. *et al.* Coherent electron focusing with quantum point contacts in a two-dimensional electron gas. *Phys. Rev. B* **39**, 8556–8575 (1989).

[129] Rokhinson, L. P., Larkina, V., Lyanda-Geller, Y. B., Pfeiffer, L. N. & West, K. W. Spin separation in cyclotron motion. *Phys. Rev. Lett.* **93**, 146601 (2004).

[130] Goldman, V. J., Su, B. & Jain, J. K. Detection of composite fermions by magnetic focusing. *Phys. Rev. Lett.* **72**, 2065–2068 (1994).

[131] Smet, J. H. *et al.* Magnetic focusing of composite fermions through arrays of cavities. *Phys. Rev. Lett.* **77**, 2272–2275 (1996).

[132] Beenakker, C. W. J., van Houten, H. & van Wees, B. J. Mode interference effect in coherent electron focusing. *Europhys. Lett.* **4**, 359–364 (1988).

[133] Aidala, K. E. *et al.* Imaging magnetic focusing of coherent electron waves. *Nature Phys.* **3**, 464–468 (2007).

[134] Rakyta, P., Kormányos, A., Cserti, J. & Koskinen, P. Exploring the graphene edges with coherent electron focusing. *Phys. Rev. B* **81**, 115411 (2010).

[135] Silvestrov, P. G. & Efetov, K. B. Charge accumulation at the boundaries of a graphene strip induced by a gate voltage: Electrostatic approach. *Phys. Rev. B* **77**, 155436 (2008).

[136] Cheianov, V. V., Falḱo, V. & Altshuler, B. L. The focusing of electron flow and a veselago lens in graphene p-n junctions. *Science* **315**, 1252–1255 (2007).

[137] Hwang, E. H. & Das Sarma, S. Acoustic phonon scattering limited carrier mobility in two-dimensional extrinsic graphene. *Phys. Rev. B* **77**, 115449 (2008).

[138] Heremans, J., Fuller, B. K., Thrush, C. M. & Partin, D. L. Temperature dependence of electron focusing in $In_{1-x}Ga_xAs$/InP heterojunctions. *Phys. Rev. B* **52**, 5767–5772 (1995).

[139] Schiefele, J., Sols, F. & Guinea, F. Temperature dependence of the conductivity of graphene on boron nitride. *Phys. Rev. B* **85**, 195420 (2012).

[140] Liu, Z. *et al.* Direct growth of graphene/hexagonal boron nitride stacked layers. *Nano Lett.* **11**, 2032–2037 (2011).

[141] Kotov, V. N., Uchoa, B., Pereira, V. M., Guinea, F. & Castro Neto, A. H. Electron-electron interactions in graphene: Current status and perspectives. *Rev. Mod. Phys.* **84**, 1067–1125 (2012).

[142] Gu, N., Rudner, M., Young, A., Kim, P. & Levitov, L. Collapse of Landau levels in gated graphene structures. *Phys. Rev. Lett.* **106**, 066601 (2011).

[143] Sanchez-Yamagishi, J. D. *et al.* Quantum Hall effect, screening, and layer-polarized insulating states in twisted bilayer graphene. *Phys. Rev. Lett.* **108**, 076601 (2012).

[144] Masubuchi, S. *et al.* Boundary scattering in ballistic graphene. *Phys. Rev. Lett.* **109**, 036601 (2012).

[145] van Wees, B. J. *et al.* Quantum ballistic and adiabatic electron transport studied with quantum point contacts. *Phys. Rev. B* **43**, 12431–12453 (1991).